1990

High resolution electron energy loss studies of O2, H, N, NO, and N2O adsorption on germanium surfaces

Anthony G. Entringer
Iowa State University

Order Number 9101349

High-resolution electron energy loss studies of O_2, H, N, NO, and N_2O adsorption on germanium surfaces

Entringer, Anthony G., Ph.D.

Iowa State University, 1990

U·M·I
300 N. Zeeb Rd.
Ann Arbor, MI 48106

High resolution electron energy loss studies of O_2, H, N, NO, and N_2O adsorption on germanium surfaces

by

Anthony G. Entringer

A Dissertation Submitted to the

Graduate Faculty in Partial Fulfillment of the

Requirements for the Degree of

DOCTOR OF PHILOSOPHY

Department: Physics
Major: Solid State Physics

Approved:

Signature was redacted for privacy.

Signature was redacted for privacy.

In Charge of Major Work

Signature was redacted for privacy.

For the Major Department

Signature was redacted for privacy.

For the Graduate College

Iowa State University
Ames, Iowa

1990

TABLE OF CONTENTS

DEDICATION

This dissertation is dedicated to my family.

ABSTRACT

The first high resolution electron energy loss spectroscopy (HREELS) studies of the oxidation and nitridation of germanium surfaces are reported. Both single crystal Ge(111) and disordered surfaces were studied. Surfaces were exposed to H, O_2, NO, N_2O, and N, after cleaning in ultra-high vacuum. The Ge surfaces were found to be non-reactive to molecular hydrogen (H_2) at room temperature. Exposure to atomic hydrogen (H) resulted hydrogen adsorption as demonstrated by the presence of Ge-H vibrational modes. The HREEL spectrum of the native oxide of Ge characteristic of ν-GeO_2 was obtained by heating the oxide to 200°C. Three peaks were observed at 33, 62, and 106 meV for molecular oxygen (O_2) adsorbed on clean Ge(111) at room temperature. These peaks are indicative of dissociative bonding and a dominant Ge-O-Ge bridge structure. Subsequent hydrogen exposure resulted in a shift of the Ge-H stretch from its isolated value of 247 meV to 267 meV, indicative of a dominant +3 oxidation state. A high density of dangling bonds and defects and deeper oxygen penetration at the amorphous Ge surface result in a dilute bridge structure with a predominant +1 oxidation state for similar exposures. Molecules of N_2O decompose at the surfaces to desorbed N_2 molecules and chemisorbed oxygen atoms. In contrast, both oxygen and nitrogen are detected at the surfaces following exposure to NO molecules. Both NO and N_2O appear to dissociate and bond at the top surface layer. Molecular nitrogen (N_2) does not react with the Ge surfaces, however, a precursor Ge nitride is observed at room temperature

following exposure to nitrogen atoms and ions. Removal of oxygen by heating of the NO-exposed surface to 550°C enabled the identification of the Ge-N vibrational modes. These modes show a structure similar to that of germanium nitride. This spectrum is also identical to that of the N-exposed surface heated to 550°C. Surface phonon modes of the narrow-gap semiconducting compounds Mg_2Sn, Mg_2Ge and Mg_2Si were detected at 29, 32, and 40 meV, respectively. The native oxide of all three show a dominant Mg-O mode at 80 meV. Probable Sn-O, Ge-O, and Si-O modes are also identified. Complete removal of the oxide layer was accomplished only on the Mg_2Si surface but resulted in no noticeable change in the energy of the surface phonon. Results are compared to the known bulk optical properties of these compounds.

I. INTRODUCTION

A. General Description of HREELS

High resolution electron energy loss spectroscopy (HREELS) is a technique that uses the scattering of low energy electrons from a surface to determine the vibrational properties of the surface. Figure 1.1 shows a monochromatic beam of electrons with an energy distribution centered around an energy E_p and some spread in energy δE incident upon a surface. The scattered beam has, in addition to the elastic peak centered at E_p, an additional peak at an energy ΔE below that of the elastic peak. Some of the electrons have lost an energy $\Delta E = \hbar\omega$ to the surface vibration of frequency ω. The exact nature of the scattering cross section will be discussed in a later chapter. In a typical HREELS experiment the energy distribution of the scattered beam is then collected and compared with IR absorption data, Raman scattering data, neutron scattering data, other HREELS spectra, or anything else that will help in the interpretation of the peaks. A full discussion of the technique is given in the book by Ibach and Mills.[1]

The incident electron energy E_p for this technique ranges from 1 eV to about 20 eV, and the spread in energy δE ranges from 5 meV to about 20 meV. The low incident energies are needed to insure surface sensitivity and also to insure that other higher energy processes do not compete with the vibrational scattering cross section. These higher order processes include valence band and core level electronic

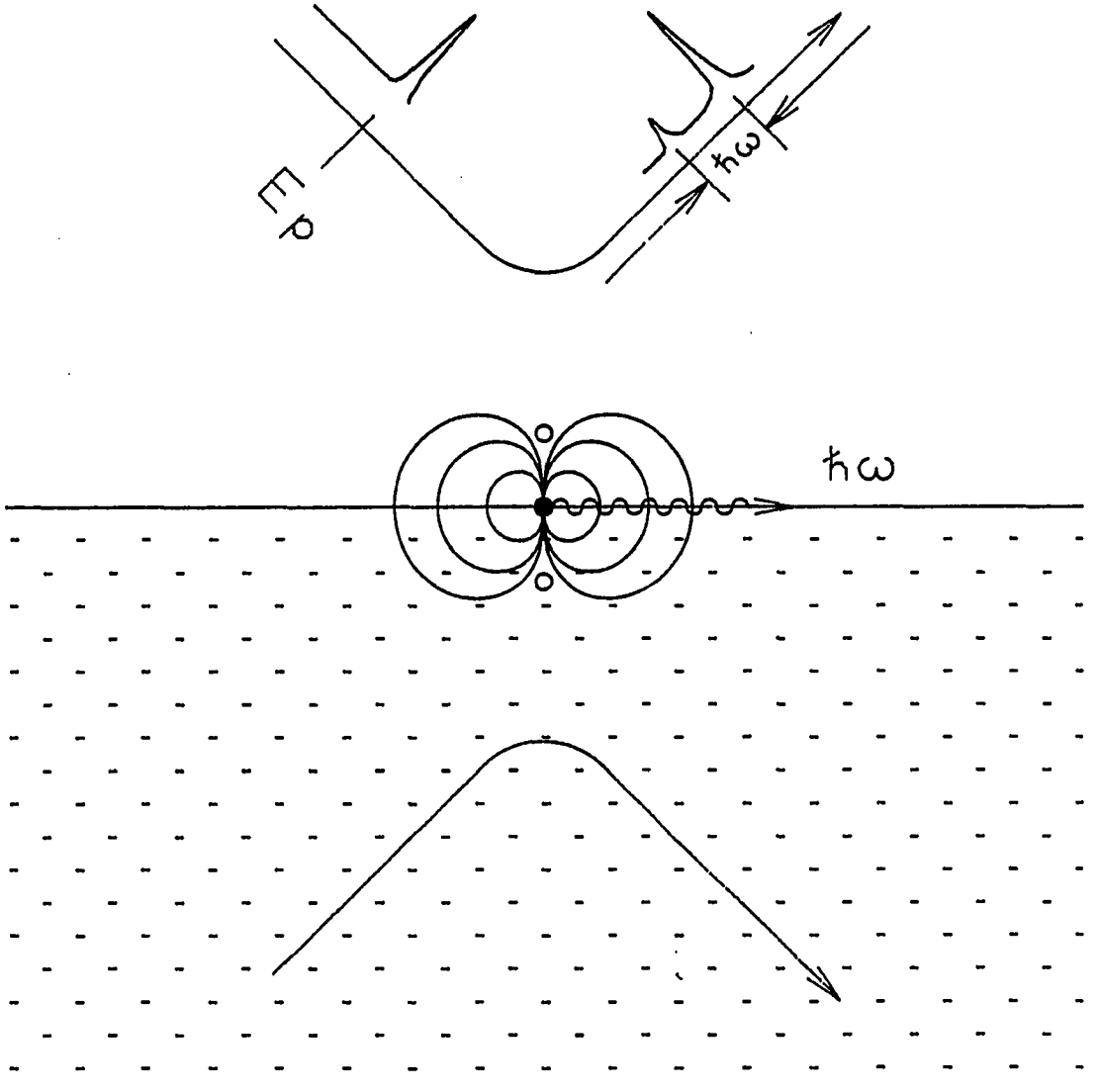

Fig. 1.1 Diagram of the scattering process. The dipole field set up by the electron and its image interacts with a surface mode, causing the electron to lose energy $\hbar\omega$

transitions, Auger processes, plasmons, and secondary electron emmission.

Fig. 1.2[2] shows the relationship of the spectrum obtained in HREELS to those obtained by other spectroscopies consisting of both incident and outgoing electrons. The peak at E_0 is the elastic peak. The large peak at low energies consists of the "true" secondary electrons often used to image in electron microscopy. The inset shows Auger transitions in the first derivative mode. It must be pointed out that in contrast to the EELS peaks, the position of the Auger peaks are independent of the elastic peak. The plasmons and the valence band and core level transitions occur in the E_0-50 to E_0 range while the vibrational transitions are bunched up close to the elastic peak. The energies of these vibrational transitions differ from the elastic peak by only meV and so are not resolvable on this figure.

B. Experimental Difficulties

The low energy of the incident electrons causes special experimental difficulties. These low energy electrons are extremely sensitive to uneven work functions on the surfaces of the instrument. Work function variations of even 1/2 volt are too much. To alleviate this problem, most HREEL spectrometers are coated on the inside with graphite. The elements are also provided with bakeout heaters. Once baked, this provides a uniform phase of graphitic carbon with little work function variation. Gold plating is sometimes used on conducting

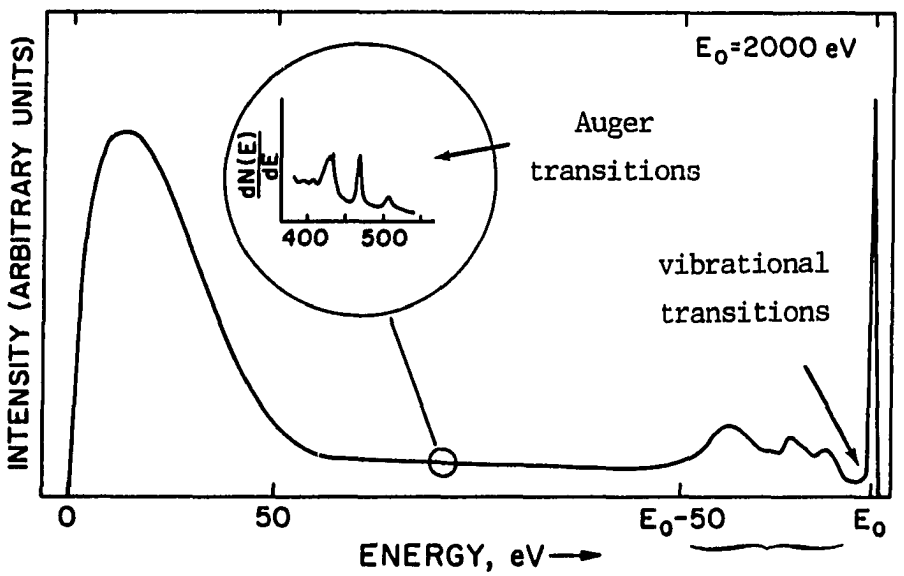

Fig. 1.2 Spectrum of electrons scattered from a solid (ref. 2). E_0 is the energy of the elastic peak. The large peak near zero energy is due to "true" secondary electrons

surfaces.

The low energy electrons are also very susceptible to magnetic fields, which tend to deflect the electron beam out of the desired position. Magnetic shielding must be provided to ensure that the field does not exceed about 50 mGauss. Particularly troublesome sources of magnetic field include the earth's magnetic field (0.6 Gauss), alternating magnetic fields, and ion pumps whose fields can reach several thousand Gauss. Care must be taken so that the magnetic field does not "leak" through cracks and holes in the shielding.

Tuning the spectrometer itself presents difficulty. One is working in an n-dimensional space where n is on the order of the number of spectrometer voltages. The ELS-22 spectrometer contains 4 sector voltages, 2 slit voltages, 2 contact voltages, 1 repeller voltage, 3 electron gun anode voltages with 3 associated asymmetries, and 4 voltages associated with accleration and deceleration optics with 3 associated asymmetries. One can also adjust the beam energy and the filament current. Hence, there are many local maxima in the electron beam current which may not result in the best signal. Tuning of the spectrometer demands patience and practice.

Finally, the electron beam itself is rather large (1/2 cm long) and is not imageable as in, for example, Auger spectroscopy. One must make sure that the surface being studied is being hit by the beam. This calls for very precise geometric alignment of the sample. Cleaning of the sample by sputter-etching requires an ion gun with a very large raster size (1 cm^2 or greater) so that the entire electron beam will hit

the cleaned surface.

C. History of HREELS

The history of HREELS goes back about 20 years. In 1967 Prost and Piper first demonstrated the feasibility of using HREELS to detect vibrations of gas molecules adsorbed at a surface.[3] They detected vibrations of H_2, N_2, CO, and H_2O adsorbed on W(100). The first direct observation of a surface optical phonon was reported by Ibach in 1970 on ZnO(110).[4] These so-called Fuchs-Kliewer surface modes were first predicted by Fuchs and Kliewer in 1965.[5] Both adsorbate vibrations and Fuchs-Kliewer surface modes are dealt with in this work. A review paper by Thiry[6] shows the number of HREELS experimental papers published annually from 1967 to 1984. This review plus an earlier version[7] contain a total of 525 references to experimental works involving HREELS. Examination of these references indicates that the vast majority of works are metal-adsorbate studies. This may be partially due to the fact that metal surfaces are very important in the area of catalysis. Metals also have the advantage of being easier to work with than semiconductors, both from a theoretical and experimental standpoint. About 25% of the works involve semiconductors or insulators, and of this 25% the majority involve adsorbates on the surface of silicon. Again this is not surprising considering the technological importance of silicon in the semiconductor industry. A literature search of the remaining years 1985-1989 also indicates a

predominance of HREELS studies on metals and silicon. .

The semiconducting compounds Mg_2Si, Mg_2Ge, and Mg_2Sn also have not been studied before using the HREELS technique. We have obtained some results on these compounds. Because the main thrust of this dissertation involves studies on germanium, the results of these experiments are presented at the end.

D. Studies on Germanium

Part of the motivation of this work is the little attention that germanium has received in this respect. As of Jan. 1990, only three other papers involving HREELS studies on germanium have been published.[8-10] All involve Ge(100). One involves hydrogen adsorption and the other two involve water adsorption. The main results will be discussed in a later chapter.

The study of hydrogen adsorption on germanium and silicon is especially important in the area of amorphous semiconductors. In unhydrogenated amorphous semiconductors, dangling bonds cause states to arise within the gap, thus degrading the electrical properties of the material. Hydrogen is used to terminate these dangling bonds and elimate the unwanted states within the gap. Also, amorphous semiconductors contain structures called microvoids. These are actual internal surfaces that occur within the bulk of the material. These microvoids seem to be an important factor in controlling hydrogen diffusion.[11] The bonding of hydrogen at these microvoids (especially

large microvoids) can be understood in terms of bonding at surfaces, where, in both cases, weakening of depolarization effects tend to affect vibrational ferquencies. IR studies of hydrogenated amorphous semiconductors can be compared to HREEL studies of hydrogen adsorption to determine vibrational frequencies in microvoids.

Another motivating factor for this work is that germanium, while it will probably never achieve the technological importance of silicon, is increasingly becoming a material of interest. Germanium has certain advantages over silicon including greater room temperature electron and hole mobilities. This brings it into consideration along with GaAs for high-speed digital and microwave devices. Also the electron and hole mobilities are more nearly equivalent than in GaAs, making it a better candidate for complementary structures. Strained-layer Ge_xSi_{1-x}/Si heterostructures and superlattices have been shown to be promising candidates for photodetectors and heterojunction bipolar transistors.[12] The observation of resonant tunneling in these structures also shows them to be good candidates for quantum nanostructure devices.[13] Finally, films of GeO_x have been generating increasing interest as optical memory devices.[14]

The success of silicon in the semiconductor industry is to a great extent derived from the ability to grow a stable insulating oxide layer on the surface. This technology for germanium is still in its infancy. An excellent review article by Gregory and Crisman[15] summarizes with 149 references current understanding of both oxidation and nitridation processes on germanium and the ability of these processes to form a

passivating insulator on the germanium surface. Important to the understanding of these processes is the understanding of how the initial stages of oxidation and nitridation proceed as well as the effects of the form of the oxidant and nitridant, whether it be O_2, NO, N_2O, NH_3, or N atoms. These questions are the main ones that will be addressed in this thesis.

II. THEORY OF HREELS

A. General Remarks

There are three basic scattering mechanisms in HREELS:[1] 1) dipole scattering, where electrons interact with the spatially extended dipole field of an adsorbate or surface phonon, 2) impact scattering, where the electrons interact directly with the atomic potentials of the surface atoms, and 3) resonance scattering, where electrons are temporarily trapped in empty orbitals of adsorbate atoms and then scatter. The latter two are often grouped together as nondipolar scattering. Because the experimantal part of this work deals only with dipole scattering experiments, only the dipole scattering mechanism will be fully developed.

One of the more important concepts in the development of the scattering cross section is that of a loss function.[16] Consider an isotropic solid described by a frequency and wave vector dependent dielectric function $\varepsilon(\omega,q)=\varepsilon_1+i\varepsilon_2$. Energy can be dissipated into the dielectric in several ways: 1) by the attenuation of electromagnetic radiation of the proper energy, 2) by bulk induced losses of electrons travelling through the solid, and 3) by surface induced losses of electrons travelling close to the surface. The attenuation of electromagnetic radiation is described by the imaginary part (ε_2) of the dielectric function. Frequency regions where $\varepsilon_2(\omega)$ is large are regions of resonant absorbtion. We are more concerned, however, with the latter

two modes of dissipation.

The energy dissipation rate per unit volume due to dielectric losses is given by the time rate of change of the energy density:

$$P = \frac{1}{4\pi}\mathbf{E}\cdot\left(\frac{\partial \mathbf{D}}{\partial t}\right). \tag{2.1}$$

If we consider the Fourier components $\mathbf{E}(\omega,\mathbf{q})$ and $\mathbf{D}(\omega,\mathbf{q})$ of the field within the dielectric, we can write the time-average power as

$$\bar{P} = \frac{1}{4\pi}\cdot\langle \mathrm{Re}\{\mathbf{E}(\omega,\mathbf{q})e^{-i\omega t}\}\cdot \mathrm{Re}\{-i\omega\mathbf{D}(\omega,\mathbf{q})e^{-i\omega t}\}\rangle. \tag{2.2}$$

For an electron travelling through an isotropic medium, the actual field $\mathbf{E}(\omega,\mathbf{q})$ within the crystal is essentially that due to the free charge $\mathbf{D}(\omega,\mathbf{q})$ screened by polarization charges described by the dielectric function $\varepsilon(\omega,\mathbf{q})$:

$$\mathbf{E}(\omega,\mathbf{q}) = \frac{\mathbf{D}(\omega,\mathbf{q})}{\varepsilon(\omega,\mathbf{q})}. \tag{2.3}$$

The expression for the time average power then becomes

$$\bar{P}(\omega,\mathbf{q}) = \frac{1}{4\pi}\cdot\langle \mathrm{Re}\{\varepsilon^{-1}(\omega,\mathbf{q})\mathbf{D}(\omega,\mathbf{q})e^{-i\omega t}\}\cdot \mathrm{Re}\{-i\omega\mathbf{D}(\omega,\mathbf{q})e^{-i\omega t}\}\rangle \tag{2.4}$$

$$= \frac{1}{4\pi}\cdot\omega D^2(\omega,\mathbf{q})\langle(\mathrm{Re}\{1/\varepsilon\}\cos\omega t+\mathrm{Im}\{1/\varepsilon\}\sin\omega t)\cdot(-\sin\omega t)\rangle \tag{2.5}$$

$$= \frac{\omega}{8\pi}\cdot D^2(\omega,\mathbf{q})\,\mathrm{Im}\left(\frac{-1}{\varepsilon(\omega,\mathbf{q})}\right). \tag{2.6}$$

Therefore the probability of exciting a quantum of energy $\hbar\omega$ by a charge moving in the bulk is proportional to $\mathrm{Im}\{-1/\varepsilon\}$.

For a charge moving in front of a semiinfinite dielectric, the method of images can be used to find the effect of screening.[17] One finds that the field is screened by a factor of $1/\varepsilon+\varepsilon'$ where ε and ε' are the dielectric constants for the two media. For a charge moving in vacuum in front of a dielectric, the probability for energy loss will be proportional to

$$\text{Surface Loss Function} \propto \mathrm{Im}\left(\frac{-1}{\varepsilon(\omega,q) + 1}\right). \tag{2.7}$$

Maxima in the surface loss function will correspond to maxima in the loss spectrum. For negligible damping this will have a maximum for $\varepsilon(\omega_s)=-1$. Letting ε_o and ε_∞ be the low frequency and high frequency dielectric constants, respectively, and taking the standard expression for the dielectric function of an ionic insulator

$$\varepsilon(\omega) = \varepsilon_\infty + \frac{\varepsilon_o - \varepsilon_\infty}{1 - \omega^2/\omega^2_{TO}}, \tag{2.8}$$

setting it equal to -1 and solving for ω_s, we get the surface mode energy

$$\omega_s = \omega_{TO}\left(\frac{\varepsilon_o + 1}{\varepsilon_\infty + 1}\right). \tag{2.9}$$

Following Ibach and Mills,[1] we now examine the nature of the dipole

scattering cross section. For an adsorbate with a dipole moment p and natural frequency ω_0 the dipole potential above the surface can be written as

$$V(r,t) = 2pz/r^3 \cdot \exp(-i\omega_0 t) \qquad (2.10)$$

where the z-axis is chosen to be the surface normal and the factor of 2 comes from the contribution of the image potential. This may be resolved into Fourier components consisting of two-dimensional waves that lie on a plane parallel to the surface. These waves have a wave vector given by $q_{||}$. The condition that the potential obey LaPlace's equation then requires that the z-dependence be $\exp(-q_{||}z)$. The potential in terms of these Fourier components is then given by

$$V(r,t) = (p/\pi)\exp(-i\omega_0 t) \cdot \int d^2q_{||} \exp(iq_{||} \cdot r_{||}) \exp(-q_{||}z). \qquad (2.11)$$

Here $r_{||}$ is the projection of r onto the surface plane. Notice that the contribution from each Fourier component has a spatial extent into the vacuum above the crystal on the order of $q_{||}^{-1}$. An incident electron approaching the surface with energy E_i and wave vector k_i will be in a plane wave state $|E_i,k_i\rangle$. The scattered electron will be in a plane wave state $|E_s,k_s\rangle$. In first order perturbation theory (Born approximation) the scattering cross section is proportional to the squared matrix element $|\langle E_s,k_s|V(r,t)|E_i,k_i\rangle|^2$. The only nonvanishing Fourier component from V(r,t) is that one with $q_{||}=k_{s||}-k_{i||}$. This is equivalent to conservation of momentum parallel to the surface. For

small angle deflections and high incident energies then $q_{\parallel} \simeq k_i \theta_s$ where θ_s is the angle between k_s and the specular direction. Maximum coupling of the incident electron occurs when its velocity v_o resembles the group velocity of the surface exitation, $v_o \simeq \omega_o / q_{\parallel}$.[18] Combining these two expressions gives the scattering angle $\theta_s \simeq \omega_o / k_i v_o$ or $\theta_s \simeq \hbar\omega_o / 2E_i$. Thus, under usual experimental conditions where $\hbar\omega_o << E_i$, the scattering is sharply peaked about the specular direction.

This then allows for an estimate of the wave vector transfer in dipole scattering. This will be given approximately by $q_{\parallel} \simeq k_i (\hbar\omega_o / 2E_i)$. For an incident energy of 10 eV and loss energies in the range of 100 meV $q_{\parallel}$, is estimated to be on the order of 10^{-2} $Å^{-1}$, which is very close to the Γ point of the surface Brillouin zone. The extent of the dipole field into the vacuum is then accordingly about 100 Å.

An important selection rule for dipole scattering is the dipole selection rule.[1] Dipoles that are aligned perpendicular to the surface will be enhanced by the image charge and will contribute to the scattering cross section. Dipoles that are parallel to the surface will be screened by the image charge and not contribute to the scattering cross section. Screening will be complete in the case of a perfect metal but will depend on the strength of the dielectric constant for the case of semi-insulating compounds such as semiconductors.

For collective excitation of solids such as plasmons and phonons the selection rule is that only surface modes will contribute to the scattering cross section. This comes about due to the fact that surface scattering is sharply peaked in the specular direction, while bulk

scattering gives a more isotropic cross section. Because of the small input aperture of high resolution electron energy loss spectrometers (typical input aperture of 2°), the amount of bulk scattering related to surface scattering is estimated to be on the order of 10^{-2}.

B. Scattering Probabilities

The scattering probability for inelastic scattering in the dipole regime from surface phonons is given below:

$$Q = \frac{I_{inelas}}{I_{elas}} = \frac{\pi e^2}{2\hbar v \cos\theta} \cdot \frac{\exp(\hbar\omega_s/kT)}{\exp(\hbar\omega_s/kT)-1} \cdot \left(\frac{\varepsilon_o - 1}{\varepsilon_o + 1} - \frac{\varepsilon_\infty - 1}{\varepsilon_\infty + 1} \right) \quad (2.12)$$

This was derived by Ibach and Mills[1] and is also derived using a slightly different approach in Appendix A. Here ω_s is the surface mode frequency given by (2.9), v is the velocity of the incident electron, and θ is the angle of incidence. This expression consists of three terms. The first term is material independent and was first obtained by Stern and Ferrel.[19] The second term takes into account finite temperature effects, and the third term corrects for the screening effect of the material. Note that this expression depends on bulk parameters of the material. This is due to the fact that these Fuchs-Kliewer surface phonons extend several hundred Angstroms into the material where the bulk properties dominate.

A slightly different expression for the scattering probability in the dipole regime is obtained when one is exciting vibrational modes of

adsorbate species. This expression is given below:

$$Q = \frac{I_{inelas}}{I_{elas}} = \frac{4\pi e^2}{\hbar v^2 \cos\theta} \cdot F_s \cdot \frac{(e^*)^2 n_s}{M_r \omega_s \varepsilon_\infty^2}. \qquad (2.13)$$

This expression has been derived by several authors[1,20] using the model of a thin dielectric surface layer on top of the bulk material. Here F_s is a function of the acceptance angle θ_c and the incident angle θ_I; e^* is an effective ionic charge; M_r is the reduced mass of the oscillator; ε_∞ is the high frequency dielectric constant of the surface layer, and n_s is the number of scatterers per unit area. A table of the function F_s for different acceptance and incident angles is given by Ibach and Mills.[1] Note that this expression depends mainly on surface parameters of the material, in contrast to the expression for the surface phonon scattering probability. Also note that this scattering probability falls off as E_I^{-1} whereas the probability for surface phonon scattering falls off as $E_I^{-1/2}$. This expression can be used to calculate the effective ionic charge e^* from HREELS data. Often this effective ionic charge is expressed in terms of the perpendicular component of the dipole moment matrix element. The dipole moment matrix element is simply e^* times the x matrix element and is given by

$$\hbar(e^*)^2/2M_r\omega_s = |\langle 1|\mu_\perp|0\rangle|^2 \qquad (2.14)$$

This then gives for the scattering probability:

$$Q = \frac{I_{inelas}}{I_{elas}} = \frac{8\pi e^2 n_s}{\varepsilon_\infty{}^2 \hbar^2 v^2 \cos\theta} \cdot F_s \cdot |\langle 1|\mu_\perp|0\rangle|^2. \qquad (2.15)$$

Note that the scattering probability is proportional to the coverage n_s.

Often the dipole-dipole interaction between adsorbed molecules causes a nonlinearity in the intensity as a function of coverage and an upward shift in the vibrational frequency. A measure of this coupling is the surface electronic polarizability α_e. Ibach has derived the scattering probability for the case of dipole-dipole coupling:[1]

$$Q = \frac{I_{inelas}}{I_{elas}} = \frac{\pi e^2}{\hbar v^2 \cos\theta} \cdot F_s \cdot \frac{(e^*)^2 n_s}{M_r \omega_s} \cdot \frac{1}{(1 + \alpha_e \Sigma)^2}. \qquad (2.16)$$

Here Σ is a sum over nearest neighbors:

$$\Sigma = \sum_{i \neq j} (1/r_{ij})^3 \qquad (2.17)$$

For an HCP structure, $\Sigma = 8.9(n_s)^{3/2}$. Fig. 2.1a shows the scattering probability as a function of coverage when dipole coupling is appreciable. Notice that the scattering probability passes through a maximum. Fig. 2.1b shows the scattering probability as a function of coverage when dipole coverage is negligible. Note the linear dependence. An example of where dipole coupling is important is in the case of CO adsorbed on Ru(100). The intensity of the CO stretch passes through a maximum for a coverage of $\theta = 0.4$. The frequency of the CO

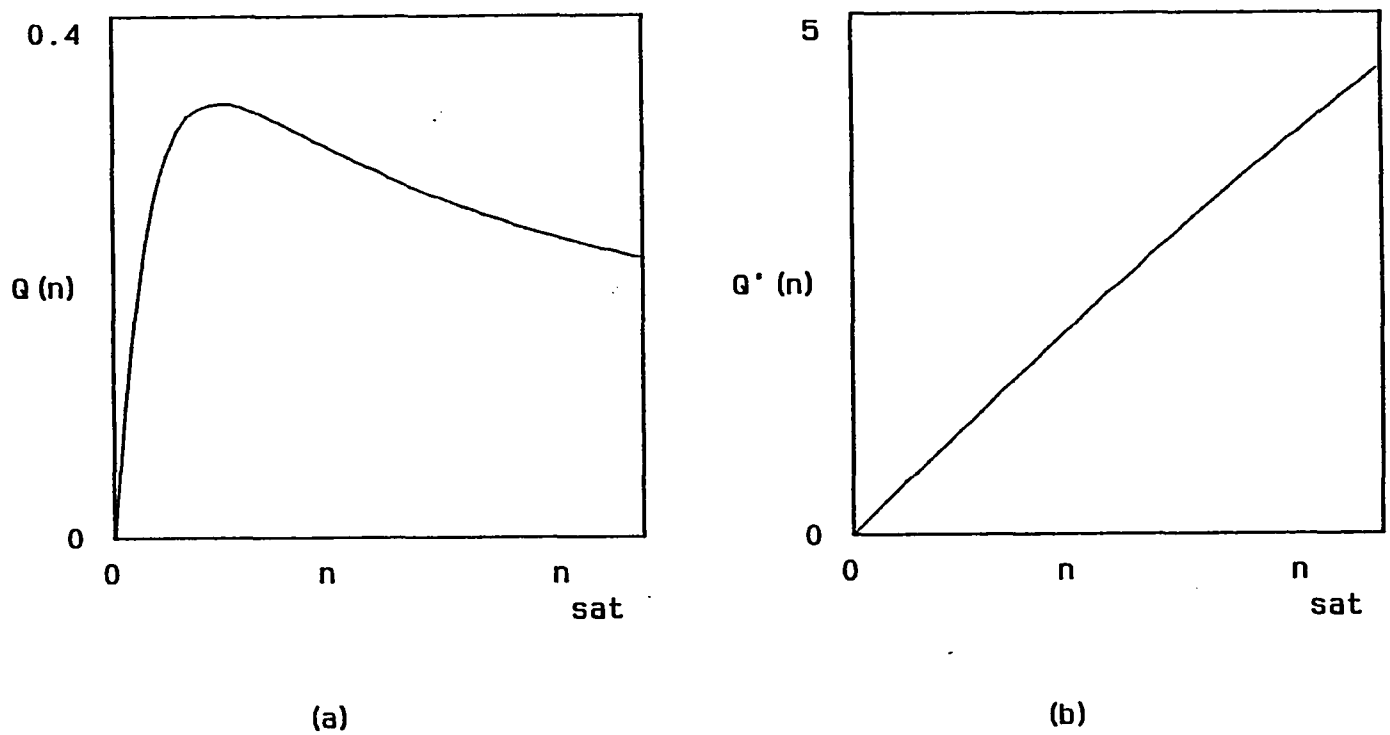

Fig. 2.1 Scattering probability (Q) vs. coverage (n): (a) where dipole-dipole coupling is appreciable; (b) where dipole-dipole coupling is negligible

stretch increases from about 246 meV at zero coverage to about 257 meV near saturation.

C. Overtones and Multiple Losses

There are two basic types of secondary peaks that occur in electron energy loss spectroscopy, overtones and multiple losses. These are illustrated in Fig. 2.2. Overtones are true second-order processes whereby the electron will couple to an oscillator by making transitions over two or more energy levels. They are usually observed on adsorbed layers. Multiple losses result from several consecutive first-order transitions and are often observed when the scattering probability is high, as is the case of scattering from surface phonons. Each of these processes is discussed below.

Because multiple losses are the result of several first-order transitions, they occur at exact multiples of the fundamental. As shown in the Appendix, they are described by a Poisson distribution:

$$P_n = e^{-Q} \cdot \frac{Q^n}{n!}. \qquad (2.18)$$

Here Q is the ratio of the intensity of the first loss peak to that of the elastic peak.

Selection rules forbid an ideal harmonic oscillator to make transitions other than $\Delta n=1$. The existence of overtones is due to anharmonicity in the oscillator potential. Deviations from harmonicity

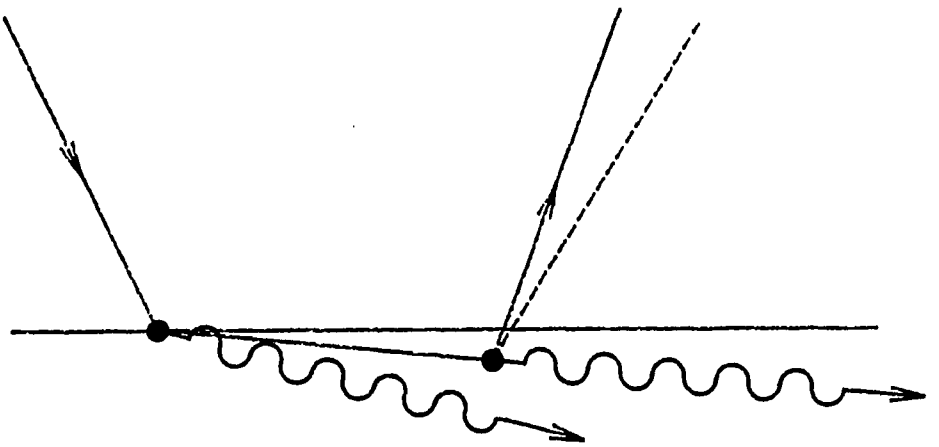

(a)

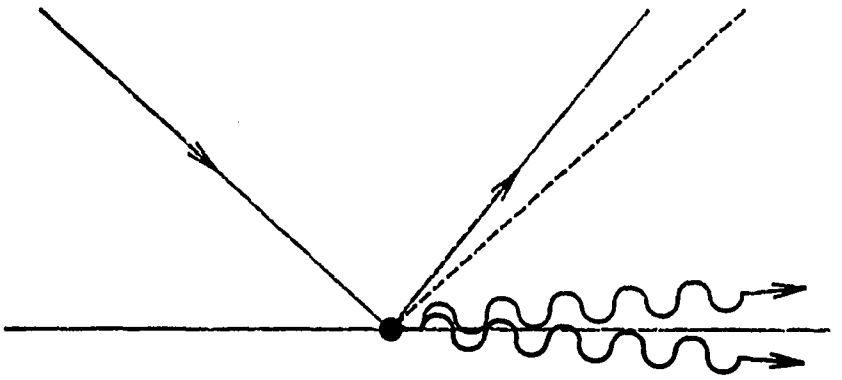

(b)

Fig. 2.2 Illustration of the two types of secondary losses: (a) multiple loss scattering; (b) overtone scattering

are often dealt with by assuming that the potential energy is more accurately described by a Morse potential:

$$V(r) = D_o[1 - \exp(-a(r - r_o)]^2 \qquad (2.19)$$

Here D_o, the dissociation energy, is the depth of the potential well and a is a measure of the width of the well. The energy eigenvalues of this potential can be solved for exactly and are given by

$$\omega_n = \omega_e(n + \tfrac{1}{2}) - \omega_e x_e(n + \tfrac{1}{2})^2 \qquad (2.20)$$

where

$$\omega_e = a(D_o\hbar/c\pi\mu)^{\frac{1}{2}} \quad \text{and} \quad \omega_e x_e = \hbar a^2/4\pi c\mu. \qquad (2.21)$$

In an ideal harmonic oscillator potential, the energy eigenvalues are equally spaced. For the Morse potential, the energy eigenvalues get closer and closer together as one goes up in energy. In fact the rate of change of energy with respect to n vanishes at the dissociation limit:

$$d\omega_n/dn \Big|_{n_{max}} = 0 = \omega_e - 2\omega_e x_e(n_{max} + \tfrac{1}{2}), \qquad (2.22)$$

so that

$$n_{max} + \tfrac{1}{2} = \omega_e/2\omega_e x_e. \qquad (2.23)$$

The dissociation energy is simply the difference between the ground state $\omega(0)$ and $\omega(n_{max})$:

$$D_o = \hbar[(\omega_e{}^2/4\omega_e x_e) - \tfrac{1}{2}\omega_e + \tfrac{1}{4}\omega_e x_e]. \qquad (2.24)$$

When expressed in terms of the fundamental $\nu_1=\omega(1)-\omega(0)$ and the first

overtone $\nu_2=\omega(2)-\omega(0)$, the dissociation energy becomes

$$D_0 = \hbar\left(\frac{(3\nu_1 - \nu_2)^2}{(4\nu_1 - 2\nu_2)} - \frac{5}{4}\nu_1 + \frac{3}{8}\nu_2\right). \tag{2.25}$$

It is useful to consider the dipole moment matrix elements of the Morse potential. These have been calculated and tabulated.[21] For $x_e<<1$ the matrix element between the ground state and first excited state has the form of that of the simple harmonic oscillator:

$$\langle 1|p|0\rangle \simeq e^*(\hbar/2M_r\omega_e)^{1/2} \tag{2.26}$$

For a harmonic oscillator, the dipole matrix element between the ground state and second excited state vanishes. This is no longer the case when anharmonicity is involved. For $x_e<<1$ we have:

$$\langle 2|p|0\rangle \simeq e^*(x_e/2)^{1/2}(\hbar/2M_r\omega_e)^{1/2} \tag{2.27}$$

Since the scattering probability is proportional to the square of the matrix element, the first overtone loss will be reduced by a factor $x_e/2$ from that of the primary loss. The anharmonicity parameter x_e is typically of the order of 10^{-2}, and so the overtone loss peak is reduced accordingly. These results will be applied to the HREEL specta of hydrogen adsorbed on Ge.

III. INSTRUMENTATION AND EXPERIMENTAL PROCEDURE

This chapter will expand on the theory of the 127° sector and its use in high resolution EELS. Later it will describe the cylindrical mirror analyzer (CMA) used in Auger spectroscopy and electronic EELS. Finally, it will describe the sample preparation procedure used in the experiments. The details of tuning the HREEL spectrometer are given in Appendix B.

A. The 127° Sector

Figure 3.1 shows the basic setup of a high resolution electron energy loss spectrometer. It consists of a hairpin filament that acts as a source of electrons. These electrons are then fed into the monochromator which lets only those electrons with an energy E_0 pass. The resolution of the beam is determined by the formula[1]

$$\Delta E = [As + B\alpha^n + C\beta^n]\cdot E_0. \qquad (3.1)$$

Here s is the slit width, and α and β are, respectively, the angular apertures in the plane and perpendicular to the plane of deflection. For a 127° deflector, A=2/r (r is the radius of the deflector), B=4/3, C=1, and n=2. The experimenter reduces the pass energy to improve the resolution, but at the same time must keep sufficient signal in order to do the experiment. The electrons leaving the monochromator have an

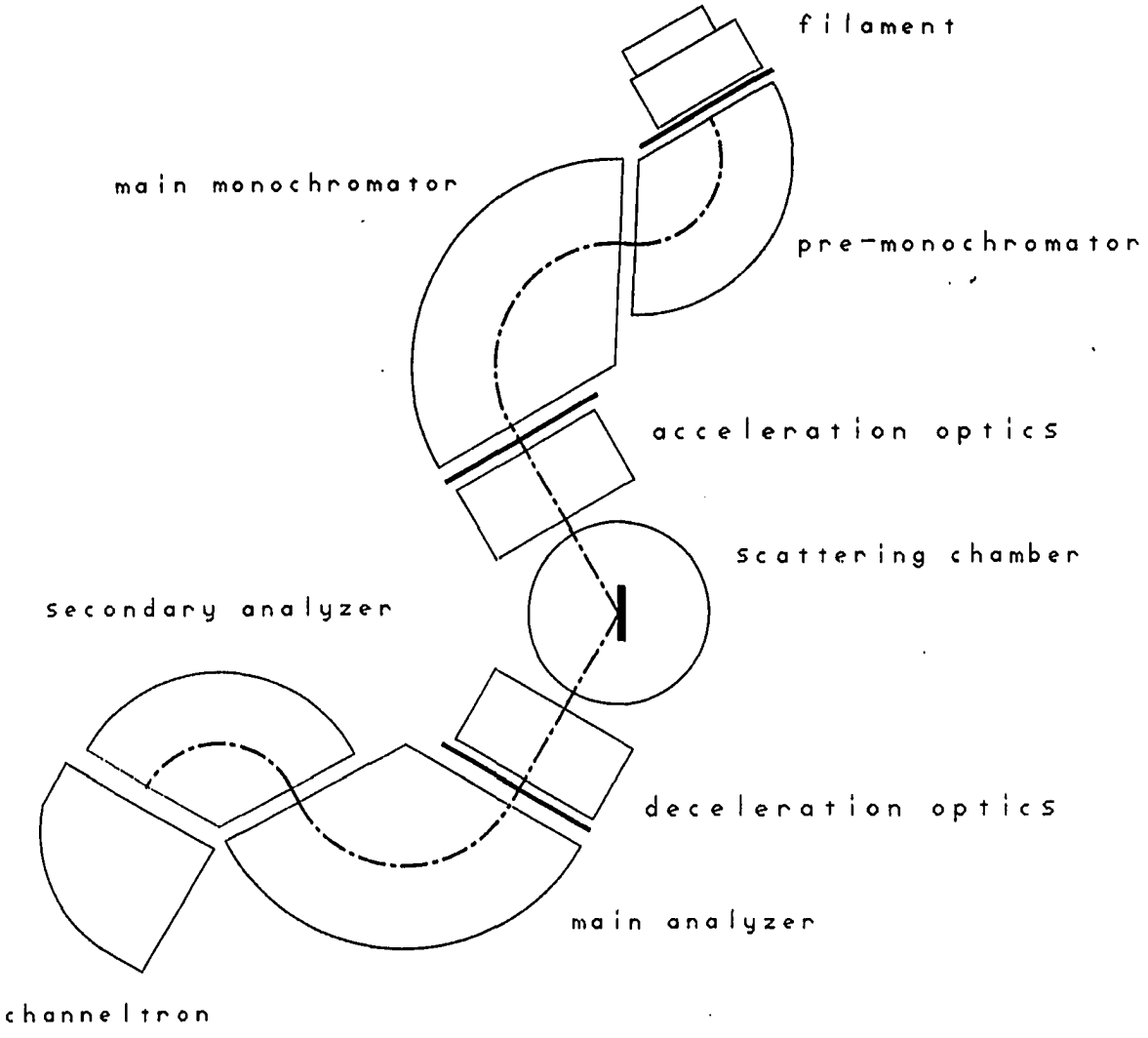

Fig. 3.1 High resolution electron energy loss spectrometer

energy E_0. They are then accelerated towards the sample to an energy E_p. This energy is usually in the 2-20 eV range. The electrons are then decelerated and focused into the analyzer. The analyzer scans the desired energy range as the channeltron measures the output, thus producing the spectrum. On a clean single crystal surface count rates of 10^5 cps are possible with an energy spread ΔE=10 meV.

The pre-monochromator, main monochromater, main analyzer, and secondary analyzer all are intended to pass electrons of a single energy. Each consists of two concentric cylindrical plates across which a potential V has been applied (see Fig. 3.2). They are bounded on each end by a narrow slit. Here R is the radius of the outer cylinder and r is the radius of the inner cylinder. The electric field between the plates is inversely proportional to the radius,

$$E(\rho) = E_0 \frac{\rho_0}{\rho} , \tag{3.2}$$

where E_0 is the electric field at the radius ρ_0 at which the slits are located, usually halfway between the plates. This is simply related to the potential V:

$$E_0 = \frac{V}{\ln(R/r)} \cdot \ln \frac{1}{\rho_0} . \tag{3.3}$$

Any electron moving in circular motion around the cylinder at radius ρ_0 will have a velocity v_0 given by

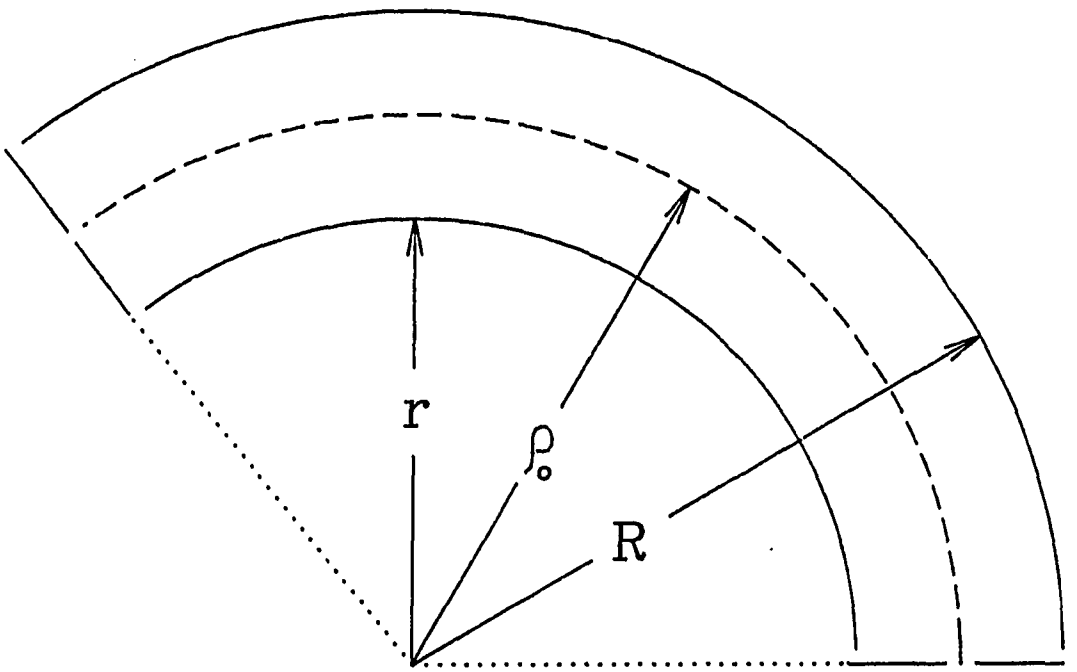

Fig. 3.2 The cylindrical 127° sector: r = inner radius; R = outer radius; ρ_0 = radius of main path

$$m\frac{v_o^2}{\rho_o} = eE_o \ . \tag{3.4}$$

These are the electrons we wish to pass. Electrons with too much or too little energy will not pass through the slit. The controllable parameter here is E_o. By changing the potential across the plates (and hence the value of E_o) we can select the energy of the electrons that pass through the sector.

However, not all the electrons that have velocity v_o will be moving in circular motion. There will be a small but finite angular distribution of electrons having velocity v_o that enter the sector. We wish to capture those electrons as well. There exists an optimal angle for doing this. The value of this angle will now be derived.

The general equation of motion for an electron in the sector is given by

$$m\frac{d^2\rho}{dt^2} = m\frac{v^2}{\rho} - eE \ . \tag{3.5}$$

For circular motion this reduces to (2.1). For small deviations from circular orbit we can approximate the electric field near ρ_o as

$$E(\rho) \approx E_o\left[1 - \frac{\Delta\rho}{\rho_o}\right] , \tag{3.6}$$

where $\Delta\rho$ is given by

$$\rho = \rho_o + \Delta\rho \ . \tag{3.7}$$

The equation of motion for the electron's deviation from the main path then becomes

$$\frac{d^2(\Delta\rho)}{dt^2} = \frac{v^2}{\rho} - \frac{e}{m}\cdot E_o\left[1 - \frac{\Delta\rho}{\rho_o}\right] \ . \tag{3.8}$$

Before substituting for r we will express the velocity v in terms of r. Utilizing conservation of angular momentum under the action of a central force, we get

$$mvr = \text{const.} = mv_o r_o \ . \tag{3.9}$$

Equation (2.7) then becomes

$$\frac{d^2(\Delta\rho)}{dt^2} = v_o^2\cdot\frac{\rho_o^2}{\rho^3} - \frac{e}{m}\cdot E_o\left[1 - \frac{\Delta\rho}{\rho_o}\right] \ . \tag{3.10}$$

We can now substitute (2.6) into the cubic term in the denominator of (2.9). This term can be expanded using:

$$(\rho_o + \Delta\rho)^{-3} = \frac{1}{\rho_o^3}\cdot\left[1 + \frac{\Delta\rho}{\rho_o}\right] \approx \frac{1}{\rho_o^3}\cdot\left[1 - 3\cdot\frac{\Delta\rho}{\rho_o}\right] \ , \tag{3.11}$$

to give

$$\frac{d^2(\Delta\rho)}{dt^2} = \frac{v_o^2}{\rho_o} - 3\cdot\frac{v_o^2}{\rho_o^2}\cdot\Delta\rho - \frac{e}{m}\cdot E_o + \frac{e}{m}\cdot\frac{E_o}{\rho_o}\cdot\Delta\rho \ . \tag{3.12}$$

The first and third terms on the right hand side cancel using (2.3).

Also using (2.3) we can combine the second and fourth terms to give

$$\frac{d^2(\Delta\rho)}{dt^2} = -2\cdot\frac{v_o^2}{\rho_o^2}\cdot(\Delta\rho) \tag{3.13}$$

or

$$\frac{d^2(\Delta\rho)}{dt^2} + 2\dot{\theta}^2\cdot(\Delta\rho) = 0 \ , \tag{3.14}$$

where θ is the angular velocity of the electrons on their circular trajectory. Notice that $\Delta\rho$ exhibits simple harmonic motion with an angular frequency given by

$$\omega_{\Delta\rho} = 2^{1/2}\cdot\dot{\theta} \ , \tag{3.15}$$

and the period of oscillation given by

$$T_{\Delta\rho} = \frac{2\pi}{\omega_{\Delta\rho}} = \frac{2\pi}{2^{1/2}\cdot\dot{\theta}} \ . \tag{3.16}$$

Electrons entering the sector at the slit at $t = 0$ will have $\Delta\rho \approx 0$. They will diverge slightly to a maximum at $t = T_{\Delta\rho}/4$, and then they will reconverge back to $\Delta\rho \approx 0$ at $t = T_{\Delta\rho}/2$. During this time they will have traveled through an angle θ given by

$$\theta = \dot{\theta}\cdot\frac{T_{\Delta\rho}}{2} = \frac{\pi}{2^{1/2}} = 127^\circ \ . \tag{3.17}$$

This is the optimal angle for so-called 1st order focusing.[22]

B. The Cylindrical Mirror Analyzer (CMA)

The analyzer used to perform the electronic EELS and Auger experiments is a cylindrical mirror analyzer (CMA). It basically consists of two concentric cylinders with entrance and exit slits located at either end (see Fig. 3.3). The inner cylinder is usually grounded, and the outer cylinder is given a negative potential V. An electron gun is located inside the inner cylinder between the slits. The sample is positioned in such a way that the angle subtended by the entrance slit from the main axis is 42.3°. This is the natural focal point for the analyzer and allows for simpler focusing. Auger electrons from the sample excited by the primary beam (or primary beam electrons that have lost energy) enter the entrance slit and are reflected back through the exit slit. They are then focused onto an exit aperture (also located at the natural focal point) after which they are collected by an electron multiplier. The pass energy (in eV) of the analyzer is given by $V=1.31V_{outer}\ln(R_{outer}/R_{inner})$. The outer plate is ramped across the desired energy range.

Because Auger transitions and electronic losses are superimposed on a large background of secondary electrons, electronic differentiation techniques are used to accentuate the peaks. This is done by adding a small modulated voltage ($k<<V$) to the outer cylinder of the analyzer:

$$\Delta V = k\sin\omega t \qquad (3.18)$$

This causes the current at the detector to also be modulated. Expanding

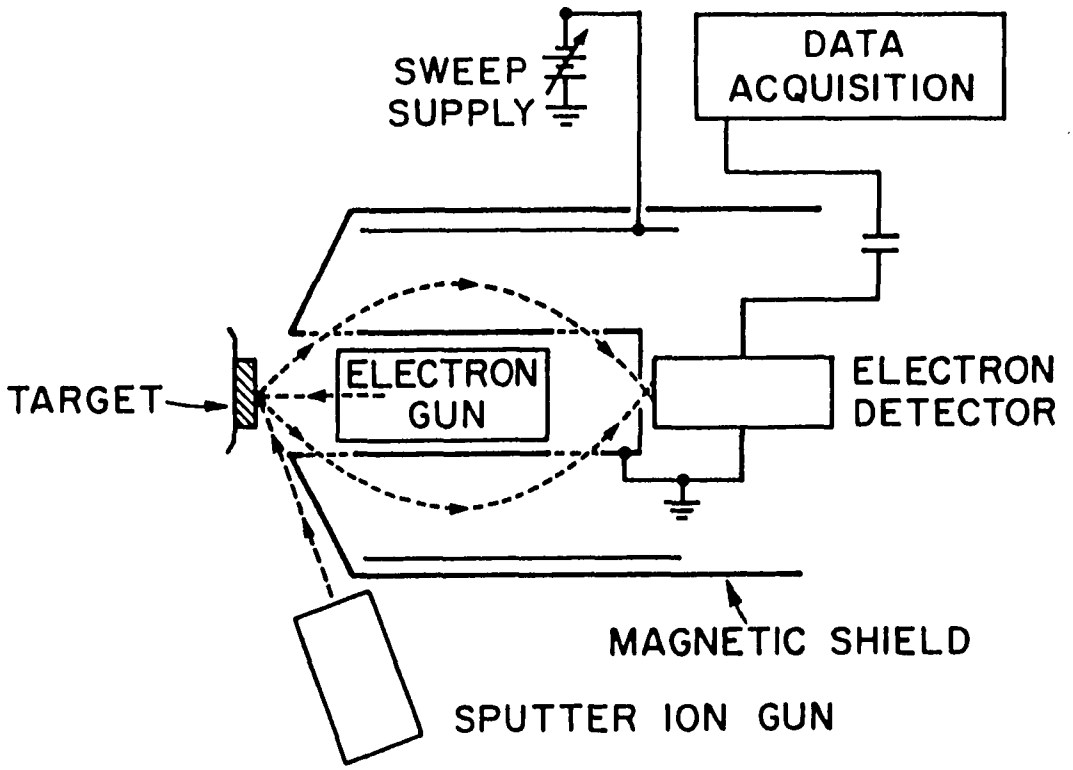

Fig. 3.3 Experimental apparatus used in Auger electron spectroscopy and electronic EELS (ref. 2)

this in a Taylor series and using some trig identities we get:

$$I(V + k\sin\omega t) = I_0 + (kI' + \ldots)\sin\omega t - (k^2 I'' + \ldots)\cos 2\omega t. \quad (3.19)$$

Here I_0 includes all of the time independent terms. Because k is small, we can neglect terms of order k^3 and higher. A lock-in amplifier is set to detect the component of the signal with frequency ω for the first derivative mode. This is what is generally done for Auger electron spectroscopy. For electronic EELS measurements the second derivative is measured by locking in to the 2ω frequency component.

C. Sample Preparation

Samples used in this study were Ge(111), a disordered, sputter-etched Ge(111), and a film of a-Ge. The Ge(111) surface was cleaned by cycles of 1-3 keV Ar^+ etching and subsequent annealing at ~550°C for 30 minutes. Annealing was sometimes performed also during the Ar^+ etching, with no observed effect on the experimental results. This cleaning procedure is believed to result in a c(2x8) reconstructed surface.[23,24] In our samples the density of surface dangling bonds and defects is unknown, but as the following experiments indicate, it appears to be lower, as expected, at the annealed surface. The native oxide can also be desorbed by heating to 550°C for 30 minutes. This procedure, however, always resulted in a high background and a poor resolution in the HREELS experiments. Samples were heated resistively or by electron bombardment from the rear. The disordered surface was prepared by Ar^+

sputter-etching the crystalline material without further annealing. An rf sputter-deposited hydrogenated amorphous germanium (a-Ge:H) film was also used.[25] As will be seen, the hydrogen in this film is preferentially etched by Ar^+ ions during surface cleaning. Results were qualitatively similar for both the sputter-etched and the amorphous film surfaces. Clean surfaces were exposed to various gases at 300K by backfilling the vacuum chambers through leak valves at pressures of 10^{-8} to 10^{-4} Torr. Hydrogen adsorption was obtained by dissociating hydrogen gas on a hot (~1700°C) tungsten filament. Adsorbed oxygen was removed from the surface by heating to ~550°C for several minutes as needed. Chemisorbed nitrogen remained at the surface under these conditions.

The HREELS experiments were performed using the previously described Leybold-Heraeus ELS-22 spectrometer. Prior to exposing the surfaces to gas molecules the cleanliness was verified by checking for the absence of Ge-O, C-H and O-H vibrational modes. The HREELS measurements were performed in the specular direction with an incident angle of 60°. The primary energy, E_p, was 5 eV and the elastic peak width ranged from ~9 to 20 meV, depending on surface cleanliness and order.

A PHI model 545 Auger spectrometer was used for surface analysis, and core level and valence band EELS studies. Sample cleanliness and coverage were regularly monitored. The relative concentrations were calculated using the equation $C_x = (I_x/S_x)/\Sigma_n(I_n/S_n)$, where C_x is the concentration of element x, I_x is its peak to peak height, and S_x is the relative sensitivity factor. The relative sensitivity factors used for

the Auger analysis were 0.1 for Ge(LMM), 0.5 for O(KLL), and 0.35 for N(KLL).[26] Although an oversimplification, this approach is sometimes used to analyze adsorbed layers.[27,28] The error in the estimated concentration increases with coverage. The N(KLL) intensities under the same experimental conditions, as well as the N(KLL)/Ge(LMM) values, at the Ge(111) surface exposed to activated N_2O saturate at an exposure of ~6000 L. These values are unchanged when the surfaces are annealed to remove oxygen. From the above, N coverage relative to saturation can be estimated. A value so obtained is also given. It should be noted that all the above coverage calculations render the same qualitative results. In the present work the analysis is used only for a qualitative comparison. The E_p values for the EELS experiments varied from 100 to 200 eV. Spectra were taken in the $-d^2N(E)/dE^2$ mode and the resolution was typically 1-1.5 eV. The electron beam was 60° to the surface normal.

The ion gauge filaments did not affect the interaction of NO and N_2O with the Ge surfaces. Electrons originating from the Auger electron gun, however, did have a small effect on the adsorption process. Adsorption was therefore carried out with the electron beam turned off. The primary beam, with currents less than 1μA, did not appear to stimulate desorption during the measurement time as the EEL spectra were identical when taken before or after exposing the surfaces to 3kV electrons used for analysis. The ion pump in the Auger system appeared to strongly activate NO, N_2O, and N_2 gases. Activated species, which may include atoms, ions, and excited species, result in the bonding of

relatively large quantities of N and O. To avoid these activated species, the poppet valve separating the ion pump from the vacuum chamber was closed for the short period of adsorption, and the chamber was pumped by a turbo-molecular pump. This procedure resulted in high levels of surface contaminants (>2%) at high exposures (>10^3L). The smaller quantities of bonded N and O observed under these experimental conditions are not a result of bonded contaminants that prevent further N and O bonding. Molecular hydrogen does not interact with Ge surfaces. Also, no nitrogen was detected at the surfaces exposed to N_2 or N_2O while operating the turbo-molecular pump only. Nitrogen was detected, however, when these same surfaces, with no additional cleaning, were subsequently exposed to the above molecules while pumping with the ion pump. This problem did not exist in the HREELS system where the sample was located during adsorption far away (~2 m) from the line of sight of the ion pump. In the HREELS system exposure to atoms and ions of nitrogen was carried out by using N_2 in a differentially pumped ion gun at ~100 eV and a pressure of ~10^{-4} Torr.

IV. RESULTS AND DISCUSSION

A. Previous Studies

Frequently we will be comparing the results of this work with the results of others who have done similar studies. The purpose of this section is to summarize some of the important results that have been done that are relevent to this work. These works include studies involving vibrational EELS, electronic EELS, and photoemission experiments.

Because of the similarities between germanium and silicon, it is often useful to compare similar experiments involving the two semiconductors. The interaction of H, N, O_2, NO, and N_2O with Si surfaces has been extensively studied using, in addition to other surface techniques, high resolution electron energy loss spectroscopy.[29-32] The interest in these studies was motivated mainly by the technological importance of the nitridation and the early stages of oxidation of the Si surfaces. As mentioned before, these processes at Ge surfaces have received less attention. Other than our studies, the only published HREELS works on germanium involve the adsorption of hydrogen and water on Ge(100).[8-10] Other important studies include photoemission studies of the oxidation of germanium,[33,34] differential reflectometry studies of N_2O on germanium,[35] and electronic EELS studies of H and O_2 adsorption on germanium.[36] The results of the present work are summarized in two papers.[37] The main points of these studies on

germanium will now be discussed.

In Fig. 4.1a is the HREEL spectrum of Ge(100)2x1 exposed to 500L atomized hydrogen.[8] The peak at 70 meV is the Ge-H wagging mode, and the peak at 247 meV is the G-H stretching mode. The peak at 247 meV is important for this work because it is very sensitive to its chemical environment. Shifts in this peak can determine the number of near-neighbor oxygen atoms.[38] Figures 4.1b and 4.1c represent a transition to a dihydride phase on the surface with the peak near 105 meV representing the Ge-H_2 scissors mode.

Fig. 4.2 shows the HREEL spectrum of Ge(100) first exposed to 3L water vapor at 90K and then warmed to 300K.[9] The adsorption had to be done at liquid nitrogen temperature (LNT) because water was not observed to adsorb on Ge(100) at room temperature. Both molecular and dissociative adsorption was observed at LNT. At room temperature only the dissociated species are observed. The peak at 243 meV is again the Ge-H stretch. The 83 meV peak is attributed to the Ge-OH stretch and the 115 meV peak is attributed to the Ge-OH bending mode. On Si surfaces these two modes are unresolved and occur at around 100 meV. The 450 meV peak is attributed to the O-H stretch. The 83- and 115-meV peaks in the spectrum of Fig. 4.2 are at the same positions as a similar study of water adsorption (1L) done on films of $Ge_xSi_{1-x}(100)$.[10] Here the author attributed the 115-meV peak to a surface oxide mode. As will be seen, our results do not support this claim.

It was mentioned before that shifts in the Ge-H stretch mode can be used to determine the number of near neighbor oxygen atoms. For a

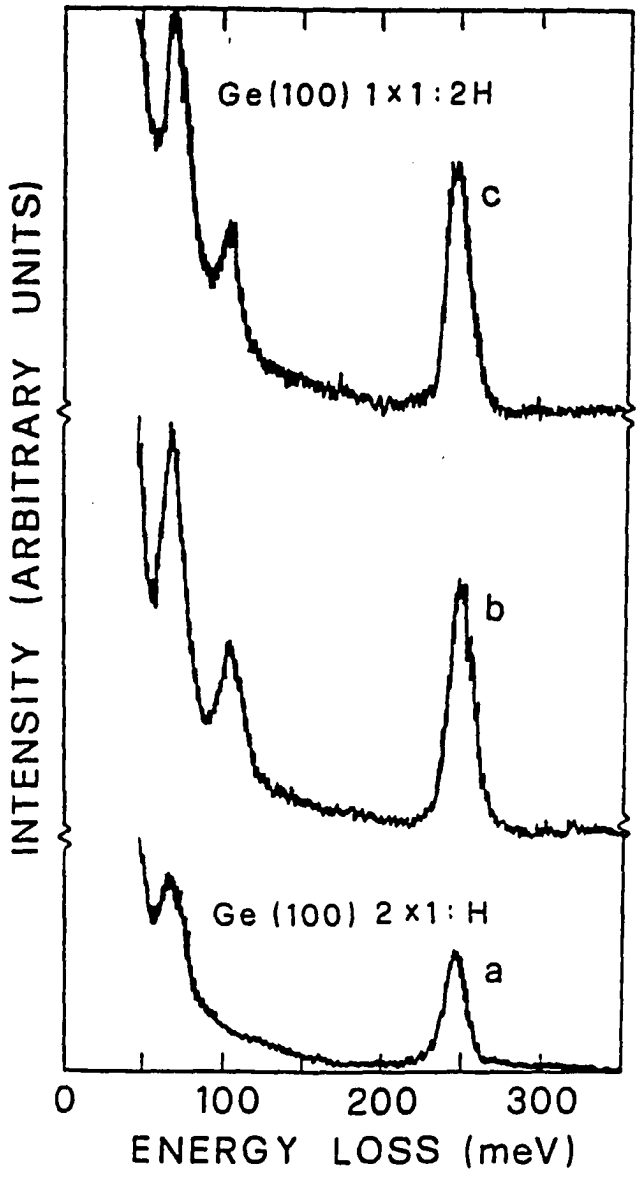

Fig. 4.1 HREELS of H/Ge(100): (a) monohydride phase; (b),(c) dihydride phase (ref. 8)

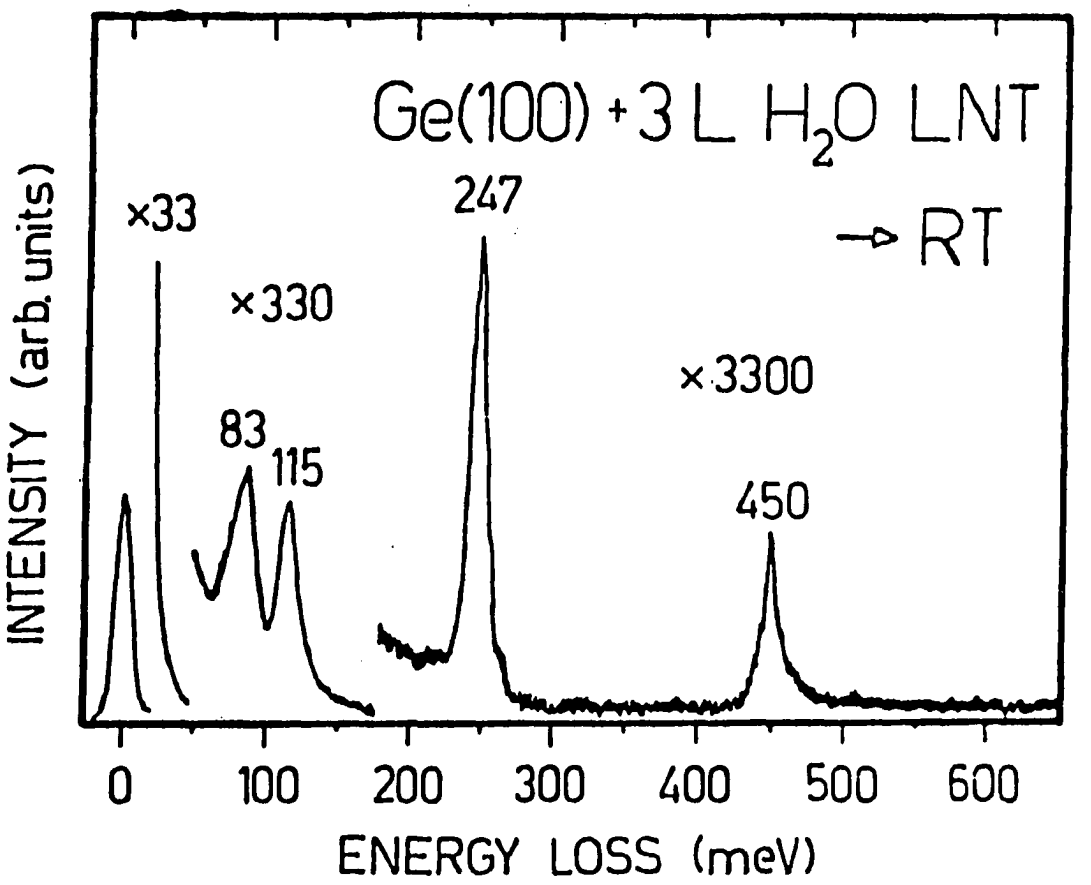

Fig. 4.2 HREELS of Ge(100) exposed to 3L H_2O at 70K, then warmed up to room temperature (ref. 9,10)

general substituted germane molecule, $GeHR_1R_2R_3$, the frequency of the Ge-H stretch mode depends on the electronegativities of the substituting R_j. As the electronegativities of the R_j increase, the electron cloud tends to pull away from the Ge atom and towards the R_j. This results in a more tightly bound Ge-H group and a higher vibrational energy. Oxygen has a higher electronegativity than germanium. Therefore, near neighbor oxygen atoms tend to raise the vibrational energy more than near neighbor Ge atoms. Empirically it is found[38] that the vibrational energy of the Ge-H bond obeys the relation

$$\hbar\omega_{Ge-H} = 222.7 + 2.84 \cdot \sum_j SR(R_j) \qquad (4.1)$$

Here $SR(R_j)$ are defined as the stability ratios, and the sum goes from 1 to 3. These stability ratios are directly related to the electronegativities of the near neighbor atoms:[38]

$$[X(R_j)] = 0.204 \cdot SR(R_j) + 0.806. \qquad (4.2)$$

Figure 4.3 shows the shifts for Ge and Si. The graphs show how the experimentally obtained vibrational energy increases as oxygen atoms are substituted for Ge or Si atoms. Because Ge and Si have the same electronegativity, they have the same stability ratio sums. These are shown at the top of the graph. Figure 4.4 shows possible bonding configurations that give rise to these shifts.

Our studies were used to elucidate the effect of surface order on the adsorption process, to compare chemisorption of oxygen originating from different oxygen containing molecules, and to study nitrogen

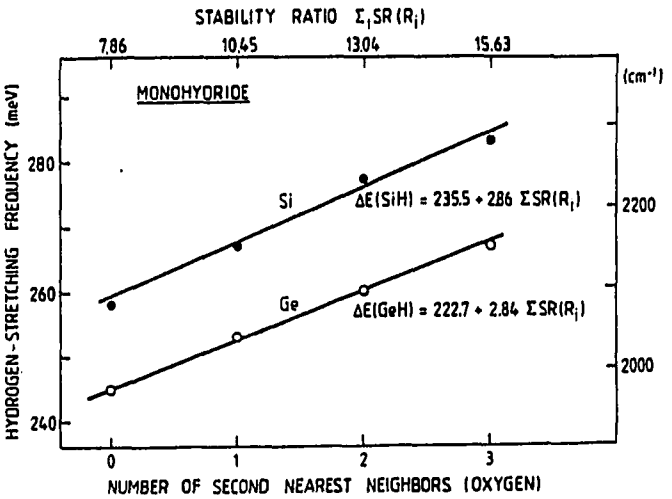

Fig. 4.3 Graph showing shift in Ge-H stretch as a function of number of near-neighbor oxygen atoms (ref. 32)

● Ge ○ oxygen			LOSS ENERGY (meV, cm^{-1})
Ge_{R_i}-H 245 (1976)	253 (2040)	260 (2097)	267 (2154)
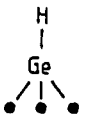	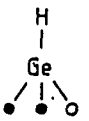	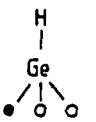	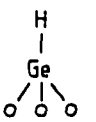
(a)	(b)	(c)	(d)

Fig. 4.4 Bonding configurations giving rise to shift in Ge-H stretch frequency (ref. 32)

bonding. Results are discussed and compared with reported photoemission studies.[33,34] Comparison with oxidation and nitridation of Si is also made.

B. Hydrogen on Ge

Figure 4.5 shows the HREEL spectrum of an a-Ge:H film that was cleaned by Ar^+ etching. The film was deposited by reactive rf sputtering from a polycrystalline target onto a single crystal Si substrate. The sputtering medium consisted of Ar (9-12 mTorr) and H_2 (1-9 mTorr). By IR techniques it was determined to have ~12 at. % Ge-H bonds. Detailed descriptions of the deposition process and the calculation of the concentration of hydrogen bonded to Ge may be found elsewhere.[25] The figure shows two features, one at 70 meV and the other at 247 meV. The highly sensitive HREELS technique shows that a small amount of hydrogen remains bonded to the surface following Ar^+ etching. Previous experiments[39,40] using valence-band and core-level EELS and Auger line shape measurements could not identify hydrogen induced features or Auger line shape changes at the Ar^+ etched surfaces. Auger line shape changes, however, were detected following hydrogen adsorption (see below). Bulk IR measurements on a-Ge:H deposited either by glow discharge decomposition of germane (GeH_4) or by rf sputtering show features at ~ 69, 95, 102, and 233, and 248 meV.[41] The 69 meV feature was assigned to the wagging mode of all Ge-H bonds. The peak at 233 meV was assigned to the bulk monohydride stretching mode, the 248 meV peak

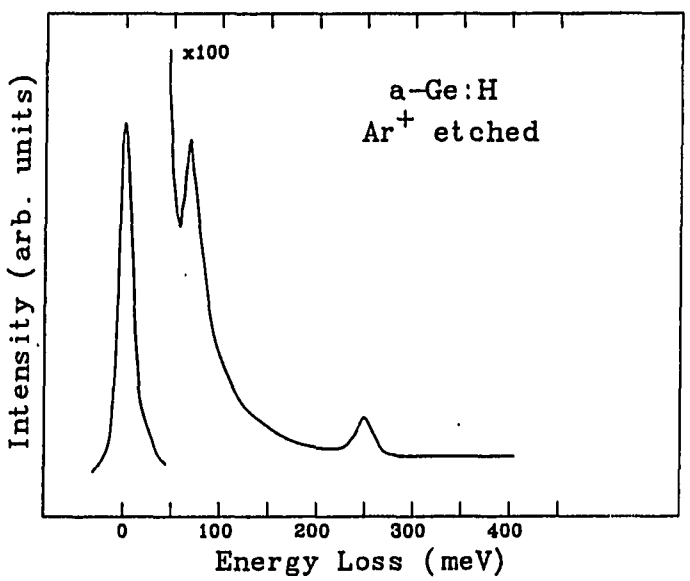

Fig. 4.5 HREELS of Ar^+ etched a-Ge:H

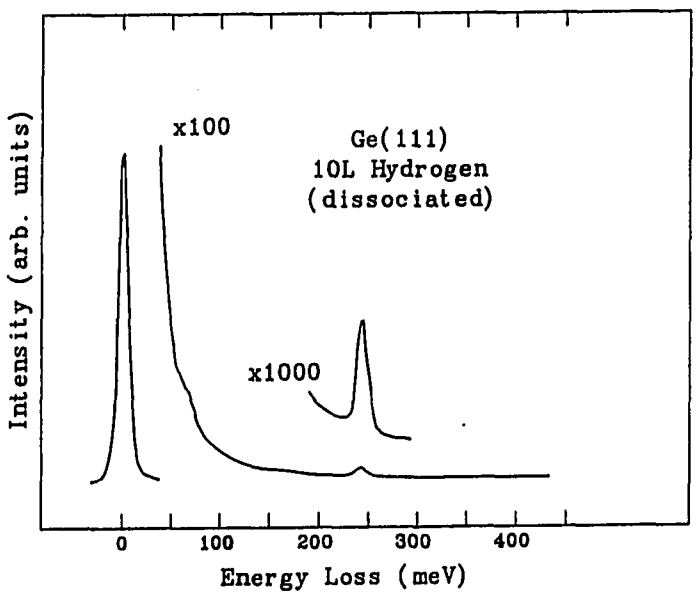

Fig. 4.6 HREELS of Ge(111) exposed to 10L H_2 (atomized)

was attributed to the dihydride (GeH_2) and trihydride ($Ge-H_3$) stretch modes. The 95 and 102 meV features were associated with the bending (scissors) modes of the di- and tri- hydride species. All these assignments parallel bulk IR results on a-Si:H.[42] The frequency of the monohydride stretch mode in bulk a-Si:H increases from 248 to 260 meV as the radius of the void around the H atom increases to 2Å.[43-45] In addition, the surface mono Si-H stretch mode, as measured by HREELS,[43] appeared at 260 meV, higher than the corresponding bulk frequency (248 meV) and similar to that of the bulk mono-H vibration in relatively large microvoids. A shift of vibration frequencies to higher values at surfaces relative to their corresponding bulk values is expected due to weakening of depolarization effects at the surfaces. Thus, we conclude that in accordance with results on single crystals of Si and Ge the 247 meV loss observed on the sputter-etched a-Ge:H surface stems mainly from the monohydride Ge-H stretch mode. The absence of the $Ge-H_2$ bending mode at 105 meV supports this conclusion.

Fig. 4.6 shows the spectrum of the Ge(111) surface exposed to 10L H_2 atomized on a hot (~1700°C) tungsten filament. Two modes are observed at ~70 meV and at ~245 meV. For exposures higher than 100L the width of the elastic peak increased to >20 meV, and the only resolvable peak was the peak at 245 meV. At this low coverage the peak at 245 meV is again assigned to the monohydride stretch, increased from its bulk value due to polarization effects at the surface. It is believed that the dihydride phase exists on Ge(111) at high exposures, but the scissors mode at ~105 meV characteristic of this phase could not be

resolved due to the degradation of the resolution. Also, no hydrogen could be detected at the Ge(111) surface following exposure at room temperature to molecular hydrogen.

Figure 4.7 shows the HREEL spectrum of the disordered surface exposed to 200L H_2 (atomized). This resulted in a large increase in the intensity of the Ge-H wag and stretch vibrations as compared to the sputter-etched a-Ge:H surface. The amorphous surface has a high density of dangling bonds, and consequently this results in a large scattering intensity when the surface is exposed to atomic hydrogen. The Ge-H stretch frequency again occurs at 247 meV. The small peak 105 meV is attributed to the dihydride scissors mode by comparison with the spectra for H/Ge(100) (see Fig. 4.1a). Note that this peak is very small compared to the intensity of the Ge-H wag at 70 meV. Empirically, it was shown by Shanks et al.[46] that the intensity of the Si-H wagging mode (78-80 meV) in IR spectroscopy is proportional to the hydrogen concentration in a-Si:H films. This is also true for the case of Ge and can be extended to the HREELS technique. For full coverage of dihydride units on the Ge(100) surface, the integrated intensities of the 70 meV and 105 meV peaks are roughly equal (Fig. 4.1). From this we conclude that on the disordered surface only a small fraction of the hydrogen atoms are attached in the dihydride phase. In addition to the multiple loss of the Ge-H wagging mode at 140 meV and the combination mode of 247+70, there is an overtone of the Ge-H stretching mode at 483 meV. This overtone can give information concerning the dissociation energy of the Ge-H bond. Note that this is slightly less than twice the

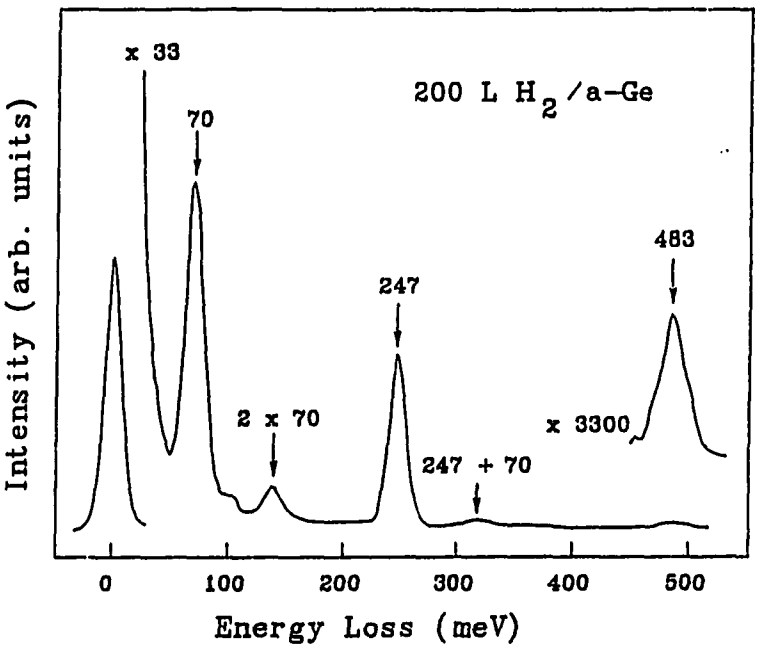

Fig. 4.7 HREELS of a-Ge exposed to 200L H_2 (atomized)

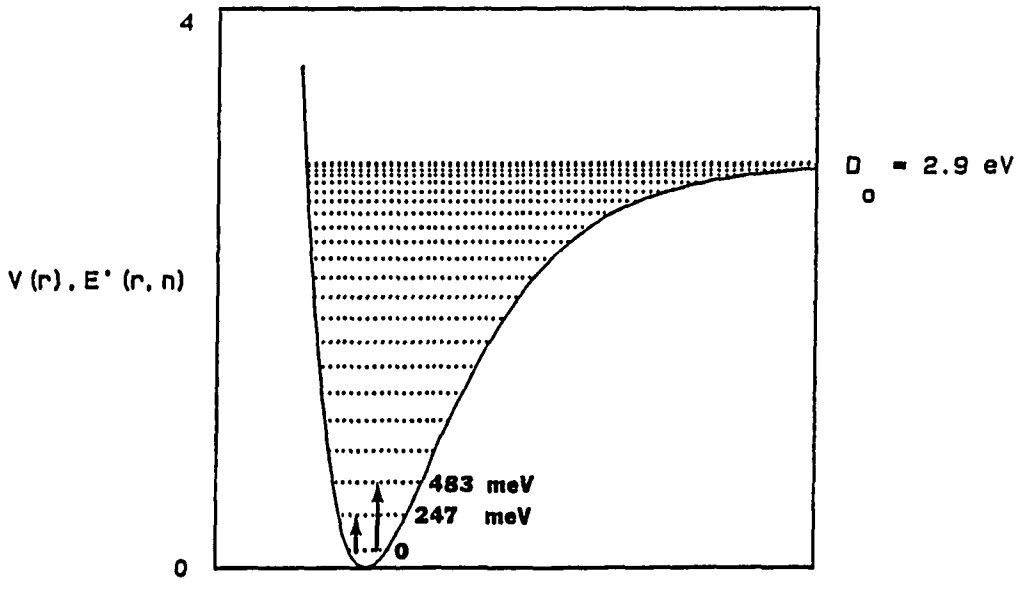

Fig. 4.8 Energy levels of Morse potential and calculated dissociation energy for H/Ge

fundamental. This is due to anharmonicity in the potential energy. The degree of anharmonicity is related to the dissociation energy. The dissociation energy can be obtained by fitting the two transitions via the Birge-Sponer extrapolation to a Morse potential:

$$V(r) = D_o[1 - \exp(-a(r-r_o))]^2 \qquad (4.3)$$

The details for fitting are described in Chapter 2. The results are shown in Fig. 4.8. The peak at 247 meV has been measured many times and is well established. Assuming a conservative estimate of the error in the position of the overtone peak of ±2 meV, a dissociation energy of 2.9±0.5 eV is obtained. This compares to the literature value of 3.3 eV.

Studies were also done on films of a-$Ge_{1-x}C_x$:H that were prepared by rf sputtering of a polycrystalline Ge target in a medium of Ar (9-12 mTorr), H_2 (1-9 mTorr), and C_3H_8 (0-4 mTorr).[25] Fig. 4.9 shows the HREEL spectrum of one of these alloys with 12% C that was sputter-etched clean of surface contaminants. Peaks characteristic of Ge-H and C-H bonds are apparent. The Ge-H wag appears at ~70 meV, the Ge-H stretch appears at ~247 meV, and the C-H stretch appears at ~365 meV. Upon exposure of the surface to atomic hydrogen, the Ge-H modes increase significantly while the C-H modes remain essentially the same. This would seem to indicate that the hydrogen is preferentially etched from the Ge atoms while the carbon atoms remain saturated with hydrogen.

This is consistent with earlier observations on the same films using a slightly different technique.[39] In this technique, line-shape

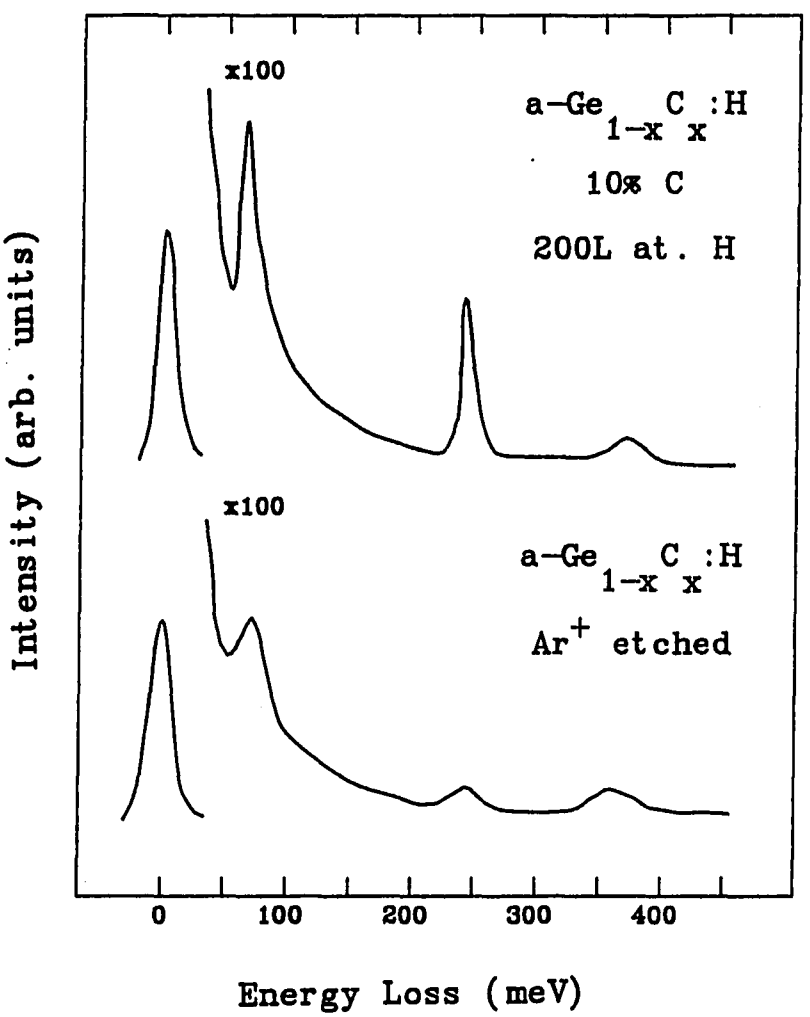

Fig. 4.9 HREELS of Ar^+ etched a-$Ge_{1-x}C_x$:H film and HREELS of same film exposed to 200L H_2 (atomized)

changes were detected in the Ge(MVV) Auger transition at 23 eV following exposure of a-$Ge_{0.9}C_{0.1}$:H and a-$Ge_{0.5}C_{0.5}$:H to atomic hydrogen (see Fig. 4.10). This line shape change confirms that hydrogen is chemisorbed on Ge, inducing a modification in the local density of valence states. No change in the carbon Auger line shape was detected after hydrogen adsorption. Carbon does not seem to react with atomic hydrogen after ion etching. Again this behavior would seem to indicate that hydrogen is preferentially etched from Ge on these films. This would leave an abundance of reactive germanium dangling bonds and relatively few reactive carbon bonds on the surfaces following ion etching.

Several things, then, can be concluded from the hydrogen adsorption experiments. We now summarize these. Molecular hydrogen does not react with the clean Ge surfaces at room temperature. Only after the hydrogen is dissociated on a hot (~1700°C) tungsten filament can the highly sensitive HREELS technique detect hydrogen at the surface. The peaks characteristic of hydrogen adsorption are the Ge-H wag at 70 meV and the Ge-H stretch at 247 meV. Weakening of depolarization effects at the surface cause the energy of the Ge-H (monohydride) stretch mode to increase from its bulk value of 233 meV to 247 meV at both the ordered and disordered surfaces. The HREELS of Ar^+ etched rf sputter-deposited a-Ge:H and a-$Ge_{1-x}C_x$:H indicate preferential removal of hydrogen bonded to Ge by ion etching (although a relatively small amount of hydrogen still remains) and the formation of Ge-H bonds after exposure to hydrogen atoms. Auger line shape measurements also support this conclusion. A dissociation energy for hydrogen on Ge of 2.9 eV was

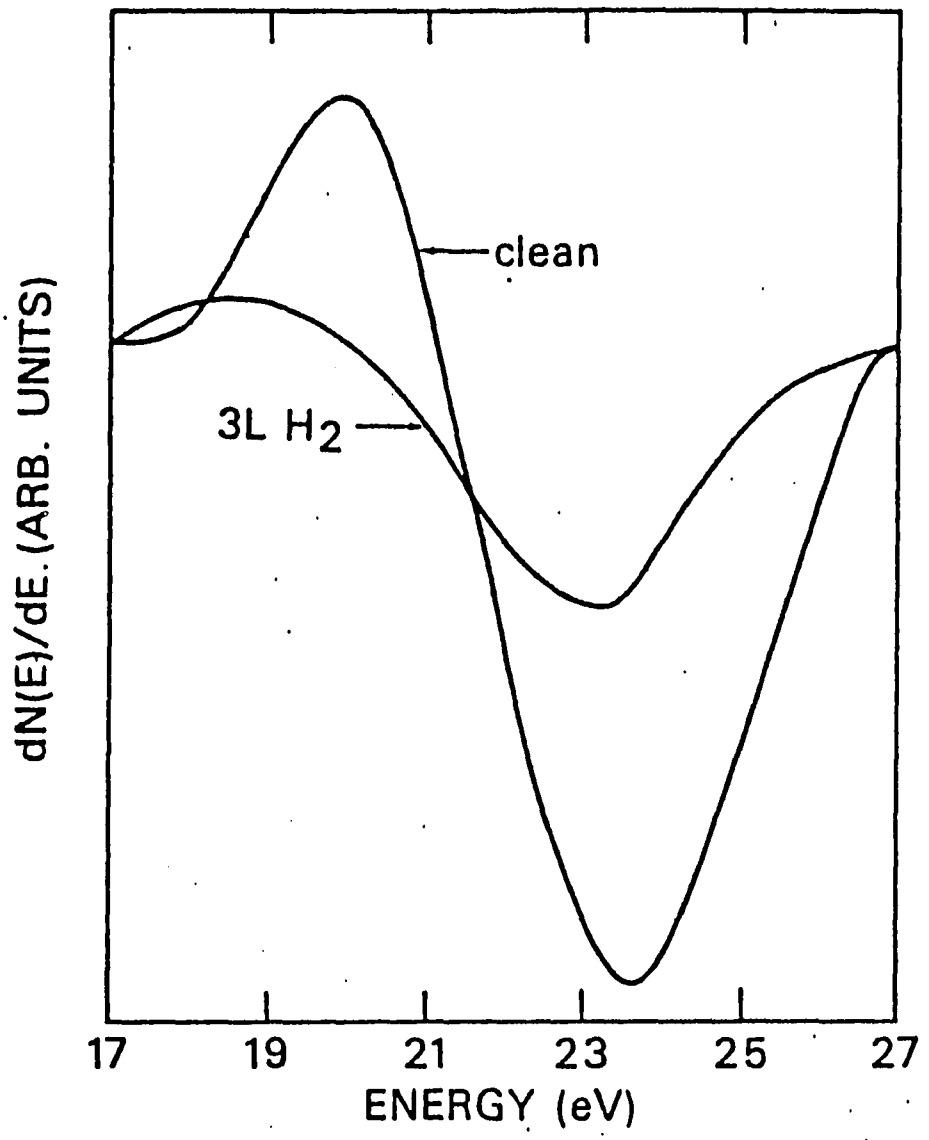

Fig. 4.10 The derivative of the Ge(MVV) Auger transition after background subtraction in clean and hydrogen covered a-$Ge_{0.9}C_{0.1}$:H (ref. 36)

obtained by observing the overtone of the Ge-H stretch and fitting the energy to a Morse potential.

C. Oxygen on Ge

Figure 4.11a exhibits the HREELS of the contaminated Ge(111) surface. The main contaminants are carbon and oxygen. The loss peaks at ~170 meV and ~365 meV correspond to the bending and stretch modes, respectively, of the $-CH_3$ group. The ~112 meV loss is attributed to the asymmetric stretch mode of the Ge-O-Ge group in the native oxide.[37] Upon heating the surface to ~200°C the hydrocarbon contaminants desorb and the spectrum shown in Fig. 4.11b is produced. This loss spectrum is also characteristic of vitreous GeO_2 (ν-GeO_2).[37] A comparison of the HREELS of the native oxide and optical data of ν-GeO_2 is shown in Fig. 4.12.[47] The bulk LO modes occur as peaks in the so-called bulk energy loss function [$-Im(1/\varepsilon)$](where ε is the complex dielectric function of the medium $\varepsilon=\varepsilon_1+i\varepsilon_2$). This function describes losses incurred by electrons travelling through the bulk. The TO modes occur at peaks in the imaginary part of the dielectric constant (ε_2). This function describes losses electromagnetic waves incur as they travel through the bulk. The surface modes shown occur in the gap between the LO and TO modes. Following the bulk IR work of Lucovsky et al.[41] the loss peaks at ~36 and ~70 meV are ascribed to the bond rocking and bond bending modes, respectively, of the Ge-O-Ge group. The rocking mode is the out of plane motion of the oxygen. The bending mode is described as the motion of the oxygen atom in the Ge-O-Ge plane along a line bisecting the bond

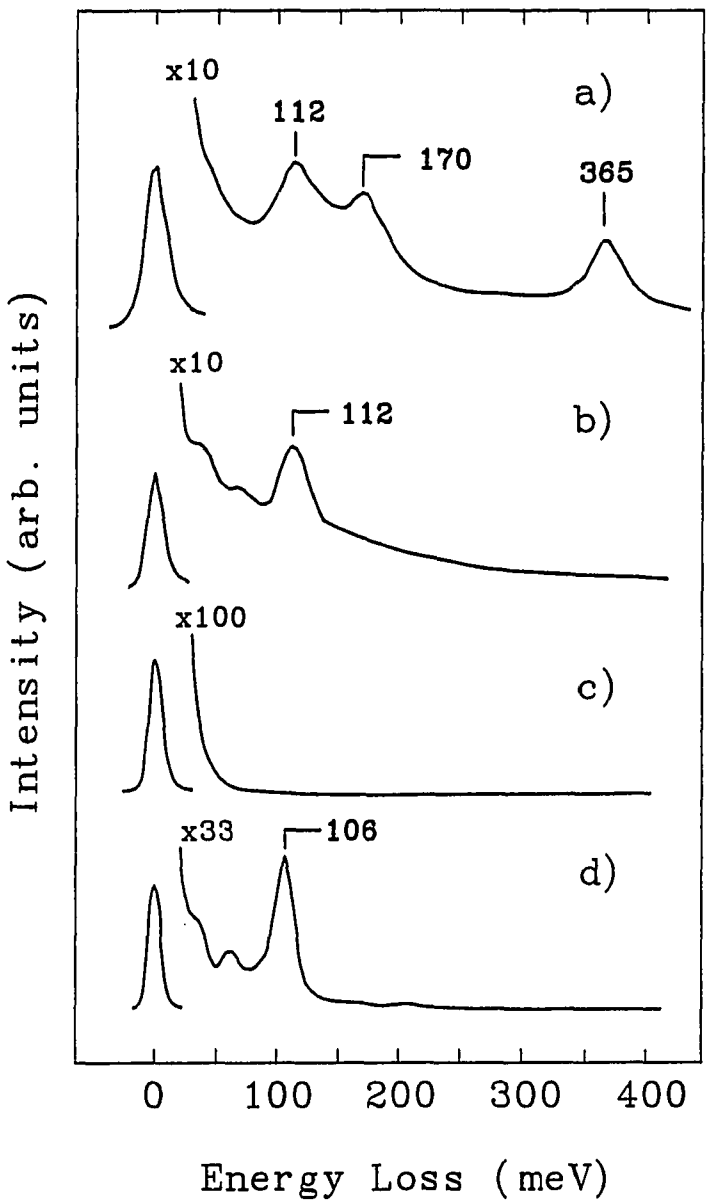

Fig. 4.11 The HREELS of Ge(111) at E_p = 5 eV: (a) The contaminated surface; (b) after heating at 200°C for ~5 minutes (GeO_2); (c) the clean surface; (d) after 10^4L O_2 exposure at 300K

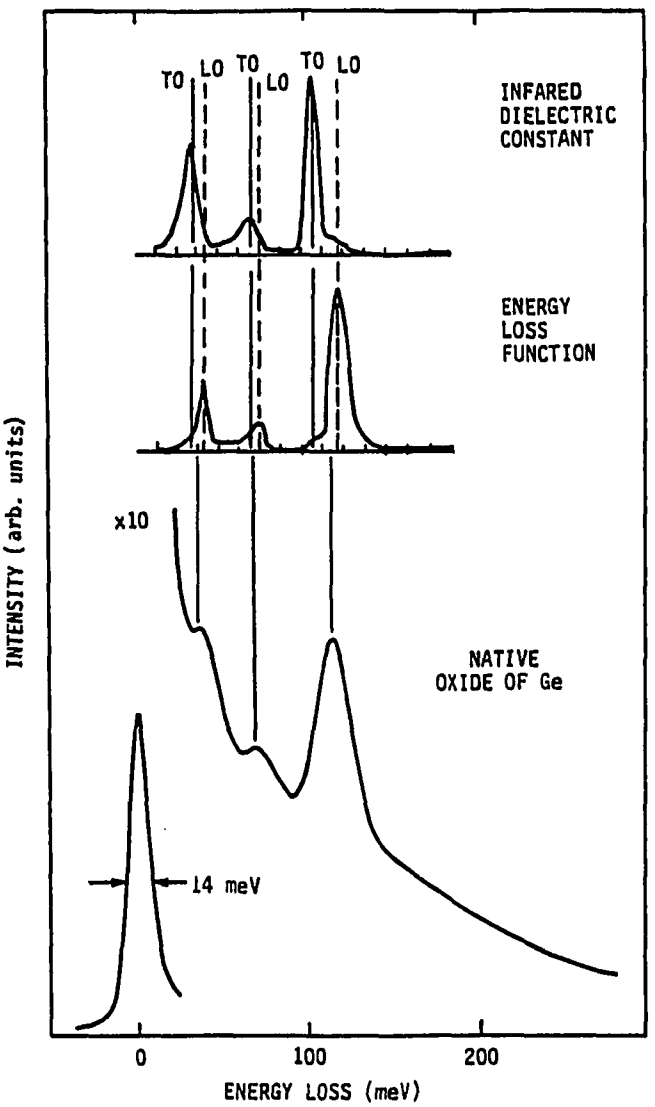

Fig. 4.12 HREELS of the native oxide of Ge and the energy loss function and IR dielectric constant of vitreous GeO_2 (ref. 47)

angle.

Figure 4.11c shows the featureless spectrum of the clean Ge(111) surface, which, when annealed, forms the c(2x8) reconstruction. This is a much lower background spectrum than that obtainable for Si(111), which forms the (7x7) reconstruction. It is believed that on the Si(111)7x7 surface, transitions between the high density of surface states within the gap causes the high background.[1] When these surface states are removed by exposure to atomic hydrogen, the background reduces significantly. From the low background for the Ge(111) surface we conclude that the density of surface states within the gap is much lower.

Exposure of the clean Ge(111) surface to 10^4L O_2 at 300K results in the loss spectrum in figure 4.11d. The loss peaks at ~33, ~62, and ~106 meV correspond, respectively, to the rocking, bending, and asymmetric stretching modes of the Ge-O-Ge group as deduced from IR measurements of GeO_2 and a-Ge:(H,O).[41] Thus, oxygen appears to dissociatively chemisorb in the bridge configuration as is the case for Si(111). This assignment parallels that of the isolated Si-O-Si group in a-Si:(H,O).[42] Thus, similarities are also expected in the HREEL spectra of the O_2/Ge and O_2/Si systems. Indeed for each system three main losses are observed at high coverage. For oxygen covered Si surfaces these modes are at about 50, 90, and 126 meV (see Fig. 4.13). The 90 and 126 meV losses were assigned to the symmetric and asymmetric stretch modes, respectively.[29-31] The surface structure and/or reconstruction of the clean surface seem to have little effect on the positions of the three

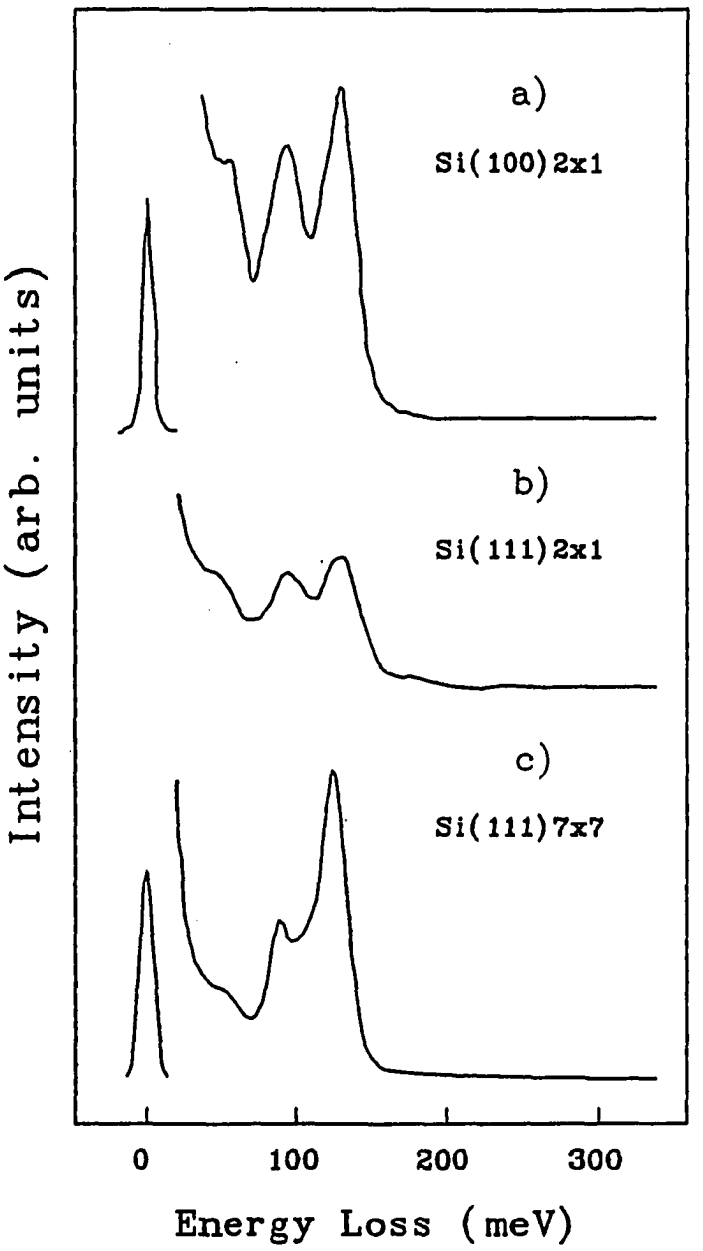

Fig. 4.13 HREELS of O_2 adsorbed on Si near saturation coverage: (a) (ref. 24); (b) (ref. 18); (c) (ref. 23)

peaks. Their relative intensities, however, may be different due to screening effects, with the dipole selection rule suppressing certain modes and enhancing others. In an earlier work[48] Bell et al. assigned the three bands to the rocking, bending, and asymmetric stretch in GeO_2 and SiO_2. However, due to the larger mass ratio between Ge and O as compared to Si and O, the assignment for GeO_2 is better defined and less band overlap occurs. For the following interpretation of our experimental results we use only the asymmetric stretch mode.

Figure 4.14 shows the spectra of Ge(111) exposed to a) 10L, b) 100L, c) 1000L, and d)10^4L O_2. The intensity of the asymmetric stretch mode increases with exposure and the loss frequency shifts from ~98 meV at 10L to ~106 meV at 10^4 L. An increase in the frequency of the asymmetric stretch was also seen in bulk IR measurements of GeO_x films for increasing x.[49] Figure 4.15 shows these IR measurements. These measurements show an approximately linear variation in the asymmetric stretch frequency with x. This increase was attributed to an increase in the average bond angle of the Ge-O-Ge bridges as the oxidation state increases. This is probably the reason for the shift in the asymmertic stretch mode in the HREELS spectra as well. No nonlinearity in the intensity of the peaks as a function of coverage characteristic of dipole-dipole coupling was observed (see Chapter 2).

The IR measurements in a-Ge:(H,O) films show that the asymmetric stretch mode of the isolated bridge Ge-O-Ge configuration appears at 93 meV.[41] This mode appears at 106 meV in the "near-neighbor" Ge-O-Ge configuration in ν-GeO_2.[41] In the HREEL spectra of Ge(111) the

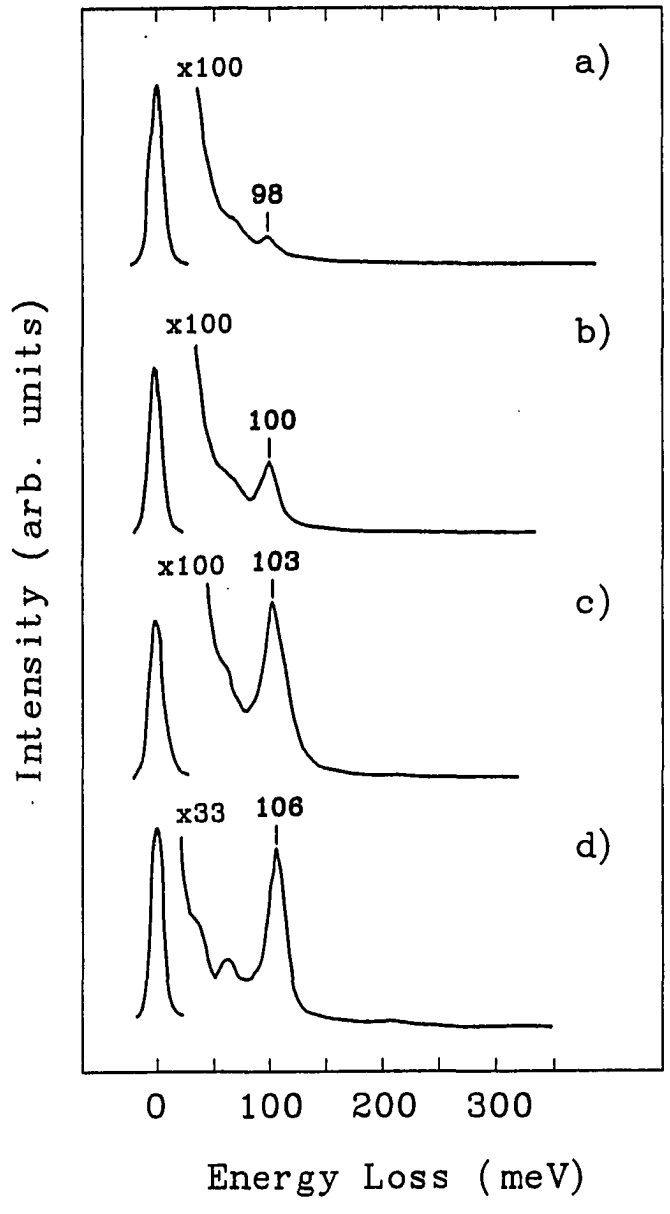

Fig. 4.14 The HREELS of Ge(111) at E_p = 5 eV exposed to O_2 at 300K: (a) 10L; (b) 100L; (c) 1000L; (d)10^4L

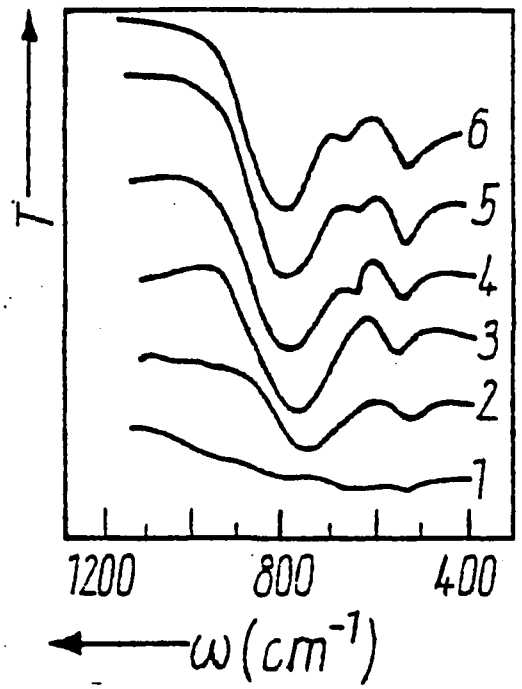

Fig. 4.15 IR spectra of GeO_x films, $0 \leq x \leq 1$ (ref. 49); (1) x=0; (2) x=0.2; (3) x=0.45; (4) x=0.6; (5) x=0.8; (6) x=0.85

respective vibrational modes show up at 98 and 112 meV. Although the shifts of the asymmetric mode with increasing coverage are small, they are reproducible and consistent. Thus, it appears that for an exposure of 10L the dominant oxidation state is +1, i.e., an isolated Ge-O-Ge configuration. The oxidation state then gradually changes (as the number of bonded oxygen atoms increases) to a mixture of +2 and +3 at the 10^4L exposure. The presence of a +3 oxidation state is supported by measurements following consecutive H adsorption, as discussed below.

This interpretation is consistent with recent photoemission studies[33] of O_2 adsorbed on Ge(111) which showed that +1 and +2 oxidation states dominate at exposures below 1000 L and that the +3 oxidation state dominates above 3000 L. The photoemission results of ref. 27 are reproduced in Fig. 4.16. The spectrum shows the Ge 3d photoelectron spectrum of Ge(111) after subtraction of the $3d_{3/2}$ component. This leaves only the $3d_{5/2}$ component and makes it easier to discuss the observed shifts. The large peak at the right corresponds to bulk electrons (no chemical shift) and is taken to be the zero of the scale. The top trace is the spectrum of the native oxide. Here the +4 oxidation state dominates. The second trace shows the photoelectron spectrum of the adsorbed oxide annealed to 400°C. Here the +2 oxidation state dominates. This makes sense since the oxide is known to desorb as Ge=O which is in the +2 oxidation state. The bottom four traces show the clean surface spectrum and the spectra of the surface exposed to 100L, 1000L and 3000L O_2. The +3 state is seen to dominate at high exposures. In another study, however, the results presented in ref. 27

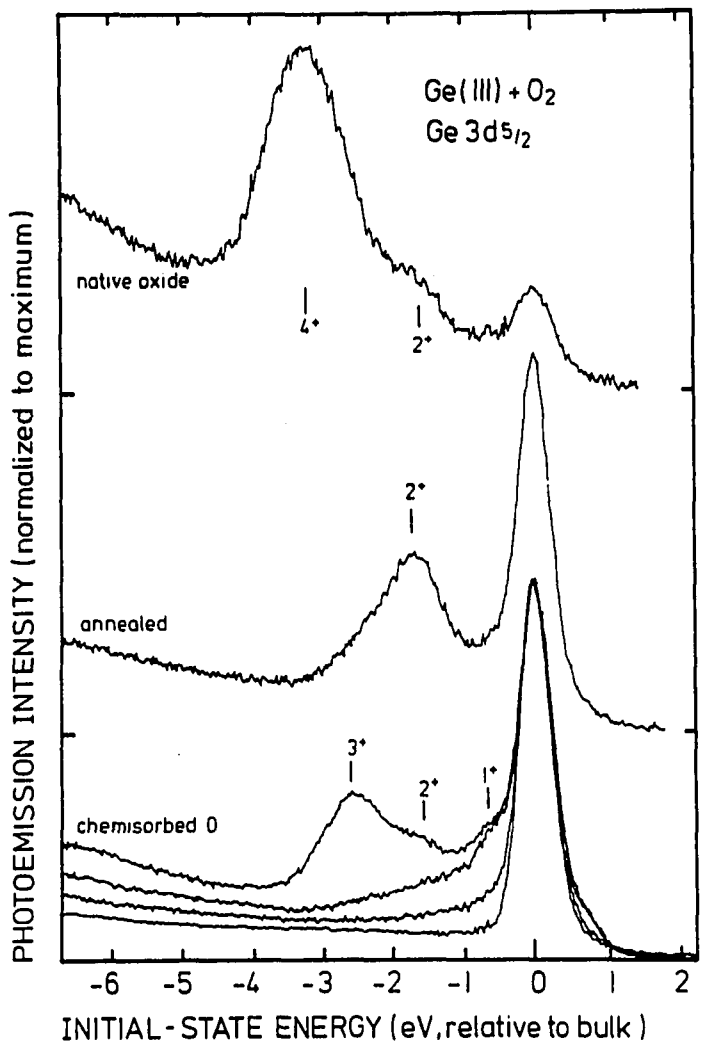

Fig. 4.16 Photoemission results of the room temperature oxidation of Ge (ref. 27); see text for details

were not reproduced, and only a weak +3 oxidation state on Ge(111) was observed.[34] Our results tend to support a dominant +3 oxidation state.

Atomic hydrogen was also used to probe the oxidation states. Figure 4.17a shows the spectrum of the disordered surface pre-exposed to 10^4L O_2 followed by an exposure to atomized 200L H_2. This exposure resulted in saturation coverage of the Ge-H monohydride at the clean surface. For comparison the loss spectrum of a surface exposed to hydrogen only is shown in Figure 4.17c. The losses at ~70 and ~247 meV are the Ge-H wagging and stretch modes, respectively, of the isolated Ge-H bond. The ~140 meV mode is probably an overtone of the ~70 meV loss. In addition to the 247 meV isolated Ge-H stretch mode, a loss at ~255 meV appears on the pre-oxidized surface (Fig. 4.17a). This shift is indicative of a +1 oxidation state with a H-Ge-O-Ge bonding configuration.[38] Figure 4.3 shows this shift for the case of one near-neighbor oxygen atom. Figure 4.4 shows a possible bonding configuration that would give rise to this shift. The relatively intense loss at 247 meV indicates that a large fraction of Ge-H bonds are still isolated, i.e., do not have a near-neighbor oxygen atom. This may indicate a relatively high density of surface dangling bonds and/or deeper penetration of the oxygen and hydrogen at the disordered surface surface. Figure 4.17b exhibits the HREEL spectrum of a pre-oxidized Ge(111) surface (10^4L O_2) exposed to 200L H_2 (atomized). The Ge-H stretch mode is shifted to ~267 meV indicating the presence of the +3 oxidation state[38] and a low density of isolated Ge-H bonds. The existence of a +3 oxidation state at the Ge(111) surface is a result of

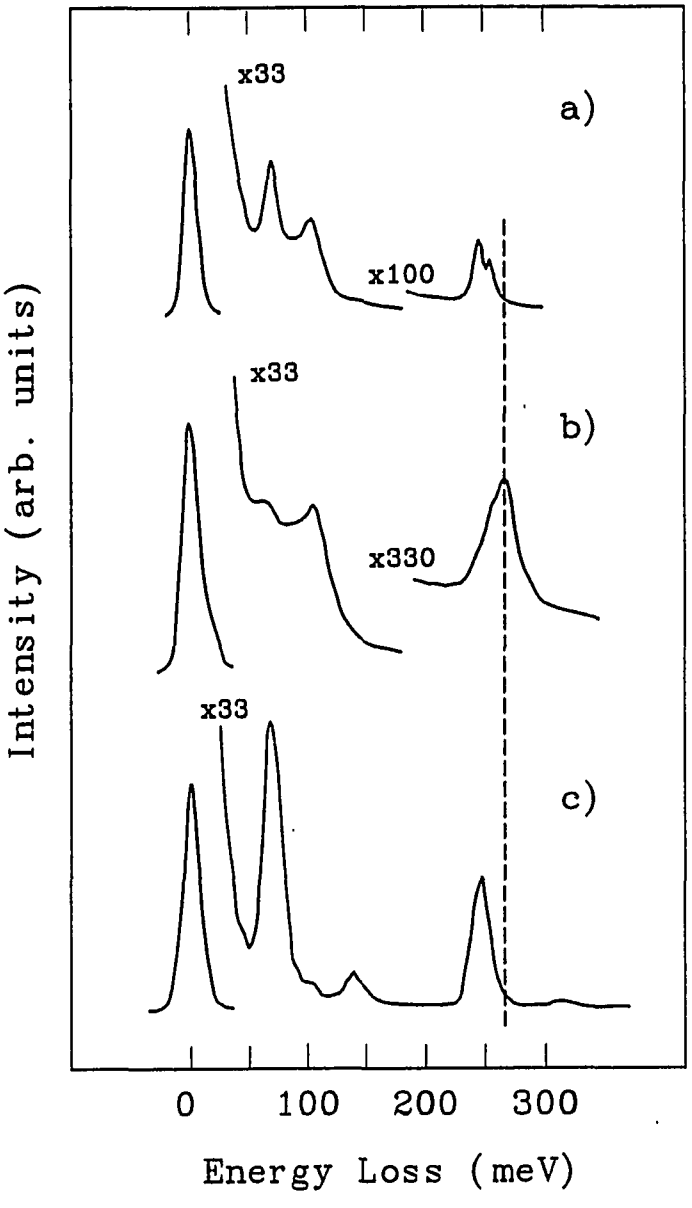

Fig. 4.17 The HREELS spectra at E_p = 5 eV of: (a) a-Ge pre-exposed exposed to 10^4L O_2 followed by atomized 200L H_2; (b) Ge(111) pre-oxposed to 10^4 followed by atomized 200L H_2; (c) a-Ge exposed to atomized 200L H_2

oxygen bonding to surface and subsurface Ge atoms. Again Fig. 4.3 shows this shift, and Fig. 4.4 shows a possible bonding configuration. Oxygen seems to penetrate deeper into the amorphous material creating a dilute Ge-O-Ge bridge structure and leaving the surface available for subsequent hydrogen bonding. Higher oxygen exposures may saturate the surface dangling bonds; however, for exposures higher than 10^4L O_2, other contaminants could not be avoided.

An oxide layer consisting of a dominant +4 oxidation state cannot be produced by O_2 adsorption at room temperature. The asymmetric loss peak at 112 meV typical of the native oxide and υ-GeO_2 (see Fig. 4.11b) was never observed for exposures of up to 10^5 L at 300 K. This is similar to the behavior of Si.[29]

Broughton et al.[10] have found that a peak appears at 115 meV on Ge_xSi_{1-x} alloys exposed to 1L water at 150K and then warmed to room temperature. They have hypothesized that this is due to a surface oxide or suboxide. Our result that the maximum asymmetric stretch energy for oxygen adsorbed on Ge was 106 meV does not support this. Oxygen adsorbed on Si causes a peak at around 126 meV, and so it is unlikely that it is a Si-O mode. A more likely interpretation is that of Papagno et al.[9] who claim that it is the Ge-OH bending mode.

The disordered surface was also studied with valence band and core level EELS. Figure 4.18 shows the EEL spectra of the clean and oxygen covered a-Ge surface at E_p=110 eV. As can be seen, the oxygen induced peak at ~7 eV increases with coverage, similar to observations on single crystals.[36,50] At E_p=110 eV, the surface plasmon at 10 eV remained

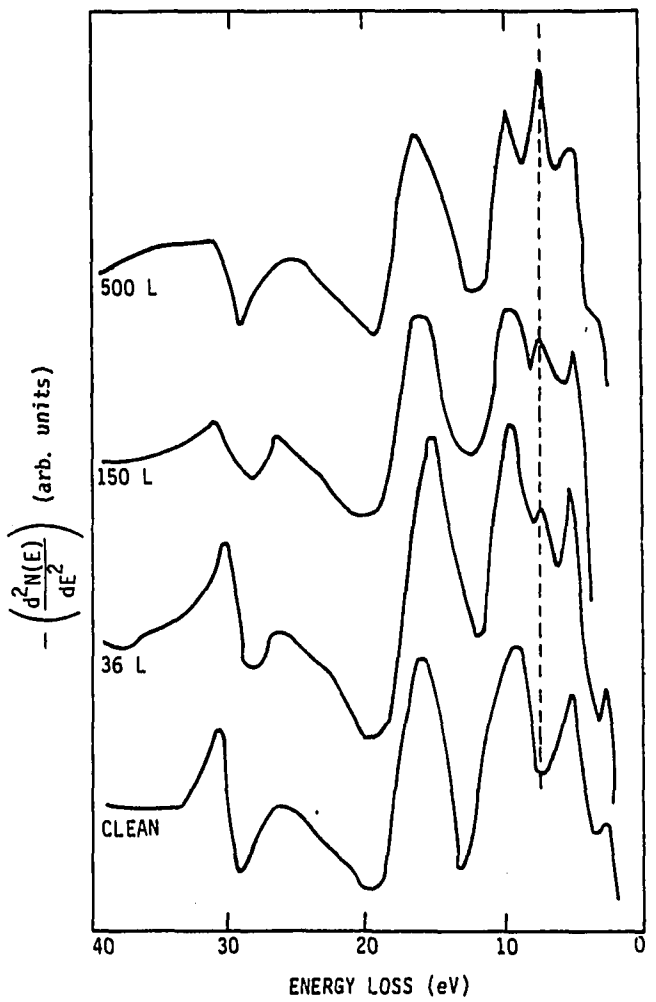

Fig. 4.18 EELS of clean and oxygen covered a-Ge at E_p=110 eV

unchanged following oxygen chemisorption. This behavior is unclear, since on single crystal surfaces,[36,50] a reduction in the surface plasmon was observed as was the case in a-Ge at higher E_p values. The 15-eV loss peak is the bulk plasmon, and the ~30 eV loss results from a single electron transition from Ge 3d core levels. In Ge(100) and Ge(111), this transition is to empty dangling bond surface states, and indeed this loss diminishes and eventually disappears following exposure to various adsorbates.[51,52] In addition, several other well-resolved loss peaks are observed on single crystals in the 29 to 35 eV range. These additional losses result from transitions from the Ge 3d levels to the conduction band.[51,52] In the amorphous samples the 30-eV loss is broad and only slightly affected by adsorbates indicating the presence of a high density of additional energy levels in the vicinity of the dangling bond surface states. These states, evidently, do not participate in oxygen bonding at the surface.

HREELS studies of oxygen adsorption on the previously described a-$Ge_{1-x}C_x$:H films show similar results. Deeper penetration of the oxygen results in a dilute bridge configuration and lower oxidation states relative to similarly exposed single crystal surfaces. This conclusion is supported by Auger and electronic EELS measurements (see below).

The oxidation of a-$Ge_{1-x}C_x$:H films was also studied using valence band and core level EELS. An oxygen induced loss peak appears at 7 eV as was the case for a-Ge:H and single crystals of Ge. However, this loss appears to be enhanced as the carbon content of the film increases.

This effect can be seen in Fig. 4.19 where the EEL spectra of three samples containing various amounts of carbon at a constant surface coverage are shown. On Ar^+ sputter-etched a-$Ge_{1-x}C_x$:H surfaces a peak appears at 8 eV for $0.24 \leq x \leq 0.5$.[40] This peak was attributed to a Ge-C induced loss since it is absent in both a-Ge:H and a-C:H. The increase in the 7-eV loss relative to the bulk plasmon could be the result of a combination of the oxygen induced loss and this Ge-C bond induced loss which increases with the carbon content. However, the relative narrow width of the 7-eV loss argues against the above explanation. The 8 eV Ge-C induced loss could not be resolved from the π-plasmon induced loss which appears at ~5 eV in a-$Ge_{1-x}C_x$:H films with $x \geq 0.25$.[40] However, the narrower oxygen induced loss was clearly observed in films with $x=0.5$ (the highest x value used in this study). As of now, the exact origin of this enhancement is unknown.

Figure 4.20 exhibits the oxygen content as a function of oxygen exposure for a-Ge, a-$Ge_{0.9}C_{0.1}$:H, a-$Ge_{0.75}C_{0.24}$:H, and a-$Ge_{0.67}C_{0.33}$:H. This figure is used to compare the behavior of the various samples towards oxygen exposure, although the sensitivity factors may change as x changes. The O(KLL)/Ge(LMM) and O(KLL)/ Ge(MNN) ratios versus exposure in a-Ge show the same qualitative behavior. In Fig. 4.20 the Ge(LMM), O(KLL), and C(KLL) Auger transitions were used to calculate the composition. It appears that the Ge/C ratio in the clean alloys is not affected by ion etching. As can be seen, the behavior is similar for all films, despite the significant reduction in the Ge content in the alloys. In addition, saturation was not reached up to an exposure of

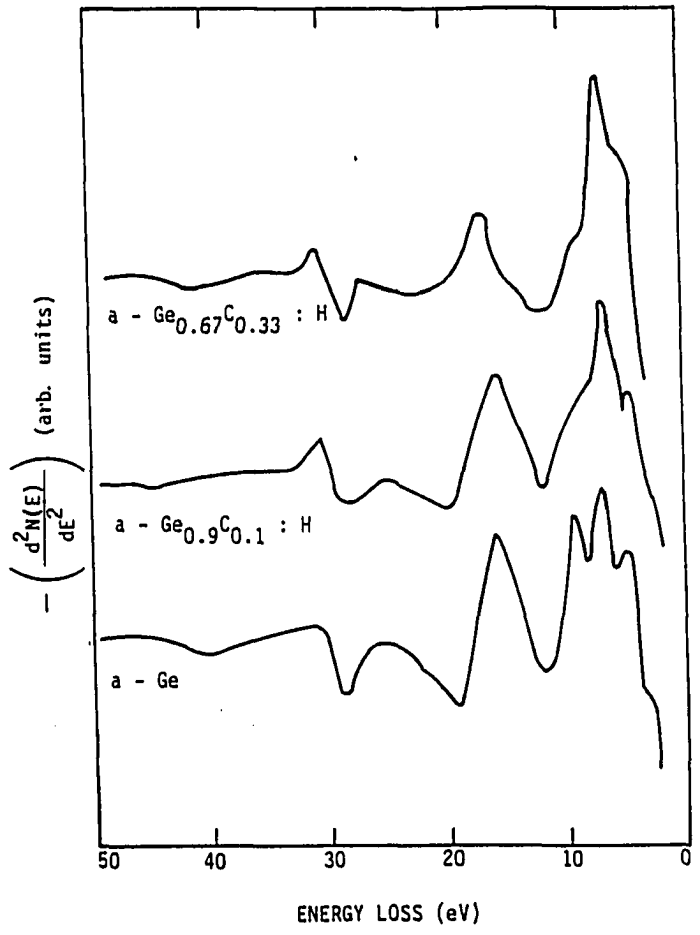

Fig. 4.19 EELS of oxygen exposed (~ 500L) a-$Ge_{1-x}C_x$:H (x = 0, 0.1, and 0.33) at E_p=110 eV

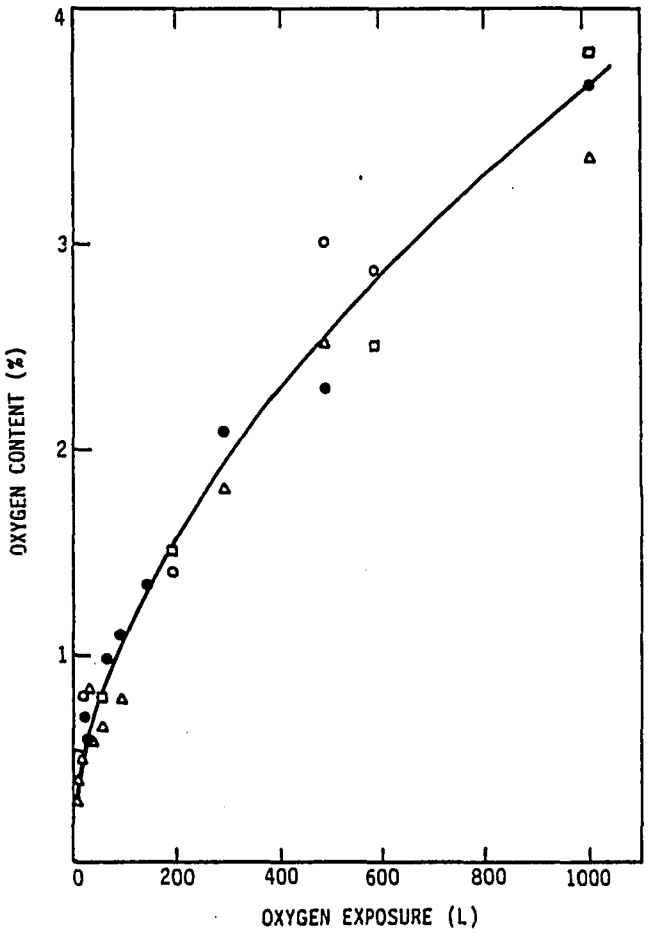

Fig. 4.20 Oxygen coverage as a function of O_2 exposure for a-$Ge_{1-x}C_x$:H ; ●: x=0, Δ: x=0.1, o: x=0.25, □: x=0.33

1000L O_2, and the coverage appears to continue to increase gradually following an initial sharper increase. Samples left in the vacuum chamber for long periods indicated a much higher level of C and O contaminations. The similarity in coverage versus exposure behavior of a-Ge and the alloys suggests that exposure of a-Ge to O_2 up to 1000L results in submonolayer coverage. In addition, the presence of carbon does not seem to alter the sticking coefficient. The fact that the surface is only partially covered even for high exposure tends to support the HREELS results. It should be noted that carbon bonds in the alloy appear to be nonreactive. There is no evidence of C-O bonds in HREEL spectra following exposure to O_2 molecules. Previous studies[39,40] and the present one similarly indicate that C atoms do not react with hydrogen atoms. Surfaces of amorphous carbon (x=1) were also nonreactive and indicated a very low sticking coefficient for oxygen in comparison to the Ge surfaces.

No change in the Ge(MVV) Auger line shape was observed following oxygen dosing, whereas a hydrogen induced broadening was previously observed.[39] The lack of shift in the Ge(MVV) transition in oxygen covered surfaces may indicate low oxidation states (mainly +1) where the core-level shifts lie within the resolution of the experiment. This is in agreement with the conclusions drawn from HREELS experiments.

The main results of the oxygen adsorption experiments are now summarized. The HREELS experiments indicate for oxygen adsorption on Ge at room temperature, a dissociative bonding of oxygen and a Ge-O-Ge bridge structure. Near saturation the Ge(111) surface forms a +3

oxidation state. The disordered surfaces, including the carbide films, tend to form a dilute bridge structure and a dominant +1 oxidation state for similar exposures. No evidence of C-O bonding was observed in the carbide films following exposure to oxygen.

D. NO on Ge

Figure 4.21a shows the loss spectrum of Ge(111) exposed to 10^4L NO. Losses are observed at about 62, 100, and 193 meV. The 62 meV loss is the bending mode of the Ge-O-Ge structure. The 100 meV loss is ascribed to the Ge-O-Ge asymmetric stretch mode with some contribution from a Ge nitride precursor as later described. The peak at ~193 meV is probably an overtone of the 100 meV loss. The frequency and intensity of the 100 meV loss are lower than those of the surface exposed to 10^3 to 10^5 L O_2. The lower frequency of 100 meV suggests a lower oxidation state (mainly +1) at the NO-exposed surface as compared to the O_2-exposed surface where the +3 oxidation state dominated. The lower intensity is consistent with the relatively lower oxygen content as revealed by Auger analysis. The HREEL spectrum of Ge(111) exposed to 10^5L NO is identical to that of the surface exposed to 10^4L NO. This may indicate that the surface is saturated, although a direct correlation between coverage and intensity does not necessarily exist.[53] Also, when the Ge(111) surface is exposed to 10^4L NO and then to 10^4L O_2, the intensity and the position of the 100 meV loss are retained. Similar to that of the O_2-exposed surface,[37] the electronic loss spectrum (not shown) indicates

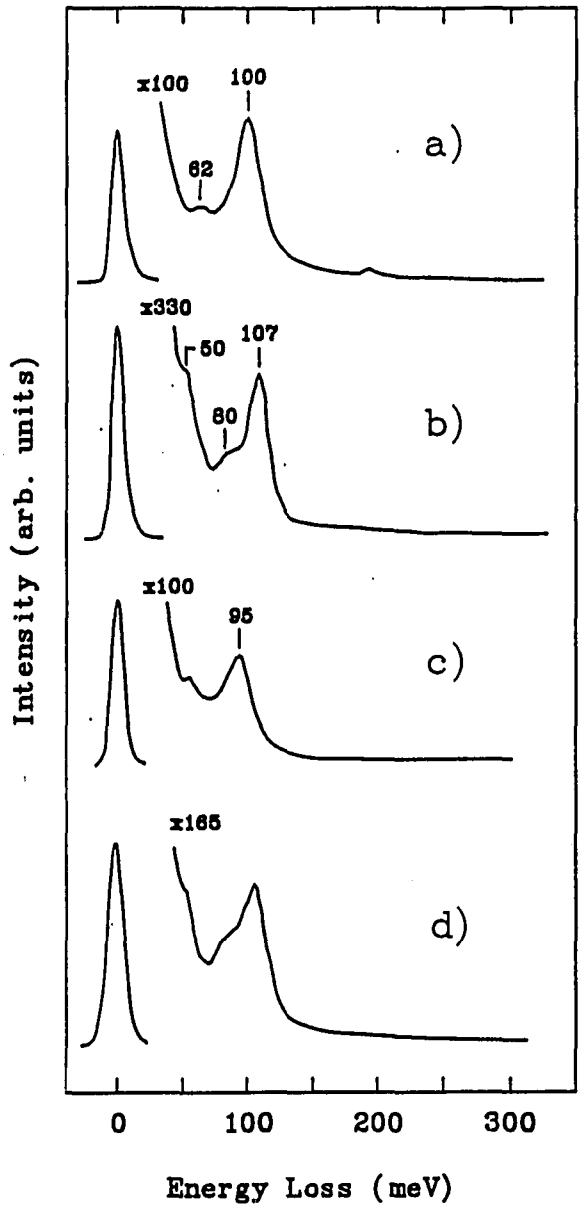

Fig. 4.21 The HREELS of Ge(111) at E_p = 5 eV: (a) surface exposed to 10^4L NO at 300K; (b) 10^4L NO-exposed surface annealed at 550°C for 30 min; (c) surface exposed to N_2 passed through a differentially pumped ion gun; (d) N-exposed surface heated to 550°C

only an oxygen related loss at ~7 eV. Yet Auger analysis following exposure of Ge(111) and a-Ge to NO indicates the presence of both N and O on the surface. The oxygen and nitrogen concentrations are equal, within experimental error, at the lower exposures ($\leq 10^3$L). At higher exposures oxygen contaminants increase the total oxygen content. These contaminants are present due to the use of the turbo-molecular pump as described in the experimental section. Nitrogen related losses are not resolved from those of oxygen as described below. The HREELS experiments do not show any losses related to molecular NO or to nitrosyl complexes. The same behavior was observed for NO/Si(111) at room temperature.[31] However, the presence of bonded, dipole inactive, molecular species cannot be ruled out.

These results indicate that at 300K NO dissociates, and N and O bond primarily at the first layer of Ge atoms. Oxygen penetration, necessary for creating the +3 oxidation state, does not occur, in contrast to observations at Ge(111) exposed to O_2. The presence of N and O atoms at the Ge(111) surface, for coverages close to or at saturation, prevents oxygen penetration. The situation is somewhat different at the disordered surface. The increase in the loss intensity following exposure to 10^5L NO indicates that the surface is not yet saturated, contrary to the similarly treated Ge(111) surface. Still, the loss at ~100 meV indicates a predominant +1 oxidation state suggesting dominant surface bonding of N and O. This behaivor is probably due to a higher density of dangling bonds at the amorphous surface. Exposure of the disordered surface to 10^4L NO and then to 10^4L

O_2 results in an increase in the intensity of the Ge-O-Ge vibrational modes but no shift in the energy loss of the asymmetric stretch mode. This is consistent with the description of a high density of surface dangling bonds and deeper penetration of oxygen at the disordered surface. The NO-covered disordered surface also seems to be more reactive to water impurities. Figure 4.22 shows the spectrum of the disordered surface exposed to 10^4L NO at high background pressure. Note the high presence of N-H and O-H stretch modes at 410 meV and 450 meV, respectively. Also note the absence of a Ge-H mode at 247 meV and the absence of Ge-OH modes. This is probably due to the fact that the Ge bonds have been saturated with N and O atoms, leaving these atoms to react with the water. As mentioned in the introduction to this chapter, clean, single crystal surfaces of Ge do not react with water at room temperature.

Figure 4.21b exhibits the loss spectrum of the 10^4L NO-exposed Ge(111) surface after annealing to 550°C for 30 minutes. As previously mentioned in the experimental section, oxygen is removed from the surface by this treatment. The HREEL spectrum shows three losses at 50, 80, and 107 meV. We attribute theses losses to vibrational modes of germanium nitride by comparison with IR spectra of α- and β-Ge_3N_4.[54] This comparison is shown in Fig. 4.23. This assignment parallels that of similarly treated Si(111)[31] where very similar peaks were found to coincide with the IR spectra of α- and β-Si_3N_4.[55] This comparison is shown in Fig. 4.24. The electronic EEL spectrum of the heated 10^3L NO-exposed sample is similar to that of the clean surface with Auger

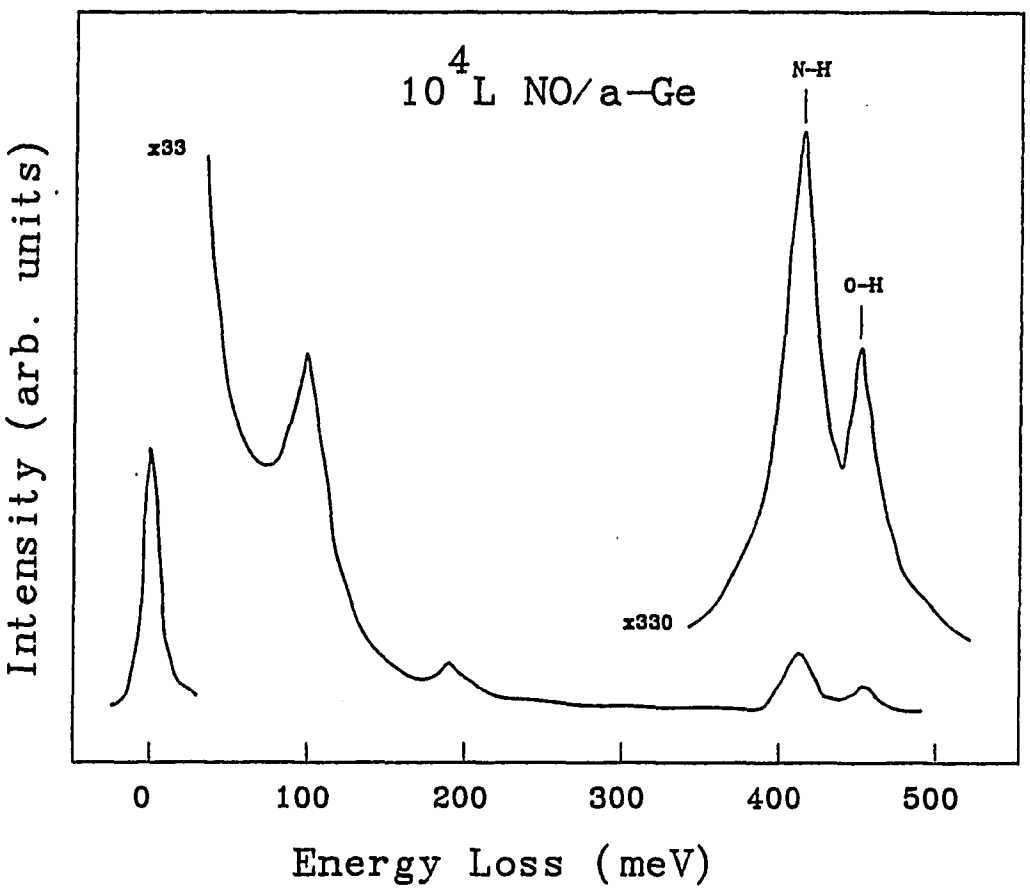

Fig. 4.22 HREELS of a-Ge exposed to 10^4L NO at high background pressure

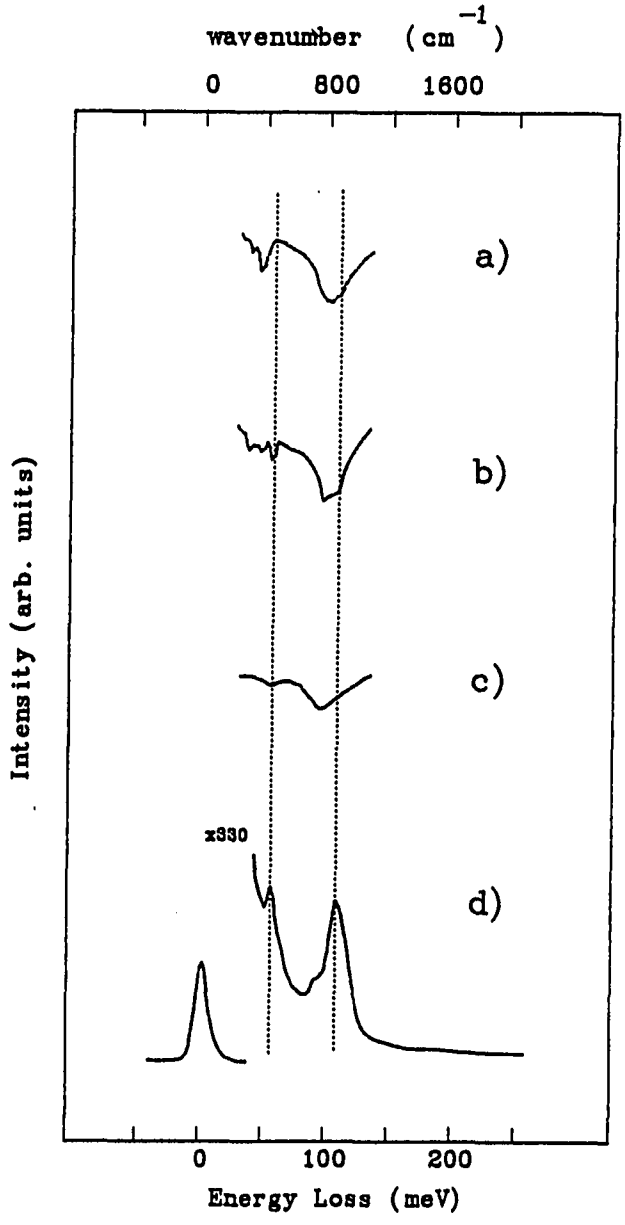

Fig. 4.23 A comparison of IR spectra (ref. 54) and HREEL spectra: (a) IR spectrum of β-Ge_3N_4; (b) IR spectrum of α-Ge_3N_4; (c) IR spectrum of a-Ge_3N_4 film; (d) HREELS of nitrogen modes on Ge(111)

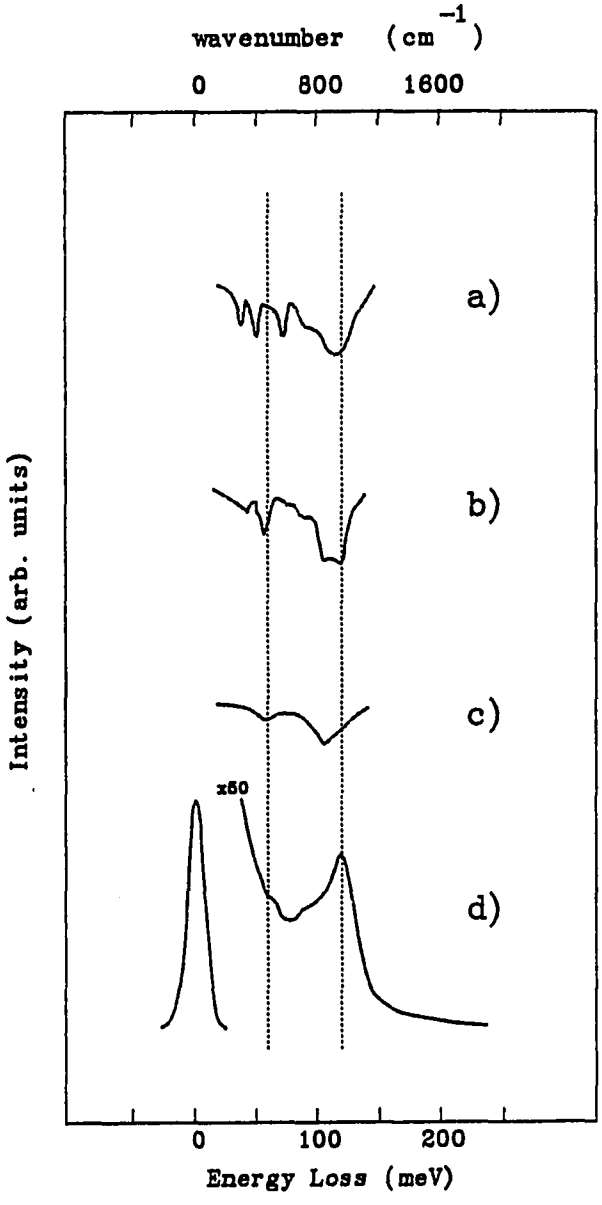

Fig. 4.24 A comparison of IR spectra (ref. 55) and HREEL spectra: (a) IR spectrum of β-Si_3N_4; (b) IR spectrum of α-Si_3N_4; (c) IR spectrum of a-Si_3N_4 film; (d) HREELS of nitrogen modes on Si(111) (ref. 25)

analysis showing ~2% nitrogen present. This behavior is addressed later.

The nitride phase can also be formed by exposure of the Ge surfaces to atomized and ionized N_2 and subsequent annealing to ~550°C. Nitrogen atoms and/or ions are needed because the Ge surfaces are very non-reactive toward molecular nitrogen at room temperature. Figure 4.21c shows the spectrum obtained by exposing the surface to nitrogen passed through a differentially pumped ion gun. This figure shows that nitrogen is bonded initially in a precursor state, indicated by the peak at 95 meV. The structure of this precursor Ge nitride is unknown. This peak is unresolved from the Ge-O-Ge asymmetric stretch loss at the NO-exposed surface. The HREEL spectrum of the N-exposed surface is shown in Fig. 4.21d. Note that the peak positions and relative intensities are identical to those of the NO-exposed and annealed surface. This supports the idea that the precursor state transfers into the nitride bond after annealing. After annealing, the integrated intensities of the loss peaks of the N-exposed surface are roughly twice that of the NO-exposed surface. This makes sense since exposure to NO results in only half coverage at saturation for both N and O, while exposure to N results in full coverage for N at saturation. Similar behavior was reported for Si(111).[56] Here the precursor appeared at 102 meV. Silicon, however, passed through an intermediate state when annealed between 1240K and 1350K, and a relatively complex HREEL spectrum was obtained with peaks at 60, 91, 120, and 141 meV. Above 1350K the HREEL spectrum shows the structure of silicon nitride. Germanium has not been

observed to pass through this intermediate state although it may exist in a very narrow temperature range.

E. N_2O on Ge

In contrast to NO, Auger analysis of N_2O-exposed Ge surfaces reveals the presence of surface oxygen only. This indicates that N_2O decomposes at the surface into chemisorbed oxygen and desorbed N_2. The HREEL spectra for exposures of up to 10^5L exhibit the 98 meV asymmetric stretch mode of Ge-O-Ge indicating a predominant +1 oxidation state. This is probably a result of bonding mainly at the top surface layer, in accordance with bonding of atomic oxygen from N_2O to the top surface layer of Ge(100).[35] Saturation coverages are not achieved for exposures as high as 10^5L. Subsequent exposure to 10^4L O_2 results in the +3 oxidation state at Ge(111), whereas the oxidation state remains +1 at the disordered surfaces. This is consistent with the behavior of the two surfaces as discussed earlier. The reactivity of the disordered surface towards N_2O is higher than that of Ge(111). This suggests that the decomposition of N_2O is enhanced by an increased density of dangling bonds and surface defects. Heating the surfaces to 550°C produces a featureless HREEL spectrum indicative of a clean surface. This indicates the absence of bonded nitrogen and, thus, supports the results of the Auger analysis. Previous studies[35] using differential reflectometry of N_2O on Ge(100) indicated that the atomic oxygen released from N_2O bonds primarily to surface Ge atoms at dangling bonds

and dimer sites. This behavior is similar to N_2O adsorption at Si(100).[57]

F. Activated O_2, NO, and N_2O on Ge

As previously mentioned in the experimental section, experiments in the Auger system had to be performed with the ion pump disconnected to avoid activation of NO, N_2O, and N_2. If, however, the surfaces are exposed to these molecules while pumping with the ion pump instead of using the turbo-molecular pump, a different behavior than earlier described is observed. Nitrogen is detected at the surfaces following exposure to N_2 and N_2O, in contrast to previously reported observations at Ge(100)[35] and Si(100).[57] In addition, the surfaces' reactivity towards NO and N_2O increases. The oxygen content is higher than that originating from similar exposures of O_2, but smaller by a factor of 2 to 3 from the nitrogen content. Using the activated species therefore enables the identification of the nitrogen-related losses in the electronic loss spectrum. We can also learn about the nature of the bonding.

Figure 4.25a shows the electronic EELS of clean Ge(111) at E_p=185 eV. The main losses are at about 5, 9, 15, and 30 eV. The 5-eV loss results from valence band to conduction band transitions. The 9- and 15- eV losses are the surface and bulk plasmons, respectively. In other studies, losses in the range 29-35 eV with E_p=100 eV were attributed to transitions from 3d core levels to the conduction band with a loss at

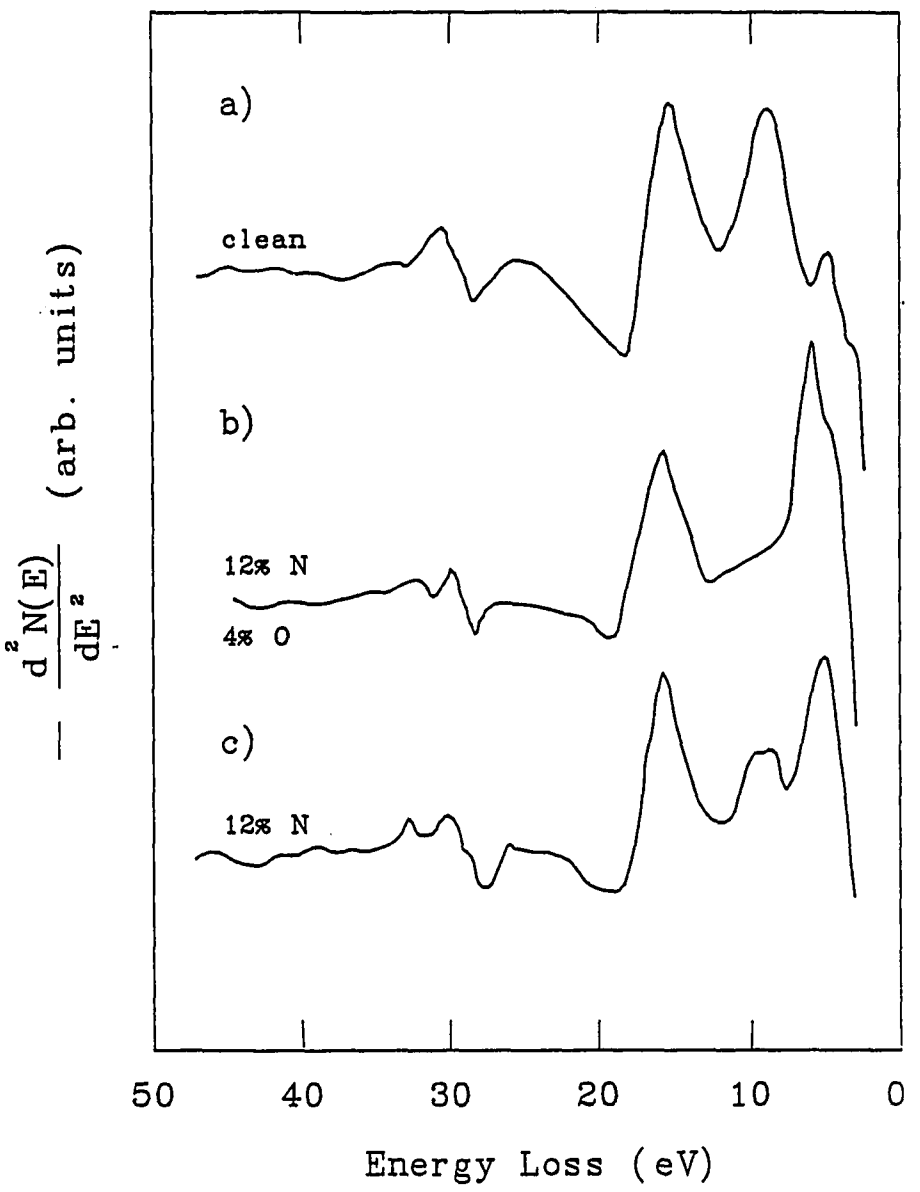

Fig. 4.25 Electronic EELS of Ge(111) at E_p = 185 eV: (a) clean surface; (b) surface exposed to activated 750 L N_2O; (c) activated N_2O-exposed surface heated to 500°C for 3 minutes

~30 eV resulting from transitions to empty dangling bond surface states.[51,52] In Fig. 4.25a, the 30-eV loss at E_p=185 eV also contains contributions from this latter transition (see below). Exposure of Ge(111) to 750L activated N_2O results in the loss spectrum shown in figure 4.25b. Auger analysis reveals 4% oxygen and 12% nitrogen. As can be seen the 30-eV loss is resolved from the 33-eV loss that is associated with excitations from 3d core levels to the conduction band.[51,52] For higher exposure (not shown) the 30-eV loss is clearly diminished. The surface plasmon decreases and a new loss at 6 eV appears. This new loss is unresolved from the 5-eV loss of the clean surface. Upon heating the surface to ~550°C for ~3 minutes the oxygen desorbs whereas the nitrogen content remains unchanged (~0.4-0.5 of the saturation coverage). The loss at ~9 eV increases and the 6-eV loss reduces and shifts to ~5 eV (Fig. 4.25c). Note that the 5-eV loss is now more intense than that of the clean surface. This spectrum is similar to that obtained for the activated N_2-exposed surface, except that the coverage, and therefore the intensity, of the loss peaks are lower for similar exposures. These results indicate that the new loss at ~5 eV is nitrogen-related. This loss can not be uniquely identified in the presence of oxygen. Also, it cannot be observed for low nitrogen coverage due to the 5-eV loss seen in the loss spectrum of the clean surface (see figs. 4.25 and 4.26). The clear reduction of the 30-eV loss at higher coverages suggests that the nitrogen bonds to surface dangling bonds that are associated with this loss, as is the case for oxygen, carbon, and other contaminants on Ge(111).[51]

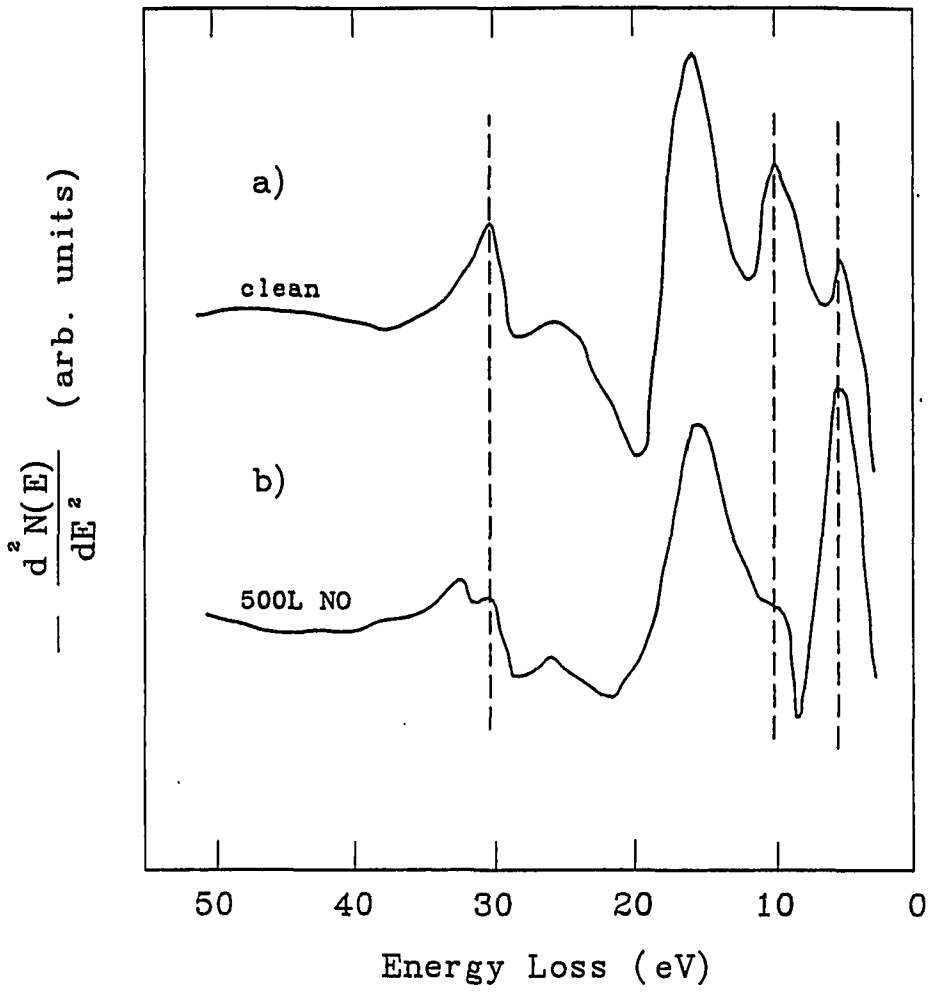

Fig. 4.26 Electronic EELS of a-Ge at E_p = 185 eV: (a) clean surface; (b) surface exposed to activated 500L NO

Figure 4.26 shows the EELS at E_p=185 eV of the clean a-Ge and of the surface exposed to 500L activated NO. Auger analysis reveals ~11% N and ~6% O. The ~30-eV loss here was believed to be the result of transitions from 3d core levels to the conduction band mainly,[39] but as shown below transitions to empty dangling bond states also contribute to its intensity. As can be seen the 30-eV loss is reduced and resolved from the 33-eV loss following adsorption as is the case for Ge(111). In addition, the surface plasmon is reduced and a new loss (unresolved from the 5-eV loss) appears at ~6 eV. The 6-eV loss is a combination of the oxygen (~7 eV) and nitrogen (~5 eV) induced losses. The same behavior is observed for E_p of 135 eV and for E_p of 110 eV. The reduction in the intensity of the 30-eV loss indicates that it is also associated with transitions from 3d core levels to empty dangling bond surface states. This reduction together with that of the surface plasmon is consistent with oxygen and nitrogen bonding mainly at the first layer of Ge atoms, probably to surface dangling bonds. Previous experiments[31] on a-Ge exposed to O_2 and hydrogen atoms did not result in a decrease in the 30-eV loss intensity, in contrast to observations at single crystal surfaces.[50,51] This behavior was interpreted by suggesting that the 30-eV loss at a-Ge contains only a relatively small contribution from transitions to empty dangling bond surface states. In addition, in the previous work,[37] the surface plasmon intensity was retained at E_p=110 eV but reduced at higher E_p values. This reduction, however, was relatively small. The results presented in Fig. 4.26 indicate a reduction of the 30-eV loss at the a-Ge surface upon exposure to

activated NO. The observed difference between adsorption of O_2, H, and NO suggests differences in surface coverage and may support earlier conclusions that oxygen originating from O_2 penetrates into the amorphous surfaces, leaving an unsaturated surface,[37] and thus an unaffected 30-eV loss. Hydrogen atoms may create dangling bonds by inducing the breaking of weak Ge-Ge bonds that are known to exist in a-Ge.[39] In contrast nitrogen and oxygen from activated NO (as well as N_2O) bond primarily at the first surface layer and terminate dangling bonds. Dissociation of molecular species at the top layer may explain the observed surface bonding. This conclusion was also drawn using non-activated molecules from oxidation states derived from HREELS experiments and from consecutive exposures to NO and O_2 molecules. For higher exposures a new loss at ~10 eV appears. This may be a nitrogen-related loss, as it is absent when the surface is exposed to O_2.

G. Mg_2X Compounds

The compounds Mg_2Sn, Mg_2Ge, and Mg_2Si are narrow-gap semiconductors that crystallize in the (cubic) antiflourite structure. They have band gaps at 0K of 0.33, 0.74, and 0.77, respectively. They have three atoms per unit cell implying two sets of optical phonon branches. One set is infrared active, and the other is Raman active. The IR active branch has been studied by McWilliams and Lynch[58]. The Raman active branch has been studied by Buchenauer and Cardona[59]. The IR-active modes are split by the Couloumb field into TO and LO modes. In high resolution electron

energy loss spectroscopy the electron couples to the infrared active modes to form the so-called Fuchs-Kliewer surface modes. Surface modes occur between the TO and LO modes and are given by equation (2.9):

$$\omega_S = \omega_{TO} \cdot \left(\frac{\varepsilon_o + 1}{\varepsilon_\infty + 1} \right).$$

This is the so-called Lyddane-Sachs-Teller relation as applied to surface scattering. It will be used to relate the surface modes to bulk optical properties.

Fig 4.27 shows the HREEL spectra of the native oxide of these compounds heated to 200°C to desorb any carbon contaminants. The surface optical phonons occur at 29, 32, and 40 meV for Mg_2Sn, Mg_2Ge, and Mg_2Si, respectively. Table 4.1 shows the optical data obtained by various groups. All data are from reference 58 except as noted.

Table 4.1 Optical constants of Mg_2X compounds

Compound	ω_{TO}(meV)	ω_{LO}(meV)	ε_∞	ε_o
Mg_2Si	33	41	13.3	20.0
Mg_2Ge	26	30[a]	13.9	18.5[b]
Mg_2Sn	23	29[a]	17.0	27.0[b]

[a]Reference 59.

[b]Calculated.

The surface optical phonon frequencies (rounded to the nearest meV) calculated from these data are 40, 30, and 29 meV for Mg_2Si, Mg_2Ge, and Mg_2Sn, respectively. Because the optical constants are relatively large

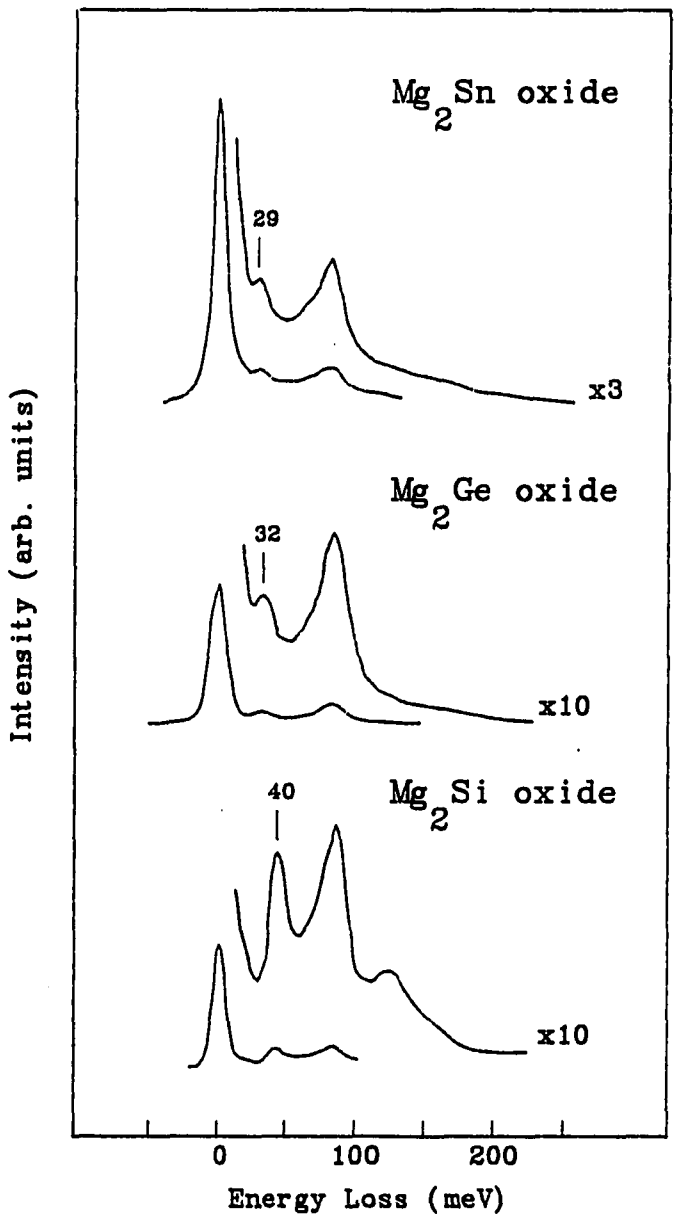

Fig. 4.27 HREELS of native oxides of Mg_2Sn, Mg_2Ge, and Mg_2Si

in magnitude, the surface phonon frequencies are very close to the longitudinal optical mode frequencies.

The peak at 80 meV is assigned to the Mg-O vibrational mode. This assignment is based on the fact that this peak is common to all three compounds. Also, a previous study[60] of MgO single crystals showed a surface optical phonon at 80.6 meV. A Si-O mode occurs at 125 meV on the Mg_2Si surface. This is confirmed by oxygen adsorption experiments on the clean surface. The Ge-O mode on Mg_2Ge is unresolved from the Mg-O mode, but oxygen adsorption experiments on Ge would seem to indicate that it would be near 100 meV. The shoulder at 75 meV that occurs only on the Mg_2Sn oxide is assigned to the Sn-O mode.

The HREEL spectra of the Mg_2Si oxide for different primary energies is shown in Fig. 4.28. The increase in intensity of the 80 and 125 meV peaks with decreasing primary energy is consistent with the identification of these as oxide modes. The surface phonon which occurs at the oxide-crystal interface is more sensitive to higher primary energies. This is due to the fact that the probing depth of the electron increases with increasing primary energy. The oxide layer is a smaller fraction of the probed volume for higher primary energies.

Figure 4.29a shows the HREEL spectrum of the native oxide of Mg_2Si. This surface can be cleaned by 1kV Ar(+) sputter-etching. The HREEL spectrum of this surface is shown in Fig. 4.29b. A high background and a poor resolution for the disordered surface result in only a shoulder for the surface phonon mode. Annealing of the surface to 600°C brings order back to the surface and a well-resolved surface phonon peak is

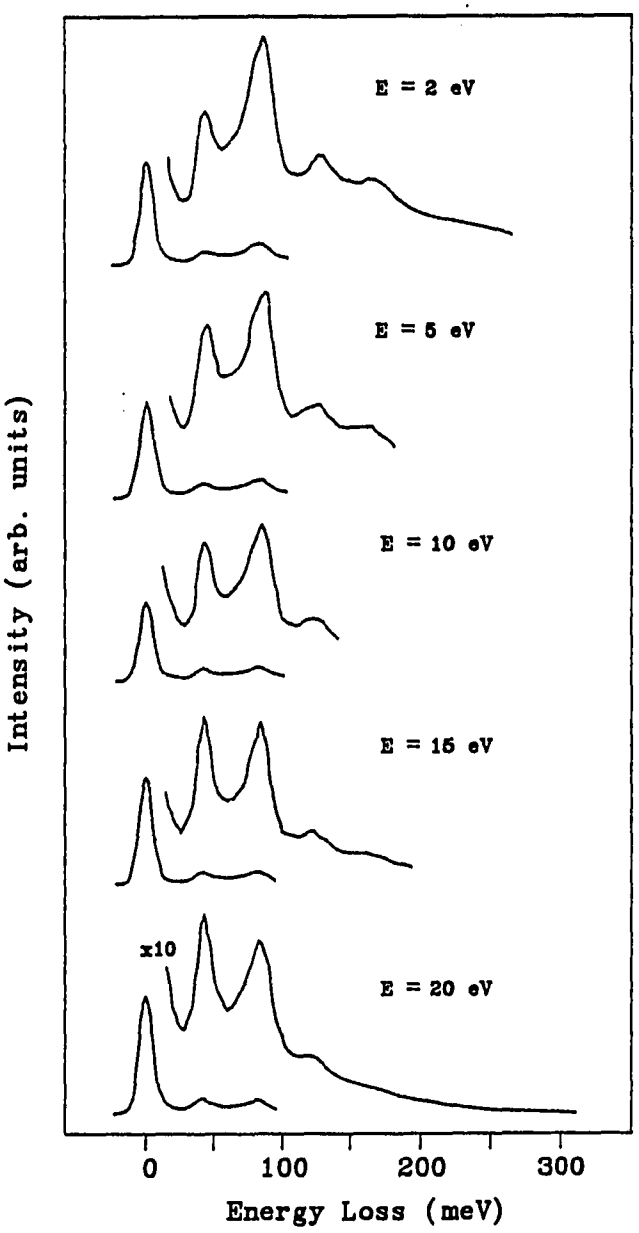

Fig. 4.28 HREELS of native oxide of Mg_2Si at varying incident energies

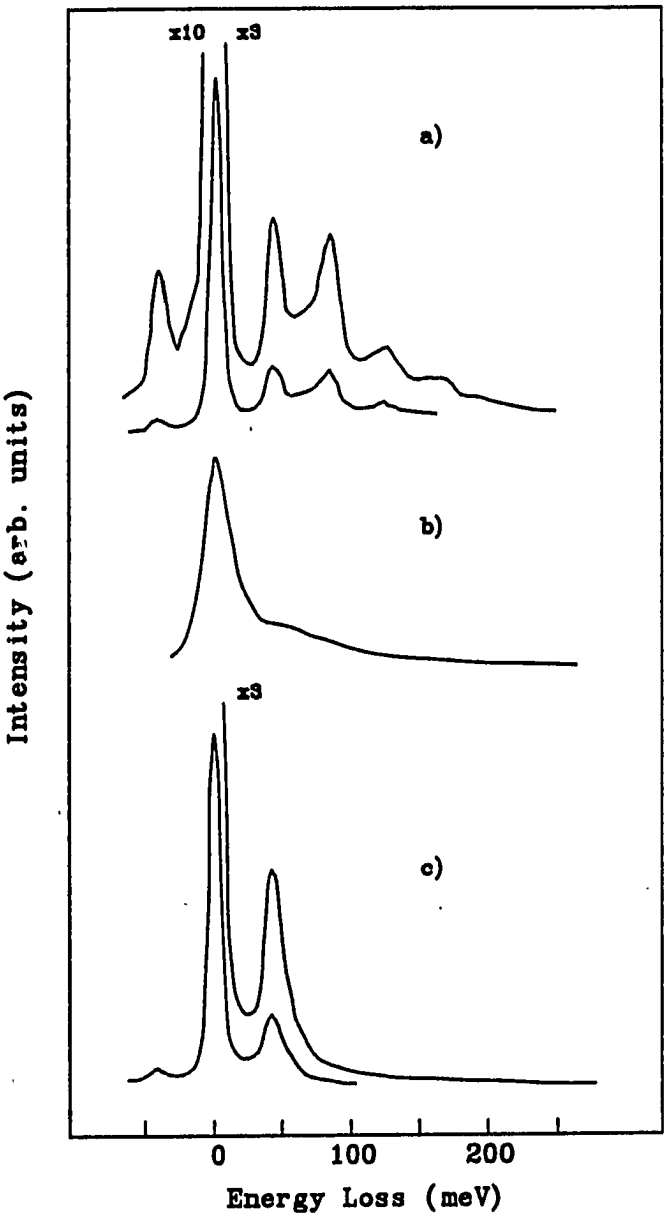

Fig. 4.29 HREELS of Mg_2Si: (a) native oxide; (b) after sputter-etching; (c) after subsequent annealing

observed (Fig. 4.29c). Also visible is an anti-Stokes energy gain peak on the left side of the elastic peak. The ratio of intensities of the Stokes and anti-Stokes peaks agree closely with the Bose distribution $e^{-\hbar\omega/kT}$. A multiple loss is also visible at 80 meV on an expanded scale. No noticeable shift is seen in the 40 meV surface phonon peak when going from the native oxide to the clean surface. This would indicate that screening by the oxide layer is negligible.

Using the expression for the scattering probability Γ (eq. 2.12) we can calculate the theoretical value of the of the ratio of the scattered intensity to the elastic intensity. This can then be compared to the experimental value. The scattering probability integrated over solid angle is given by

$$\Gamma = \frac{I_{inelas}}{I_{elas}} = \left\{\frac{\exp(\hbar\omega_s/kT)}{\exp(\hbar\omega_s/kT)-1}\right\}\cdot\left\{\frac{\pi e^2}{\hbar v\cos(\theta)}\right\}\cdot\left\{\frac{\varepsilon_o - 1}{\varepsilon_o + 1} - \frac{\varepsilon_\infty - 1}{\varepsilon_\infty + 1}\right\}.$$

The theoretical value is calculated to be Γ=0.18 while the experimental value $I_{inelastic}/I_{elastic}$ is measured to be 0.15, giving fairly good agreement between theory and experiment.

V. SUMMARY

In this work, vibrational and electronic EELS, as well as Auger electron spectroscopy, were used to study the interaction of O_2, H, NO, N, and N_2O with Ge(111) and disordered surfaces at room temperature. Activated NO, N_2O, and N_2 were also used. These studies were used to elucidate the effect of surface order on the adsorption process, to compare chemisorption of oxygen originating from different oxygen containing molecules, and to study nitrogen bonding. High resolution EELS studies of the narrow-gap semiconducting compounds Mg_2Sn, Mg_2Ge, and Mg_2Si were also done.

It is found that molecular hydrogen (H_2) does not react with the Ge surfaces at room temperature. Atomic hydrogen (H), however, does react with the surface, with the characteristic peaks being the Ge-H wagging mode at 70 meV and the Ge-H stretch mode at 247 meV. The HREELS results also indicate preferential sputtering of Ge-bonded hydrogen from films of a-$Ge_{1-x}C_x$:H. This is supported by Auger line shape measurements which show a change in the shape of the Ge(MVV) transition following exposure to atomic hydrogen. A dissociation energy for hydrogen on Ge of 2.9 eV was obtained by fitting the energy of the G-H stretch overtone to a Morse potential.

Contrary to the results for molecular hydrogen, molecular oxygen (O_2) is observed to react with the Ge surfaces at room temperature. Results indicate that O_2 dissociates and bonds at the Ge(111) surface in the bridged configuration. Three peaks characteristic of this

adsorption were observed. The oxidation state increases from +1 to +3 with increasing exposure at Ge(111). The +3 oxidation state indicates oxygen bonding to surface and subsurface Ge atoms. Exposure of the pre-oxidized Ge(111) surface to hydrogen atoms results in a shift of the Ge-H vibrational stretch mode. The shift indicates the presence of the +3 oxidation state at high exposures.

Mainly the +1 oxidation state is observed at the disordered surfaces. This may be due to a high density of surface dangling bonds and deeper penetration of oxygen which result in a dilute Ge-O-Ge (+1 oxidation state) bonding configuration even at higher exposures. Exposure of the pre-oxidized a-Ge surface to hydrogen indicates the presence of a high density of isolated Ge-H bonds (i.e., no near-neighbor oxygen) and the H-Ge-O-Ge bonding configuration.

The NO molecules dissociate at Ge(111) and the disordered surfaces, and N and O atoms bond primarily at the top surface layer. The oxygen is bonded in a bridge configuration, resulting in the +1 oxidation state only. Exposure of Ge(111) to 10^4L NO and then to oxygen indicates that chemisorbed N and O atoms prevent oxygen penetration. The nitrogen related loss peaks in the vibrational and electronic EELS are not resolved from the oxygen related losses. Upon heating the NO-exposed surfaces oxygen is desorbed and the nitrogen related losses in the HREELS are identified and attributed to the nitride bond.

The reactivity of Ge surfaces toward N_2O is very low. The N_2O molecules decompose at the surface to chemisorbed oxygen atoms and to desorbing N_2. The oxidation state is +1 up to an exposure of 10^5L N_2O.

The relatively higher reactivity of the disordered surfaces may indicate N_2O decomposition at dangling bonds and surface defects.

Unactivated molecular nitrogen (N_2) is observed to be non-reactive with the Ge surfaces. Exposing the surface to nitrogen atoms and ions, however, enables the identification of the room temperature precursor Ge nitride state by HREELS. This state transfers into the nitride bond upon heating the surface to ~550°C. When the surfaces are exposed to activated NO, N_2O, and N_2, nitrogen and oxygen are detected in greater quantities. Nitrogen related losses are then identified in the electronic EELS. The decrease in the intensity of various loss peaks with increasing coverage indicates that bonding occurs primarily at the top surface layer at both surfaces. This is similar to bonding of atomic oxygen (N_2O) to the top surface layer of Si(100) and bonding of oxygen originating from O_2 to surface and subsurface atoms.[28]

Surface phonon modes of the narrow-gap semiconducting compounds Mg_2Sn, Mg_2Ge and Mg_2Si were detected at 29, 32, and 40 meV, respectively. The native oxide of all three show a dominant Mg-O mode at 80 meV. Probable Sn-O, Ge-O, and Si-O modes are also identified. Complete removal of the oxide layer was accomplished only on the Mg_2Si surface but resulted in no noticeable change in the energy of the surface phonon. Results are compared to the known bulk optical properties of these compounds.

VI. BIBLIOGRAPHY

1. H. Ibach and D. Mills, Electron Energy Loss Spectroscopy and Surface Vibrations (Academic Press, New York, 1982).
2. L. C. Feldman and J. W. Mayer, Fundamentals of Surface and Thin Film Analysis (North-Holland, New York, 1986), p. 270.
3. F. M. Prost and T. C. Piper, J. Vac. Sci. Technol. 4, 53 (1967).
4. H. Ibach, Phys. Rev. Lett. 24, 1416 (1970).
5. R. Fuchs and K. L. Kliewer, Phys. Rev. 140, A2076 (1965).
6. P. A. Thiry, J. Electron Spectrosc. 30, 261 (1983).
7. P. A. Thiry, J. Electron Spectrosc. 39, 273 (1986).
8. L. Papagno, X. Y. Shen, J. Anderson, G. Schirripa Spagnolo, and G. J. Lapeyre, Phys. Rev. B 34, 7188 (1986).
9. L. Papagno, L. S. Caputi, D. Frankel, Y. Chen, and G. J. Lapeyre, Surface Sci. 189/190, 199 (1987); L. Papagano, L. S. Caputi, J. Anderson, and G. J. Lapeyre, Phys. Rev. B 40, 8443 (1989).
10. J. Q. Broughton, J. A. Schaefer, J. C. Bean, and H. H. Farrell, Phys Rev. B 33, 6841 (1986).
11. J. Shinar, R. Shinar, S. Mitra, and J.-Y. Kim, Phys. Rev. Lett. 62, 2001 (1989).
12. J. S. Park, R. P. G. Karunasiri, K. L. Wang, S. S. Rhee, and C. H. Chern, Appl. Phys. Lett. 54, 1564 (1989), and references therein.
13. H. C. Liu, D. Landheer, M. Buchanan, and D. C. Houghton, Appl. Phys. Lett. 52, 1809 (1988).
14. L. Kameswara Rao, K. Solomon Harshavardhan, A. Selvarajan, and M. S.

Hedge, Appl. Phys. Lett. 49, 826 (1986).

15. O. J. Gregory and E. E. Crisman in Integrated Circuits: Chemical and Physical Processing of Integrated Circuits (Am. Chem. Soc., Washington, D.C., 1985).

16. C. Kittel, Introduction to Solid State Physics, 5th ed. (Wiley, New York, 1976), p. 349.

17. L. D. Landau, E. M. Lifshitz, and L. P. Pitaevskii, Electrodynamics of Continuous Media, 2nd ed. (Pergamon, New York, 1984), 37.

18. H. Lüth, in Festkörperprobleme XXI (Vieweg, Braunschweig, 1981).

19. E. A. Stern and R. A. Ferrel, Phys. Rev. 120, 130 (1960).

20. E. Evans and D. L. Mills, Phys. Rev. B 5, 4126 (1972).

21. H. B. Rosenstock, Phys. Rev. B 9, 1963, (1974).

22. O. Klemperer, Electron Optics (Cambridge Univ. Press, London, 1971).

23. H. Ibach, H. D. Bruchmann, and H. Wagner, Appl. Phys. A 29,113 (1982).

24. J. A. Schaefer and W. Gopel, Surface Sci. 155, 535 (1985).

25. M. Nishijima, K. Edamoto, Y. Kubota, H. Kobayashi, and M. Onchi, Surface Sci. 158, 422 (1985).

26. Z. Ying and W. Ho, J. Vac. Sci. Technol. A 7, 2099 (1989).

27. D. Schmeisser, R. D. Schnell, A. Bogen, F. J. Himpsel, D. Rieger, G. Landgren, and J. F. Morar, Surface Sci. 172, 455 (1988).

28. H. J. Kuhr and W. Ranke, Surface Sci. 201, 408 (1988).

29. H. J. W Zandvliet, E. G. Keim, and A. van Silfhout, J. Vac. Sci. Technol. A (to be published).

30. L. Surnev and M. Tikhov, Surface Sci. 123, 505 (1982).

31. R. Shinar, A. G. Entringer, J. Shinar, H.-S. Wu, and H. R. Shanks, J. Vac. Sci. Technol. A 7, 2998 (1989), and references therein; A. G. Entringer, R. Shinar, and H. R. Shanks, Surface Sci. (to be published).

32. J. A. Schaefer, J. Q. Broughton, J. C. Bean, and H. H. Farrell, J. Electron Spectrosc. 39, 127 (1986).

33. H. J. W. Zandvliet and A. Van Silfhout, Surface Sci. 195, 138 (1988), and references therein.

34. R. S. Becker, B. S. Schwartzentruber, J. S. Vickers, and T. Klistner, Phys. Rev. B 39, 1633 (1989); G. M. Guichar, G. A. Garry, and C. A. Sebenne, Surface Sci. 85, 326 (1979).

35. J. Shinar, H.-S. Wu, R. Shinar, and H. S. Shanks, J. Appl. Phys. 62, 808 (1987).

36. R. Shinar, J. Vac. Sci. Technol. A 6, 2910 (1988), and references therein.

37. L. E. Davis, N. C. MacDonald, P. W. Palmberg, G. E. Riach, and R. E. Weber, Handbook of Auger Electron Spectroscopy, 2nd ed. (Perkin Elmer Corp., Eden Praire, MN, 1976).

38. O. Millo, A. Many, and Y. Goldstein, J. Vac. Sci. Technol. A 7, 2688 (1989), and references therein.

39. A. G. B. M. Sasse, D. G. Lakerveld, and A. Van Silfhout, Surface Sci. 195, L167 (1988).

40. R. Shinar, J. Shinar, H.-S. Wu, and H. R. Shanks, J. Vac. Sci. Technol. A 5, 2804 (1987).

41. G. Lucovsky, S. S. Chao, J. Yang, J. E. Tyler, R. C. Ross, and W.

Czubatyj, Phys. Rev. B 31, 2190 (1985).

42. G. Lucovsky, J. Yang, J. S. Chao, J. E. Tyler, and W. Czubatyj, Phys. Rev. B, 28 3225 (1983).

43. M. Cardona, Phys. Status Solidi B 118, 463 (1983).

44. H. R. Shanks, F. R. Jeffrey, and M. E. Lowry, J. Phys. (Paris) 42, C4-773 (1981).

45. H. Wagner, R. Butz, U. Backes, and D. Bruchmann, Solid State Commun. 38, 1155 (1981).

46. H. Shanks, C. J. Fang, L. Ley, M. Cardona, F. J. Demond, and S. Valbitzer, Phys. Status Solidi B 100, 43 (1980).

47. F. L. Galeener and G. Lucovsky, Phys. Rev. Lett. 37, 1474 (1976).

48. R. J. Bell, P. Dean, and D. C. Hibbins-Butler, J. Phys. C: Solid State Phys. 4, 1214 (1971).

49. A. L. Shabalov and M. S. Feldman, Phys. Status Solidi A 83, K11 (1984).

50. L. Surnev, Surface Sci. 110, 439 (1981).

51. R. Ludeke and L. Esaki, Phys. Rev. Lett. 33, 653, (1974).

52. L. Surnev and M. Tikhov, Surface Sci. 138, 40 (1984).

53. H. Froitzheim and U. Kohler, Phys. Rev. B 40, 8213 (1989).

54. Yu. I. Ukhanov, Yu. N. Volgin, and F. F. Grekov, in Fiz. Elektron., Nauchn. Dokl., Gertsenovskie Chteniya, 27th, edited by I.M. Bronshtein (Gos. Pedegog. Inst., Leningrad, 1974), vol. III, p. 45.

55. Yu. N. Volgin and Yu. I. Ukhanov, Opt. Spectrosc. 38, 412 (1975).

56. K. Edamoto, S. Tanaka, M. Onchi, and M. Nishijima, Surface Sci. 167,

285 (1986).

57. E.G. Keim, L. Wolterbeek, and A. Van Silfhout, Surface Sci. 180, 565 (1987).

58. D. McWilliams and D. Lynch, Phys. Rev. 130, 2248 (1963).

59. C.J. Buchenauer and M. Cardona, Phys. Rev. B 3, 2504 (1971).

60. P. A. Cox and A. A. Williams, J. Electron Spectrosc. 39, 45 (1986).

61. E. Merzbacher, Quantum Mechanics (Wiley, New York, 1970), p. 362.

62. G. D. Mahan, in Elementary Excitations in Solids, Molecules, and Atoms (Plenum, London, 1974), p. 93.

63. G. D. Mahan, Phys. Rev. B 5, 739 (1972).

VII. ACKNOWLEDGEMENTS

Most of all, I would like to thank Ruth Shinar whose advice and guidance made this dissertation possible. Our many discussions and days working together in the lab made for a truly enjoyable learning experience.

A special thanks goes to Howard Shanks for general support and encouragement. Thanks also goes to the staff of the Microelectronics Research Center, especially fellow Loras graduate Kevin McCarron, whose expertise in the lab saved me on many occasions.

The assistance of several people is gratefully acknowledged: Joe Shinar, Howard Shanks, and Terry Holesinger for the samples they provided me, Steve Braymen for assisting me in the sample preparation, and the secretaries, Kerri Eggers and Evelyn Kruse for their patience in letting me use their printers. I would also like to thank the Dugan's crowd, for helping me get through the week.

I would also like to acknowledge the Air Force Office of Scientific Research, which provided the funding for this work.

Finally, I would like to thank my family and friends who supported me through some rough times. Their support and encouragement will always be remembered.

VIII. APPENDIX A:

DERIVATION OF THE SCATTERING PROBABILITY

In order to achieve an understanding of the physics behind the scattering mechanism, the scattering probability for surface phonons will be derived. First, a very general derivation of the distribution of scattered states will be given. This is based on material from Merzbacher.[61] This will lead to the Poisson distribution. Second, the actual scattering probability will be derived. This is based on a derivation given by Mahan.[62]

The effect of the incident electron on an oscillator at the surface can be understood in terms of an external time dependent force F(t) that is independent of the oscillator displacement q. The Hamiltonian for such a system then has the form

$$H = \frac{p^2}{2\mu} + \frac{1}{2}\mu\omega^2 q^2 - qF(t). \tag{A.1}$$

This can be written in terms of the usual creation and annihilation operators of the harmonic oscillator as

$$H = \hbar\omega(a^{\dagger}a + \tfrac{1}{2}) + f(t)(a + a^{\dagger}), \tag{A.2}$$

where

$$f(t) = -\left(\frac{\hbar}{2\mu\omega}\right)^{\frac{1}{2}} \cdot F(t). \tag{A.3}$$

The equation of motion for the operator a is given by the Heisenberg

equation

$$i\hbar\frac{da(t)}{dt} = [a(t),H(t)] = \hbar\omega a(t) + f(t) \qquad (A.4)$$

or

$$\frac{da(t)}{dt} + i\omega a(t) = -\frac{i}{\hbar}f(t). \qquad (A.5)$$

The force f(t) is nonzero only during a finite time interval $t_1<t<t_2$ when the electron is near the surface. We note that before and after the interaction with the electron the system is described by the harmonic oscillator states $|n\rangle_b$ and $|n\rangle_a$ respectively (b for before and a for after), which are eigenstates of the "free" harmonic oscillator Hamiltonians

$$H_b = \hbar\omega(a_b^\dagger a_b + \tfrac{1}{2}) \qquad \text{for} \qquad t<t_1, \qquad (A.7)$$

$$H_a = \hbar\omega(a_a^\dagger a_a + \tfrac{1}{2}) \qquad \text{for} \qquad t>t_2. \qquad (A.8)$$

The operators $a_b(t)$ and $a_a(t)$ are solutions of the homogeneous equation

$$\frac{da(t)}{dt} + i\omega a(t) = 0 \qquad (A.9)$$

for $t<t_1$ and $t>t_2$ respectively.

A particular solution to the inhomogeneous equation can be written as

$$a(t) = -\frac{i}{\hbar}\int_{-\infty}^{+\infty} G(t - t')f(t')dt', \qquad (A.10)$$

where the Green's function $G(t - t')$ is the impulse response of the system:

$$\frac{dG(t - t')}{dt} + i\omega G(t - t') = \delta(t - t'). \tag{A.11}$$

For $t \neq t'$ the Green's function is proportional to $e^{-i\omega(t-t')}$, but at $t=t'$ there is a discontinuity of the order of a step function $\eta(t)$. Two Green's functions which satisfy these conditions are

$$G_R(t - t') = \eta(t - t')e^{-i\omega(t-t')} \tag{A.12}$$

and

$$G_A(t - t') = -\eta(t' - t)e^{-i\omega(t-t')}, \tag{A.13}$$

where G_R is the retarded Green's function and G_A is the advanced Green's function. The retarded Green's function coincides with the complementary solution to the homogeneous equation $a_b(t)$, and the advanced Green's function coincides with the solution $a_a(t)$. Plugging in the Green's functions to (A.9) and combining the complementary and particular solutions, we get the following final solutions:

$$a(t) = a_b(t) - \frac{i}{\hbar}\int_{-\infty}^{t} e^{-i\omega(t-t')}f(t')dt' \tag{A.15}$$

and

$$a(t) = a_a(t) + \frac{i}{\hbar}\int_{t}^{+\infty} e^{-i\omega(t-t')}f(t')dt'. \tag{A.16}$$

Equating the two equivalent solutions gives a relation between $a_b(t)$ and

$a_a(t)$:

$$a_a(t) = a_b(t) - \frac{i}{\hbar}\int_{-\infty}^{+\infty} e^{-i\omega(t-t')} f(t')dt' \qquad (A.17)$$

The solutions to the homogeneous equation have the normal time dependence

$$a_b(t) = a_b e^{-i\omega t} \qquad \text{and} \qquad a_a(t) = a_a e^{-i\omega t}. \qquad (A.18)$$

Plugging these into (A.16) we get

$$a_a = a_b + \Gamma(\omega), \qquad (A.19)$$

where

$$\Gamma(\omega) = -\frac{i}{\hbar}\int_{-\infty}^{+\infty} e^{-i\omega t'} f(t')dt'. \qquad (A.20)$$

The function $\Gamma(\omega)$ is essentially the Fourier transform of the force $f(t)$.

We wish to find the probability of finding the system at $t>t_2$ in the nth eigenstate of H_a, if the system was in the ground state $|0\rangle_b$ of H_b at $t<t_1$. This is given by

$$P_n = |{}_a\langle n|0\rangle_b|^2. \qquad (A.21)$$

In order to do this we must find a unitary operator relating the two sets of states. This unitary operator will satisfy the relations

$$a_a = S^{\dagger} a_b S \qquad (A.22)$$

and

$$|n\rangle_a = S^\dagger |n\rangle_b. \tag{A.23}$$

As a direct consequence of the commutation relations between a and $a^\dagger$, $[a,a^\dagger]=1$, and using the well known operator identity

$$e^A B e^{-A} = B + [A,B] + (1/2!)[A,[A,B]] + \cdots, \tag{A.24}$$

the following relation is seen to hold true:

$$\exp(\alpha a - \alpha a^\dagger)\cdot a \cdot \exp(-\alpha a + \alpha a^\dagger) = a + \alpha. \tag{A.25}$$

Letting $\alpha=\Gamma(\omega)$ and comparing equations (A.19), (A.22), and (A.25) we find that the the transformation we are seeking has the form:

$$S = \exp[\Gamma(\omega)a - \Gamma(\omega)a^\dagger)]. \tag{A.26}$$

The amplitude ${}_a\langle n|0\rangle_b = {}_b\langle n|S|0\rangle_b$ for transition from the ground state of H_b to the nth eigenstate of H_a then takes the form

$${}_b\langle n|e^{[\Gamma(\omega)a^\dagger - \Gamma(\omega)a]}|0\rangle_b. \tag{A.27}$$

In order to solve this we make use of the identity

$$e^{A+B} = e^A e^B e^{-\frac{1}{2}[A,B]}, \tag{A.28}$$

which holds for any operators A and B that commute with their commutator. The amplitude then becomes

$${}_a\langle n|0\rangle_b = {}_b\langle n|e^{\Gamma(\omega)a^\dagger}\cdot e^{-\Gamma(\omega)a}\cdot e^{-\frac{1}{2}[\Gamma(\omega)]^2}|0\rangle_b \tag{A.29}$$

$$= e^{-\frac{1}{2}[\Gamma(\omega)]^2} \cdot {}_b\langle n|e^{\Gamma(\omega)a^\dagger}|0\rangle_b \tag{A.30}$$

$$= e^{-\frac{1}{2}[\Gamma(\omega)]^2} \cdot {}_b\langle n|\{1 + \Gamma(\omega)a^\dagger + (1/2!)[\Gamma(\omega)a^\dagger]^2 + \cdots\}|0\rangle_b \tag{A.31}$$

$$= e^{-\frac{1}{2}[\Gamma(\omega)]^2}(n!)^{-\frac{1}{2}}[\Gamma(\omega)]^n. \tag{A.32}$$

Here we have made use of the fact that $a|0\rangle=0$, the property of the creation operator $(a^\dagger)^n|0\rangle=(n!)^{\frac{1}{2}}|n\rangle$, and the orthonormality property of the harmonic oscillator eigenstates. The probability for transition from the ground state to the nth excited state is given by the square of the amplitude:

$$P_n(\omega) = |{}_a\langle n|0\rangle_b|^2 = e^{-[\Gamma(\omega)]^2} \cdot \frac{|\Gamma(\omega)|^{2n}}{n!} . \tag{A.33}$$

This is the Poisson distribution. We define the quantity $Q=\Gamma^2$ as the average number of modes that are excited. Note that Q is the ratio of the 1st order loss (P_1) to the 0th order loss (elastic peak).

In order to get the form of the scattering probability Q we cast the Hamiltonian into a different form:

$$H = H_{oe} + H_{os} + H_I \tag{A.34}$$

where H_{oe} is the energy of the electrons, H_{os} is the energy of the surface modes, and H_I is the energy of interaction between the two. The energy of the surface modes H_{os} has the form

$$H_{os} = \hbar\omega_s \sum_k (a_k^\dagger a_k + \tfrac{1}{2}) \tag{A.35}$$

Here we allow for different k values. The interaction term has the form:

$$H_I = \sum_k (\Gamma_k e^{i\mathbf{k}\cdot\boldsymbol{\rho}_e - k|z|}(a_k + a_k^\dagger)) \tag{A.36}$$

Note the similarities to (A.2). This form of the interaction term also has the linear combination of the operators a and $a^\dagger$. Again we have allowed for a k dependence. The spatial dependence is demanded by Laplace's equation (see Chapter 2), and the constant Γ_k is called the coupling constant.

First we must find the form of the coupling constant Γ_k. To do this we place the electron at rest some distance z above the surface. The first term, H_{oe} is zero and we have

$$H = \sum_k [\hbar\omega_s a_k^\dagger a_k + \Gamma_k e^{i\mathbf{k}\cdot\boldsymbol{\rho}_e - k|z|}(a_k + a_k^\dagger)] \tag{A.37}$$

Here we have dropped the constant ½ term in H_{os} for simplicity. This Hamiltonian may be diagonalized by completing the square:

$$H = \sum_k (\hbar\omega_s \tilde{a}_k^\dagger \tilde{a}_k - \frac{\Gamma_k^2}{\hbar\omega_s} e^{-2k|z|}), \tag{A.38}$$

$$\tilde{a}_k = a_k + \frac{\Gamma_k}{\hbar\omega_s} e^{-i\mathbf{k}\cdot\boldsymbol{\rho}_e - k|z|}. \tag{A.39}$$

The last term gives the image potential self-energy of the electron:

$$-\sum_k \frac{\Gamma_k^2}{\hbar\omega_s} e^{-2k|z|} = \frac{A}{(2\pi)^2}\cdot\int d^2k \frac{\Gamma_k^2}{\hbar\omega_s} e^{-2k|z|} = \frac{A}{(2\pi)^2}\cdot\int_0^\infty 2\pi k dk \frac{\Gamma_k^2}{\hbar\omega_s} e^{-2k|z|}. \quad (A.40)$$

Here the term $A/(2\pi)^2$ gives the density of levels per unit area k-space, where A is the normalization area. The image potential for an insulator has two contributions, the contribution from surface optical phonons and the contribution from high frequency electronic excitations.[62] The total static image potential has the form[63]

$$V_{total} = -\frac{e^2}{4z}\frac{\varepsilon_o - 1}{\varepsilon_o + 1}. \quad (A.41)$$

The contribution from high frequency electronic excitations has the form

$$V_{electronic} = -\frac{e^2}{4z}\frac{\varepsilon_\infty - 1}{\varepsilon_\infty + 1}. \quad (A.42)$$

Since the total potential is the sum of the electronic and surface phonon potentials, the contribution from the surface optical phonons is given by

$$V_{SO\ phonons} = \frac{e^2}{4z}\left(\frac{\varepsilon_o - 1}{\varepsilon_o + 1} - \frac{\varepsilon_\infty - 1}{\varepsilon_\infty + 1}\right). \quad (A.43)$$

We set this term equal to the expression for the self-energy given above and solve for Γ_k.

$$\frac{A}{(2\pi)^2}\cdot\int_0^\infty 2\pi k dk \frac{\Gamma_k^2}{\hbar\omega_s} e^{-2k|z|} = \frac{e^2}{4z}\left(\frac{\varepsilon_o - 1}{\varepsilon_o + 1} - \frac{\varepsilon_\infty - 1}{\varepsilon_\infty + 1}\right). \tag{A.44}$$

Noting that

$$\int_0^\infty dx e^{-ax} = \frac{1}{a}, \tag{A.45}$$

we can see that the coupling constant Γ_k has the form

$$\Gamma_k^2 = \frac{\pi e^2 \hbar\omega_s}{Ak}\left(\frac{\varepsilon_o - 1}{\varepsilon_o + 1} - \frac{\varepsilon_\infty - 1}{\varepsilon_\infty + 1}\right). \tag{A.46}$$

Now, instead of fixing the z position in space, we let the particle move in the z direction towards the surface, $z(t)=vt$, with $z(t=-\infty)=-\infty$. The equation we need to solve then has the form:

$$i\hbar\frac{\partial}{\partial t}\Psi(t) = H_I(t)\Psi(t) \tag{A.47}$$

$$= \sum_k \Gamma_k e^{k|z(t)|}(a_k \exp(i\omega_s t) + a_k^\dagger \exp(-i\omega_s t))\Psi(t). \tag{A.48}$$

Integrating, we find that

$$\Psi(t) = \exp[-i\sum_k (I_k(t)a_k + I_k^*(t)a_k^\dagger]\Psi(-\infty), \tag{A.49}$$

$$I_k(t) = \Gamma_k \cdot \int_{-\infty}^t dt' \exp(kvt')\exp(i\omega_s t') = \frac{\Gamma_k \exp(vkt + i\omega_s t)}{\hbar(vk + i\omega_s)}. \tag{A.50}$$

$\Psi(t)$ may be rewritten using (2.37) as

$$\Psi(t) = \prod_k \exp(-\tfrac{1}{2}|I_k(t)|^2)\exp(-iI_k{}^* a_k{}^\dagger)\exp(-iI_k a_k)\Psi(-\infty) \qquad (A.51)$$

$$= \prod_k \exp[(-\tfrac{1}{2})|I_k(t)|^2)\exp(-I_k{}^* a_k{}^\dagger)|0\rangle, \qquad (A.52)$$

where we have used the fact that $a_k|0\rangle=0$. The average number of surface modes for a given z value is then given by

$$N(z) = \sum_k \langle\Psi|a_k{}^\dagger a_k|\Psi\rangle = \sum_k |I_k(t)|^2 = \frac{A}{(2\pi)^2}\cdot\int d^2k\,|I_k(t)|^2 \qquad (A.53)$$

$$= \frac{A}{(2\pi)^2}\cdot\int_0^\infty 2\pi k dk \Gamma_k{}^2 \frac{e^{2kz(t)}}{\hbar^2(\omega_s{}^2 + v^2k^2)} \qquad (A.54)$$

$$= \frac{A}{(2\pi)^2}\cdot\int_0^\infty 2\pi k dk\cdot\frac{\pi e^2\hbar\omega_s}{Ak}\left(\frac{\varepsilon_o - 1}{\varepsilon_o + 1} - \frac{\varepsilon_\infty - 1}{\varepsilon_\infty + 1}\right)\cdot\frac{e^{2kz(t)}}{(\omega_s{}^2 + v^2k^2)}. \qquad (A.55)$$

We now make the substitutions $u=vk/\omega_s$ and $x=-2z\omega_s/v$.

$$N(-2z\omega_s/v) = \frac{e^2}{2\hbar v}\cdot\left(\frac{\varepsilon_o - 1}{\varepsilon_o + 1} - \frac{\varepsilon_\infty - 1}{\varepsilon_\infty + 1}\right)\cdot\int_0^\infty \frac{du e^{-ux}}{(1 + u^2)}. \qquad (A.56)$$

The integral is solveable numerically. Of particular importance is its value of $\pi/2$ at $z=u=0$. This will enable us to calculate the number of surface modes excited by a charge starting at $x=-\infty$ and ending up at $z=0$. The total number of modes for a particle going from infinity to the surface and back to infinity is twice this number. We then get for the

scattering probability

$$\frac{\pi e^2}{2\hbar v}\cdot\left(\frac{\varepsilon_o - 1}{\varepsilon_o + 1} - \frac{\varepsilon_\infty - 1}{\varepsilon_\infty + 1}\right). \tag{A.57}$$

This scattering probability was derived assuming normal incidence at T=0. Correction factors to account for nonnormal incidence and finite temperature are $1/\cos\theta$ and $1+n_s(T)$, respectively, where $n_s(T)$ is the Bose factor. The $\cos\theta$ factor comes about because we want only the normal component of the velocity $v\cos\theta$ in the denominator. The $1+n_s(T)$ factor comes about because of the occupation of excited states at non-zero temperature. The so-called Stokes peak involves the creation of a phonon and subsequent energy loss by the electron. The anti-Stokes peak involves the annihilation of a phonon and subsequent energy gain by the electron. Both the creation and annihilation of phonons involve harmonic oscillator creation and annihilation operators whose matrix elements (connecting adjacent states) are proportional to $(n+1)^{1/2}$ and $(n)^{1/2}$, respectively. We thus have

$$I(n+1) \propto |\langle n+1|a_n|n\rangle|^2 \propto n + 1, \tag{A.58}$$

$$I(n-1) \propto |\langle n-1|a_n^\dagger|n\rangle|^2 \propto n. \tag{A.59}$$

If the system is in thermal equilibrium, then we have

$$I(n+1) \propto \langle n \rangle + 1 = \frac{\exp(\hbar\omega_s/kT)}{\exp(\hbar\omega_s/kT)-1}, \tag{A.60}$$

$$I(n-1) \propto \langle n \rangle = \frac{1}{\exp(\hbar\omega_s/kT)}. \tag{A.61}$$

The ratio of the anti-Stokes to Stokes peaks should then be $\exp(-\hbar\omega_s/kT)$ as is observed. The expression for the scattering probability for energy loss then becomes

$$Q = \frac{\pi e^2}{2\hbar v\cos\theta} \cdot \frac{\exp(\hbar\omega_s/kT)}{\exp(\hbar\omega_s/kT)-1} \cdot \left(\frac{\varepsilon_o - 1}{\varepsilon_o + 1} - \frac{\varepsilon_\infty - 1}{\varepsilon_\infty + 1} \right). \tag{A.62}$$

This is the expression obtained by Ibach and Mills using a slightly different approach.[1]

This expression holds for the so-called Fuchs-Kleiwer surface modes on semi-insulating infrared-active compounds. It is assumed that the angular distribution of the scattered electrons is small enough so that most all of the electrons are captured by the analyzer. This is usually true for single crystal surfaces in the dipole scattering regime.

IX. APPENDIX B:

TUNING THE HREEL SPECTROMETER

As mentioned before, tuning of the spectrometer demands patience and practice. Many local maxima exist in the phase space of tuneable parameters. The basic strategy of tuning the spectrometer is to start with a set of more or less proven initial conditions. One then maximizes the current at various places in the spectrometer by adjusting the voltages in a systematic way. This Appendix will expand on the theory of the 127° sector and its interaction with other parts of the spectrometer, set up the initial conditions, and then take one through the various stages of tuning the spectrometer.

A. Definition of Quantities

We first define the important parameters. For the manipular, the x- direction is defined as the horizontal direction perpendicular to the axis of the manipulator. The y-direction is defined as the vertical direction perpendicular to the axis of the manipulator, and the z-direction is the direction along the axis of the manipulator. The angle of rotation about the z-axis is defined by θ.

The front panel of the spectrometer is divided up into several sections. The first of these sections contains the controls for the electron gun. In the lists that follow, the first name labels the variable that you control, and the name in parentheses labels the

corresponding push-button on the consol used for measurement of that quantity. Note that some of the quantities are not measurable.

I_{fil}	Filament (current)
R	Repeller (repeller)
A_1	Anode 1 (main)
ΔA_1	Anode 1 asym (diff)
A_2	Anode 2 (main)
ΔA_2	Anode 2 asym (diff)
A_3	Anode 3 (main)
ΔA_3	Anode 3 asym (diff)
E_p	Primary Energy (prim energy)

All of these quantities except E_p make up the electron gun. Each anode has two plates. The quantities A1, A2, and A3 give an average value of the two plates and are measured with respect to the center potential of the cathode, which floats at a potential E_p/e below ground (target) potential. The asymmetries provide beam steering capabilities, and each is provided with a polarity switch.

The monochromator voltages are defined as follows:

C_m	Monochrom. contact potential
PE_m	Monochrom. pass energy
M	Monochrom. slit potential (slit)
r_{pm}	Voltage on inner plate of pre-monochrom.

R_{pm}	Voltage on outer plate of pre-monochrom.
r_{mm}	Voltage on inner plate of main monochrom.
R_{mm}	Voltage on outer plate of main monochrom.
Δ_{pm}	$R_{pm} - r_{pm}$ (diff)
Δ_{mm}	$R_{mm} - r_{mm}$ (diff)

The pot labeled C_m controls the contact potential between the cathode and the entrance slit to the pre-monochromator. The actual effective level of zero potential will not be at the center potential of the cathode, but instead will be slighly shifted, forming an effective contact potential $C_{m,eff}$. This is due to the fact that the electrons will be pulled out of a charge cloud near the cathode. This shift will depend on the cathode emission density, the repeller potential, and the slit potential M. The net effect of changing C_m is to simply change the monochromator slit potential M, measured with respect to the center potential of the cathode. Changing the monochromator pass energy PE_m, however, is set up to not only change the slit potential M, but also the deflection capacitor voltages in such a way as to maintain a linear relationship between M and the various deflection plates. The pass energy is proportional to the potential difference between the various pairs of plates. Combining equations (3.3) and (3.4) we see that the various quantities are related by the equation:

$$PE_m = \tfrac{1}{2}mv_o^2 = \frac{e\Delta_{pm}}{2\ln(R_{pm}/r_{pm})} = \frac{e\Delta_{mm}}{2\ln(R_{mm}/r_{mm})} = e(C_{m,eff} + M). \quad (B.1)$$

Since the resolution is proportional to the pass energy, this equation states that the resolution is proportional to the capacitor voltages.

The analyzer voltages are now defined:

C_a	Analyzer contact potential
PE_a	Analyzer pass energy
A	Analyzer slit potential (slit)
r_{ma}	Voltage on inner plate of main analyzer
R_{ma}	Voltage on outer plate of main analyzer
r_{sa}	Voltage on inner plate of secondary analyzer
R_{sa}	Voltage on outer plate of secondary analyzer
Δ_{ma}	$R_{ma} - r_{ma}$ (diff)
Δ_{sa}	$R_{sa} - r_{sa}$ (diff)

The quantities are similar to the corresponding monochromator voltages except that the analyzer contact potential is the contact potential between the target (ground) and the analyzer slit A. A similar relation holds for the various quantiies:

$$PE_a = \tfrac{1}{2}mv_o^2 = \frac{e\Delta_{ma}}{2\ln(R_{ma}/r_{ma})} = \frac{e\Delta_{sa}}{2\ln(R_{sa}/r_{sa})} = e(C_a + A) \qquad (B.2)$$

Very low pass energies (~0.5eV) are needed to obtain the desired high resolution. The electrons must then be accelerated towards the target when they leave the monochromator to get the desired impact

energies (~5-20 eV). The accleration optics that do this consist of two electrostatic lenses:

E_1	Electrode 1 (main)
ΔE_1	Electrode 1 asym (diff)
E_2	Electrode 2 (main)
ΔE_2	Electrode 2 asym. (diff)

Again each electrode is made up of two plates. The main voltages are again measured with respect to the cathode center potential. The asymmetries provide beam steering capabilities perpendicular to (E_1) and parallel to (E_2) the plane of scattering.

Once the electrons have scattered from the target, they must be decelerated to the pass energy of the analyzer. The deceleration optics also consists of two electrostatic lenses:

E_3	Electrode 3 (main)
E_4	Electrode 4 (main)
ΔE_4	Electrode 4 asym. (diff

Beam steering perpendicular to the plane of scattering is provided by ΔE_4. There is no asymmetry control for E_3.

Figure B.1 shows the relationship between the various voltages in the scattering process. An electron that has lost energy $\hbar\omega$ when scattering at the surface enters the analyzer with an energy given by

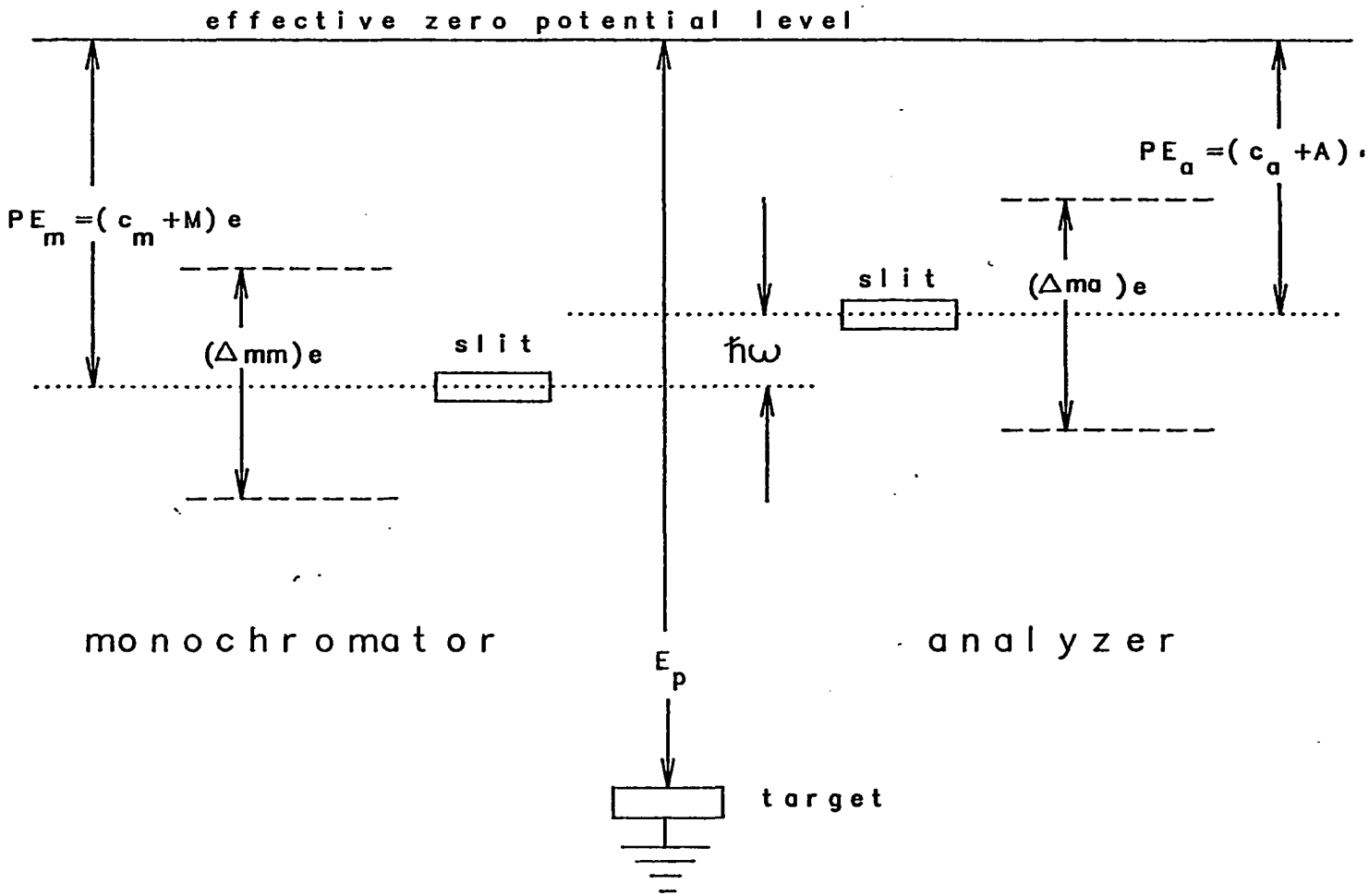

Fig. B.1 Voltage and potential relations between monochromator, target, and analyzer

$e(C_a + A) - \hbar\omega$. In order for these electrons to pass, A must compensate for $\hbar\omega$. Usually the elastically scattered electrons are collected at the same slit potential as the monochromator. In the spectrometer, the analyzer slit potential is then ramped across the range from near the elastic peak out to about 500 mV below the elastic peak. The corresponding deceleration optics and plate potentials are also ramped accordingly (while keeping the potential difference between the plates a constant). Maxima in the transmitted electron current will occur when $A - M = \hbar\omega$. These electrons are collected and multiplied by a channel electron multiplier located at the exit slit of the secondary analyzer.

B. Initial Setup

When tuning the instrument initially one should make sure that all of the cables are connected properly. Two cables provide the voltages to the spectrometer. Two MHV feedthroughs provide the connections to the "high" and "low" of the channeltron detector. Cables connected to these feedthroughs are fed into a decoupling box. High voltage is fed into this decoupling box, and the signal is sent out. The output is fed into a pre-amp and then to the ratemeter. The HREELS power supply should be plugged in, and the LED display at the top of the panel should be on. To measure a voltage, simply press the appropriate button below the corresponding control pot and hold it. The voltage will appear (to the nearest millivolt) on the LED display. The filament current will be displayed while the button below the small filament current control pot

is pressed.

C. Finding the Straight Through Beam

Step 1: Once the cables have been properly connected, the current in the hairpin filament can be turned on. If the system was recently up to air, the filament current should be slowly turned up from zero to 2A. This will give the filament a chance to outgass slowly, thereby increasing its life.

Step 2: With the filament current (I_{fil}) at 2A, set the following initial conditions:

E_p	5V
C_m	fully counterclockwise
M (slit)	set to about -0.200V using the PE_m control
Δ_{pm}	0.5V
R	-1V
A_1	1V
A_2	15V
A_3	-2V
Asym.	all set to zero

It is important that these settings be done in the order presented because of the interdependence of the controls.

Step 3: Take a picoammeter and connect it to the plug labeled R_{mm}

(from spectrometer) on the front panel. Set the picoammeter to its most sensitive current range. Now slowly turn up C_m until the picoammeter registers some current.

Step 4: Maximize the current in a cyclic way by adjusting R, A_1, A_2, A_3, C_m, and I_{fil}. After a few cycles adjust the associated asymmetries as well. Continue until a maximum is reached in the current. The current should be in the 10^{-8} range. Changing Δ_{pm} both ways should result in a reduction of the current. If it doesn't, change A_2 about 3V up or down and repeat the optimization process.

Step 5: Current will now be measured at the target location in the scattering chamber. Reconnect the main monochromator to the voltage supply, and put the sample holder in the center of the scattering chamber. Hook the electrometer to the feedthrough pin connected to the sample holder. Be sure to ground the shielding on the electrometer cable.

Step 6: Set E_1 to +1V and E_2 to +3V, and set their associated symmetries to zero. Set the electrometer to its most sensitive range. Slowly turn up Δ_{mm} until some current is registered on the picoammeter. Now optimize in a cyclic way adjusting I_{fil}, R, A_1, A_2, A_3, Δ_{mm}, E_1, E_2, and the associated asymmetries. The maximum current attainable should be in the 10^{-10} range.

Step 7: Remove the sample holder from the scattering chamber, and make sure that the spectrometer is in the straight through position. Set the slit potential A of the analyzer and E_4 to the same value of the monochromator slit M. Connect the picoammeter to the plug labeled R_{ma}

(from spectrometer), and slowly turn up E_3 until some current is registered on the picoammeter. Maximize the current by adjusting E_1, E_2, E_3, E_4, and their associated asymmetries, and then reconnect the main analyzer to the voltage supply.

Step 8: Set Δ_{ma} to exactly the same value as Δ_{mm}, and set the channeltron high voltage supply to 2.2kV. The ratemeter should be at its highest sensitivity. Slowly turn up Δ_{sa} from zero until some counts are registered on the ratemeter.

Important: Do not let the count rate exceed $3x10^4$ cps. Count rates greater than this will shorten the life of the channeltron. When maximizing the signal, keep the count rate below $3x10^4$ cps by lowering the filament current, I_{fil}.

Step 9: Note the optimum filament current. This will be needed later. Maximize the signal in a cyclic way by adjusting ΔE_1, E_1, ΔE_2, E_2, E_3, ΔE_4, E_4, A (using the motorpot), and Δ_{sa}. In the straight through position, count rates of about 10^4cps should be achievable with the filament current reduced to about 1.5A.

D. Finding the Reflected Beam

Step 10: Rotate the analyzer to the sample analysis position. This is done by making 11 turns of the linear motion feedthrough. Insert the sample into the scattering chamber. The sample should be vertical and facing towards the monochromator and analyzer. The sample

is in the right position when it can be viewed through the small slit in the scattering chamber. It is very important that the sample be grounded, either directly or through the picoammeter.

Step 11: Turn up the filament current to the optimal value noted in step 9. Set the ratemeter to its highest sensitivity. Now adjust the x setting of the manipulator until some counts are observed on the ratemeter. If this doesn't work try adjusting ΔE_4. Once some signal has been obtained, optimize in a cyclic way using all of the settings. Oxide and carbon contaminated samples should provide count rates of around 10^4 cps. Clean single crystal samples should give count rates in excess of 10^5 cps.

Step 12: Use the recorder to check the shape of the elastic peak. Often times there will be a tail on the energy loss side of the elastic peak, causing the elastic peak to be asymmetric. This is caused by the target increasing the angular divergence. To reduce this tail do the following:

- Shift the recorder pen using the motorpot to the position of the tail.
- Change E_4 to reduce the tail.
- Go back to the elastic peak.
- If the elastic peak is reduced by more than 25%, change E_4 in the other direction.
- Optimize the elastic peak using E_2, ΔE_2, E_1, ΔE_1, E_3, and ΔE_4.

E. Reducing the Halfwidth of the Elastic Peak

Step 13: Begin to optimize the resolution by turning down the monochromator pass energy. Turn down the pass energy until the ratemeter registers a count rate of a few hundred cps. Make sure that you don't lose the signal because it is very tough to get it back. Regain the signal by adjusting in order the following papameters: c_m, Δ_{pm}, R, E_2, E_1, E_3, I_{fil}, and the associated asymmetries.

Step 14: Turn down the analyzer pass energy until the the analyzer slit potential A is the same as the monochromator slit potential M. Turn the motorpot until the signal regains its maximum. This will result in A no longer being equal to M. Repeat step 14 until A is approximately equal to M for a maximum in the elastic peak.

Step 15: Now maximize the elastic peak by adjusting the gun parameters, the acceleration and deceleration optics, Δ_{pm}, Δ_{ma}, and Δ_{sa}.

You may wish to repeat steps 13 through 15 for an even better resolution. There is always a tradeoff, however, between count rate and resolution. How far down you may go in resolution depends on a number of things. Some loss peaks (such as overtones) demand a gain of x10,000 over the elastic peak. Obviously one needs count rates well in excess of 10,000 cps in order to observe these peaks. One can reduce the resolution only so far and still retain these count rates. Other losses (such as optical phonon losses) are in general a significant fraction of the elastic peak. One can improve the resolution and reduce the elastic

peak to even 1000 cps and still be able to observe these losses. Disordered surfaces have a lower reflectivity, and hence a lower maximum count rate for the elastic peak. One can, in general, achieve a better resolution on well ordered, single crystal surfaces. Finally, some semiconducting samples cause a broadening in the elastic peak due to scattering from free carrier excitations.[1] This can sometimes degrade the ultimate resolution.

F. Tips on Achieving the Maximum Possible Signal

Sometimes, no matter how many times you go through the cycle of optimization, you can't seem to increase the count rate to a reasonable value. This can be very frustrating. What has happened is that you have reached a local maximum in the adjustment of the parameters. Experience has shown that there are several things one can do that may increase the count rate:

- Degrade the resolution slightly by doing steps 13-15, except this time increasing the pass energy. This will always result in a higher count rate. Often one can achieve a significant increase in the signal with only a slight degradation of the resolution.
- Adjust the angle θ. On well ordered, single crystal surfaces the angular halfwidth of the scattered beam is only a few degrees. Even being slightly off-specular could reduce the signal significantly.

- Check the asymmetries. Very large asymmetry voltages in the acceleration and deceleration optics indicate some geometric misalignment. Reduce the asymmetry and remaximize. The interaction of ΔE_2 and the x-position is particularly strong.
- Optimize the signal at the sample by observing the current at the sample using the picoammeter. Then optimize the signal on the ratemeter by adjusting the deceleration optics and the analyzer settings.
- Change the primary energy and reoptimize. Often the reflectivity is very sensitive to the incident electron energy.
- Change the monochromator slit potential M using C_m. Then change the analyzer slit potential A using C_a and reoptimize.

Experience with the will eventually give one the "feel" of the spectrometer. This is very helpful in obtaining the maximum possible signal.

G. Troubleshooting

Sometimes no signal is obtainable even in the straight through position. There are several possible causes for this, and some of them are given here.

- Check the cables, and make sure the power is on to all components.

- Is the high voltage on? If so, check the output with a high voltage probe.
- Transients of unknown origin have been known to blow transistors in the pre-amp. The one that blows most often has been put into a socket for easy removal. Check this one first.
- Measure the resistance of the channeltron by measuring the current flow through the channeltron caused by a small battery. Use the picoammeter to measure the current. This can be done without bringing the system up to air by connecting to the two MHV connectors at the top of the spectrometer. The resistance should be about 10^8 Ω.
- If the problem is not in the HV supply, the pre-amp or the channeltron, it is probably in the spectrometer itself. Remove the spectrometer and check for continuity between the feedthrough pins and the various parts of the spectrometer. Wires have been known to come loose from the feedthrough.